INORGANIC CHEMISTRY FRONTIERS

REVIEW

View Article Online
View Journal | View Issue

Cite this: *Inorg. Chem. Front.*, 2023, **10**, 6440

Investigating the role of oxygen vacancies in metal oxide for enhanced electrochemical reduction of NO_3^- to NH_3: mechanistic insights

Sadeeq Ullah,[a] Shiyong Wang,[a] Muhammad Sohail Ahmad,[d,e] Hafiz M. Adeel Sharif,[a] Qingling Liu,[c] Tetsuya Kida,[d,e] Aamir Shafique,[f] Majeed Ur Rehman,[g] Gang Wang *[a] and Jieshan Qiu*[b]

Ammonia (NH_3) is a crucial chemical commodity used extensively in fertilizer production and as a renewable potential energy carrier. Conventionally, NH_3 synthesis relies on the energy-intensive Haber–Bosch process, which requires elevated temperatures and pressures. However, the demanding conditions of this method have led to research into electrochemical NH_3 synthesis *via* nitrate (NO_3^-) and water, creating a sustainable environment. The electrochemical nitrate reduction reaction (NO_3RR) emerged as a promising eco-friendly alternative, boasting reduced energy consumption and mild reaction conditions. Moreover, the NO_3RR is capable of achieving a high NH_3 yield and faradaic efficiency (FE) but poses challenges due to the competing hydrogen evolution reaction (HER), *etc*. To address these issues, it is essential to tailor the structure of the electrocatalysts, such as incorporating oxygen vacancies (OVs) and controlling the coordination environment and local electronegativity. This review offers a thorough description of current developments in the identification, processing, and use of OVs for the NO_3RR. We highlight different OV generation processes and the associated assessment methodologies. Lastly, we discuss the challenges and opportunities of designing metal oxide catalysts with OVs for NO_3RR, aiming to accelerate the development of exceptional electrocatalysts and contribute to a sustainable future for ammonia generation.

Received 4th August 2023,
Accepted 9th September 2023

DOI: 10.1039/d3qi01536j

rsc.li/frontiers-inorganic

1. Introduction

Ammonia (NH_3) is one of the most widely produced synthetic chemicals globally, primarily used in fertilizer manufacturing and the production of fibers, plastics, explosives, and other fine chemicals.[1,2] Recently, it has gained significant interest as a portable energy carrier due to its high energy density and zero carbon emissions, making it a valuable resource.[3,4] The primary method for industrial NH_3 production is the Haber–Bosch process, which involves harsh operating conditions, including temperatures of 400–600 °C and pressures ranging from 150–350 atm. These conditions result in substantial energy consumption, accounting for approximately 1–2% of global energy usage and significant carbon emissions.[5,6] Consequently, scientists are actively seeking alternative and efficient methods for NH_3 synthesis to replace the conventional approach. Among the various options available, the NO_3RR route presents an optimal solution regarding economic feasibility and environmental sustainability.[7,8] Recently, considerable research efforts have been dedicated to investigating diverse innovative methods for electrochemically reducing N_2 to produce NH_3.[9–13] However, the process continues to face challenges in terms of low yield rates and faradaic efficiency (FE),[3,14–16] falling short of the industrial standard for NH_3 production.[17,18] These obstacles arise due to the exceptionally high decomposition energy of the triple bond in N_2 (941 kJ mol^{-1}) and the limited solubility of N_2 in water.[19–22] Furthermore, the dissociation of the first bond in N≡N necessitates an energy input of 410 kJ mol^{-1}, rendering the activation of N_2 exceptionally challenging and energetically demanding. Similarly, the electrochemical conversion of N_2 to NH_3 faces substantial impediments due to the intense competition posed by the side product, namely the hydrogen evolution reaction (HER), observed across traditional catalysts, such as Rh, Fe, and Ru.[23,24] This is attributed to the fact that its theoretical reaction potential

[a]*School of Environment and Civil Engineering, Research Center for Eco-Environment Engineering, Dongguan University of Technology, Dongguan 523106, Guangdong, PR China. E-mail: wghy1979@163.com*
[b]*Beijing University of Chemical Technology, Beisanhuan East Road No: 15, Chaoyang District, Beijing, PR China. E-mail: qiujs@mail.buct.edu.cn*
[c]*Tianjin Key Lab of Indoor Air Environmental Quality Control, School of Environmental Science and Technology, Tianjin University, Tianjin, 300350, China*
[d]*Institute of Industrial Nanomaterials (IINa), Kumamoto University, 2-39-1 Kurokomi Chuo ku, Kumamoto, 860-8555, Japan*
[e]*International Research Organization for Advanced Science and Technology (IROAST), Kumamoto University, Kumamoto, 860-8555, Japan*
[f]*Department of Physics, University of Ulsan, Ulsan, 44610, South Korea*
[g]*Department of Physics, University of Science and Technology of China, Hefei, Anhui 230026, China*

(0.09 V *vs.* RHE) closely resembles that of the hydrogen evolution reaction (HER).

While nitric oxide (NO) is a more reactive nitrogen source compared with N_2, its limited solubility in aqueous electrolytes poses a significant obstacle for NO electroreduction. This requirement for concentrated NO hampers its progress and impedes further development. Many noble metals exhibit promising NORR activity, with NH_3 being the main reduction product with numerous catalysts.[8,25,26] However, their scarcity imposes severe limitations on their widespread utilization. Consequently, the pursuit of cost-effective materials for electrochemical NORR catalysis remains a formidable challenge. Though Cu foam demonstrated an impressive NH_3 faradaic efficiency (FE) of 93.5% when utilizing NO from exhaust emissions, it is important to note that the direct use of concentrated NO gas, as described in the study, could present a significant hurdle to its commercial viability. This is due to the necessity for an additional facility for the concentration of NO gas extracted from exhaust emissions. In a similar way, Kim *et al.*[27] accomplished the precise electroreduction of NO to NH_3 with nearly 100% NH_3 FE using a nanostructured silver electrode and an electrolyte devised by EFeMC (EDTA-Fe^{2+} metal complex), with the initial NO concentration set at 1%. Nonetheless, when assessing the economic viability of this setup, the researchers determined that the cost of producing NH_3 through the NORR in the EFeMC-designed electrolyte was roughly 2.5 times greater than the prevailing commercial NH_3 price. In practice, NO concentrations in real-world exhaust gases tend to be relatively low, whereas previous research on electrochemical NORR has predominantly centered around high-concentration NO. Therefore, future investigations should delve into advanced NORR electrocatalysts capable of performing effectively with low-concentration NO or even real exhaust gases. To sum it up, the limited availability of effective and selective catalysts, the complexities related to NO solubility in aqueous solutions, and the necessity for an additional step to concentrate NO collectively impede further advancements in the electrochemical production of NH_3 from NO.

In contrast, the electrochemical reduction of nitrate offers a promising alternative as it does not require the breaking of high-energy bonds (204 kJ mol^{-1}), allowing for faster reaction rates and enhanced NH_3 production; see Table 2.[18,28] Moreover, the substantial difference in the standard reduction potential between nitrate (NO_3^-; 0.69 V *vs.* RHE) reduction and the HER implies that NO_3^- reduction effectively avoids the hindrance caused by competing for the HER (Fig. 1a).[29] Furthermore, NO_3^- serves as an abundant nitrogen source, particularly in industrial wastewater and contaminated groundwater, contributing to the worldwide nitrogen cycle imbalance.[30] Consequently, a viable approach to "turn waste into wealth" and establish a closed N-cycle (Fig. 1b, pathway 1) involves utilizing renewable energy sources to drive electrochemical NO_3^--to-NH_3 conversion, thereby mitigating the adverse effects of nitrates on public health.[31,32]

Recently, there has been an interest in the electrocatalytic NO_3RR to yield valuable NH_3.[34–36] This methodology utilizes water as the primary source and can be sustained by renewable energy sources such as wind and solar energy. Yet, its efficacy is undermined by the occurrence of side reactions, including the HER.[37] Therefore, there is an urgent need for high-performance electrocatalysts with outstanding selectivity and stability. The electrode materials significantly influence the reaction kinetics and product selectivity in the electrochemical NO_3RR.

The typical half-cell reaction for the NO_3RR is as follows:

$$NO_3^- + 6H_2O + 8e^- \rightarrow NH_3 + 9OH^-$$

Sadeeq Ullah

Dr Sadeeq Ullah received a B.S. degree in Chemistry from the University of Malakand Pakistan in 2014, and an M.S. and a Ph.D. in Materials Science from Beijing University of Chemical Technology, China, in 2018 and 2021. Then, he experienced experimental approaches in the field of electro-catalysis and energy storage technology concerned with electrochemical methods at Dongguan University of Technology as a postdoctoral position. Currently, he is working at Dongguan University of Technology, China, in Environmental Research and his main research interest is electro-catalyst design for nitrate reduction to ammonia (turning waste to wealth) to create a global sustainable environment.

Shiyong Wang

Dr Shiyong Wang received his Ph.D. degree from the School of Chemical Engineering at Dalian University of Technology (DUT) in 2019. He is currently an associate research fellow at the School of Environment and Civil Engineering, Dongguan University of Technology, China. His main research interests are the treatment of high-salt wastewater and heavy metal wastewater, ion separation, and purification.

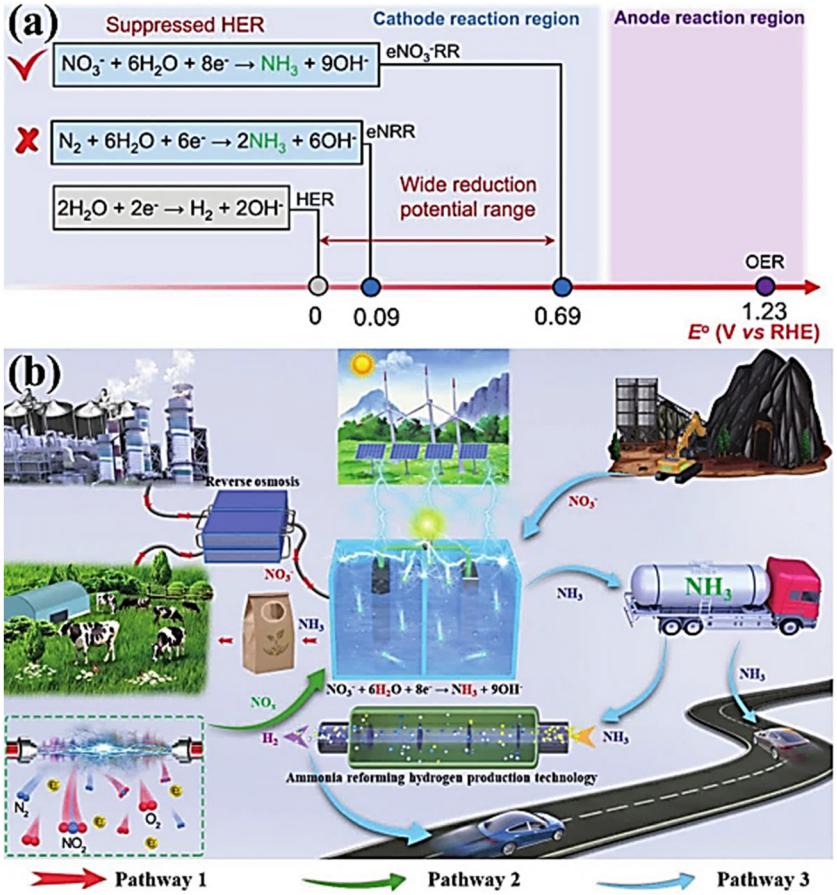

Fig. 1 (a) The standard reduction potentials for the HER, NRR, and NO_3RR were compared. Reproduced from ref. 29 with permission from the American Chemical Society, copyright 2022. (b) The design schematic illustration of the NO_3RR process to NH_3. Reproduced from ref. 33 with permission from Wiley, copyright 2023.

In this context, the main goal of catalysts is to guide the reduction process toward the production of ammonia while simultaneously minimizing the formation of side products stemming from different NO_3RR pathways and the HER. This ultimately leads to the achievement of high FEs for NH_3 synthesis. Recently, scientists have dedicated considerable effort

Hafiz M. Adeel Sharif

Dr H. M. Adeel Sharif received a Ph.D. degree from the Chinese Academy of Science (CAS), in 2019 under the supervision of Prof. Wang Ai-Jie (distinguished Prof.). During his Ph.D. he received an excellent student award for the synthesis of core–shell recyclable materials used for the treatment of industrial pollutants (air pollution and wastewater). Recently, he has been working at Dongguan University of Technology as a post-doc researcher. His research focuses on developing dynamic nano-composites and emerging technologies for green environments.

Gang Wang

Prof. Gang Wang received his Ph.D. degree from the School of Environmental Science and Technology at Dalian University of Technology (DUT) in 2009. He is currently a professor at the School of Environment and Civil Engineering, Dongguan University of Technology, China. He is mainly engaged in capacitive deionization for desalination, ion separation and purification, high-performance adsorbents for uranium extraction, and electrochemically advanced oxidation technologies.

towards devising and fabricating electrocatalysts for use in the electrochemical NO_3RR to enable efficient NH_3 synthesis, making it a recent area of intense interest in the field of electrocatalysis.[38–40] The effectiveness of the electrocatalysts commonly used is impeded by the complex eight-electron reduction process and the synchronized occurrence of the HER, which poses a competitive challenge.[20] This limits their selectivity and efficiency in producing ammonium from NO_3^- electroreduction. As a result, there is a pressing need to devise a new approach for creating highly efficient electrocatalysts that can selectively produce ammonium during NO_3^- electroreduction. Considerable endeavors have been directed toward creating advanced metal electrode materials by incorporating heteroatoms/heterojunctions,[41–43] and introducing noble metals.[7,44,45] Recent investigations have demonstrated that the inclusion of vacancy sites, such as selenium-vacancy, S-vacancy, and oxygen vacancy (OV), within materials based on metal oxides presents a straightforward and efficient approach for boosting their catalytic effectiveness.[46–51] The incorporation of OVs as a strategy has found extensive application in diverse fields, including the OER,[52,53] ORR,[54,55] CO_2RR,[56,57] HER[58,59] and NRR,[60,61] supercapacitors,[62] and batteries,[63,64] with impressive results showcasing their remarkable ability to adsorb and activate various molecules like O_2, H_2O, and H_2, among others. Similarly, in the case of electrochemical nitrogen fixation, OVs can function as active sites by delivering electrons into the anti-bonding orbitals of nitrogen molecules, facilitating their adsorption and activation. Studies have documented this phenomenon, highlighting the roles of OVs in the regulation of the electronic makeup and their impact on the adsorption of electrochemical reaction intermediates.[65–67] When combined with metal cations, neighboring OVs can act as unsaturated active sites, enabling the adsorption and weakening of N–O bonds, thereby boosting NO_3^- reduction.[68] Hence, a comprehensive exploration of the impact of OVs on the electrocatalytic NO_3RR and its intermediates is imperative to guide the design of catalysts with superior catalytic performance.

Our review covers the literature on the use of metal oxides as electrocatalysts, specifically focusing on the OVs for the NO_3RR to NH_3 up to June 2023. The purpose of this review is to show the advantages and possibilities that OVs offer to catalysis due to their enhanced morphology and the possibility of active sites on the surface of metal oxides.

Previous review articles that consolidate the utilization of oxygen vacancies (OVs) in metal oxides often exhibit a more limited focus. These reviews primarily delve into particular metal categories or applications distinct from those discussed in this comprehensive review article. For example, Jiang *et al.* investigated the influence of OVs in enhancing the photocatalytic CO_2 reduction reaction.[69] In a recent review article, Wang and co-authors conducted an extensive examination of the formation and characterization of OVs in metal oxides. Nevertheless, this paper lacks in-depth coverage of the practical applications of OVs in catalytic processes.[70] On a similar note, Lin *et al.* directed their attention toward the analysis of oxygen vacancies within rare earth CeO_2, a catalytic material extensively applied across diverse fields.[71] Additional research from various teams encompasses a wide range of organic transformations, exemplified by processes like CO oxidation and water–gas shift reactions. These instances are used to showcase the pivotal role of the metal oxide interface in catalytic activity.[72] Wang *et al.* provide a comprehensive review, critically examining the role of oxygen vacancies (OVs) in metal oxide photoelectrodes for photoelectrochemical water splitting.[73] Furthermore, Singh *et al.*[74] studied the approaches to control the concentration of OVs during the growth of metal oxides and the mechanism by which these vacancies affect catalytic reactions. They also explore the regeneration of OVs in aged catalysts and their role in the regeneration of electrocatalytic activity for CO_2 reduction. However, the precise role played by oxygen vacancies (OVs) in a diverse array of nanocatalysts during the electrochemical conversion of nitrate to ammonia lacks prior documentation. This review paper brings together recent progress in the realm of catalysts enriched with oxygen vacancies, offering an in-depth exploration of their specific contributions to the electrochemical reduction of nitrate to NH_3. Furthermore, we placed particular emphasis on the various techniques utilized to create oxygen vacancies (OVs), advanced methods for characterizing these vacant sites, and delved into the comprehensive role that OVs play in the electrochemical nitrate reduction reactions.[67]

Taking into consideration the significant role of OVs in electrochemical reduction reactions, we have consolidated the most recent research on catalysis involving OVs in this comprehensive review. Our focus in this paper specifically centers on defect metal electrocatalysts for the electrochemical reduction of NO_3^- to NH_3. Furthermore, we have provided a concise overview of the catalytic mechanism underlying the heightened activity of OVs in NO_3^- reduction reactions. Additionally, we have outlined prospective advancements, challenges, and potential developments associated with the utilization of OVs in electrochemical NO_3^- reduction. To the best of our knowledge, a comprehensive review dedicated to the electrochemical conversion of NO_3RR to NH_3 is lacking in the literature. In this review, we will summarize recent advances in the case of catalysts composed of oxygenated architectures; the injection of ample OVs has been discovered to enhance the catalytic activity of NO_3RR by controlling the coordination environment and local electronegativity. This review offers a thorough description of current developments in the identification, processing, mechanisms, and use of OVs for NO_3RR in Scheme 1. We highlight different OV generation processes, such as wet chemical procedures, high-temperature hydrogen reduction, vacuum annealing, plasma treatment, and ion doping techniques, as well as the associated assessment methodologies. Finally, we insight opportunities and challenges associated with designing OVs in oxide-based catalysts for the NO_3RR, aiming for the rapid progress of the efficient electrocatalysts and a prosperous future of a sustainable vector of ammonia generation.

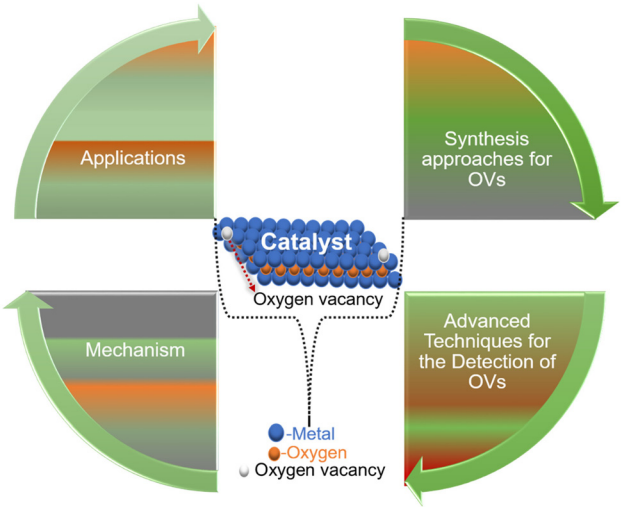

Scheme 1 The general overview covering the outlines of this review.

2. The electronic structure fingerprint of oxides: unseen actors (oxygen vacancies in metal oxides)

OVs have long remained imperceptible agents that exist on oxide surfaces. While their presence and characteristics were acknowledged, their visibility and reactivity could not be directly observed. However, a groundbreaking milestone was achieved by Flemming Besenbacher and colleagues,[75] who investigated the surface migration of OVs on TiO_2 using scanning tunneling microscope (STM) images (Fig. 2a–c). This breakthrough marked the first instance where the migration of OVs was examined in such detail. Through successful tracking of this dynamic phenomenon, the researchers unveiled that short-lived O_2 molecules facilitate the movement of OVs. These adsorbed O_2 molecules diffuse throughout the surface, actively seeking vacancies. Upon locating a vacancy, they undergo dissociation to occupy the vacancy, generating an O atom that subsequently adheres to the nearest Ti atom. Defect engineering, which involves introducing surface defects into solids, specifically metal oxides, has gained widespread application in modifying electrode materials' electronic structure and surface properties. A wide array of defects and irregularities have been extensively reported in the existing literature to date.[76] Among these, OVs are the most common and can serve as a distinctive characteristic of the electronic configuration of metal oxides.[46,77,78] We shall examine magnesium oxide (MgO) as an example to elaborate on the electronic arrangement upon OV induction. In MgO, the absence of an O atom within the bulk or on the surface leads to the confinement of two electrons within the central void (as depicted in Fig. 2d).[79] The Madelung potential of this profoundly ionic crystal serves as the driving factor behind localizing the electrons within the void. Consequently, in the defective crystal, the position typically occupied by the O_2^- anion in the regular lattice is substituted by two "free" electrons. The presence of trapped electrons at an OV in MgO leads to distinct excitations within the visible range of the electromagnetic spectrum. As a result, the color of the defective material undergoes a noticeable alteration, as depicted in Fig. 2e and f. These centers are commonly referred to as F centers, deriving their name from "Farbe", the German term for color, due to their significant role in coloration phenomena. OVs are characterized by a small hollow area within the oxide matrix, which arises when an oxygen atom is extracted from its atomic-scale structure. The metal–oxygen interaction in their native lattice site causes the liberated oxygen atom to remain in a neutral state instead of being ionized. Consequently, the vacancy site retains two electrons, leading to an excess electron density on neighboring metal cations, thereby reducing their valence states (Fig. 2g and h).[77,80] Recent research has shown that OVs in metal oxides hold great potential as a platform for the selective capture and conversion of ions in electrochemical systems. The key attributes of this approach include quicker electron transfer and stronger contact with the oxygen atom from the target species.[81,82]

By considering factors such as the Gibbs free energy (ΔG_f), mass and balance charge, and lattice site availability, the formation of OVs can be anticipated using the following reactions.[70]

$$O_o^x \Leftrightarrow 0.5O_2 + 2e' + OV \quad (1)$$

$$O_o^x \Leftrightarrow 0.5O_2 + e' + OV \quad (2)$$

$$O_o^x \Leftrightarrow 0.5O_2 + OV \quad (3)$$

The expressions used in the Kröger–Vink notation, where O_o^x represents a neutral divalent oxygen ion, e^- for an electron, and OV denotes an oxygen vacancy (with single OV and double OV denoting the charge state of $^+1$ and $^+2$, respectively), are utilized to predict the formation of OVs.[86] The conditions that govern the interaction between the lattice of the metal oxide and the presence of atmospheric oxygen during the different reaction conditions have a significant influence on the equilibrium of various defect types. The relationship between the concentration of OVs and the partial pressure of oxygen could be determined by investigating the ΔG_f and equilibrium constant (K) of the defect reaction, as shown in eqn (4).[37,86]

$$K = \frac{[V_{\ddot{O}}] \times p(O_2)^{0.5}}{[O_o]} = \exp\left(\frac{-\Delta G_f}{K_B T}\right) \quad (4)$$

Eqn (4) demonstrates that when OVs are created, lattice oxygen atoms are discharged from the oxide matrix in the form of O_2 molecules (gas). As per the aforementioned equation, the formation of a defect site becomes more favorable under low-oxygen partial pressures. This principle has been extensively used in the development of OVs using diverse techniques.

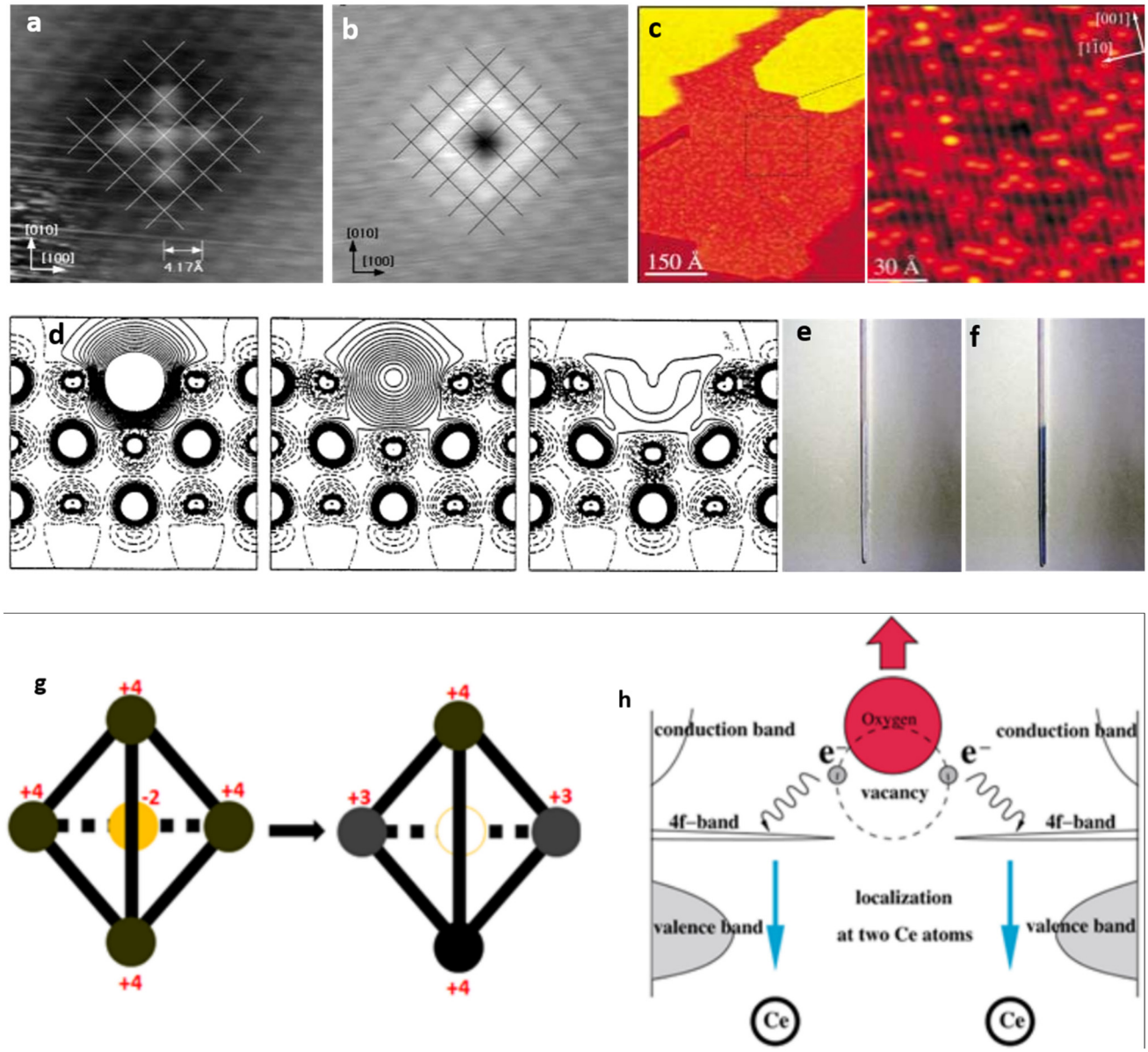

Fig. 2 (a and b) Scanning tunneling microscopy (STM) images indicating the empty state (a) and filled states (b) on a NiO(100) surface, disclosing the availability of vacancies. Reproduced from ref. 83 with permission from the American Physical Society, copyright 2022. (c) STM observation illustrating OVs as bright spots on the surface of TiO_2. Reproduced from ref. 77 and 75 with permission from Wiley, copyright 2003. (d) Electron density difference plot showing different OV configurations at the surface of MgO: left, a neutral OV with 2 trapped electrons forming an F center; a charge vacancy with 1 trapped electron forming an F^+ center; and a doubly charged oxygen without trapped electrons forming an F^{2+} center. Reproduced from ref. 79 with permission from the American Association for the Advancement of Science, copyright 2002. (e and f) Two samples of polycrystalline MgO powder showing low (e) and high (f) concentrations of trapped electrons, resulting in significant color changes. Reproduced from ref. 77 with permission from Wiley, copyright 2003. (g) The structure of CeO_2 consists of an oxygen atom at the center surrounded by four Ce atoms forming a tetrahedron. The process of reduction shown by the arrow leads to a neutral O vacancy at the center of the tetrahedron (empty circle) while two of the Ce ions have been reduced to the +3 oxidation state. Reproduced from ref. 85 with permission from IOP, copyright 2010. (h) The formation of an OV in Ce involves the release of an oxygen atom from its lattice position, leading to the localization of two electrons on the two Ce atoms and the reduction of Ce ion oxidation states from 4^+ to 3^+. Reproduced from ref. 40 with permission from IOP, copyright 2002.

3. Advanced characterization techniques for the detection of OVs

Directly imaging the atomic-level lattice cave poses a significant challenge because an OV serves as a virtual object representing the oxygen lattice site in a crystal. However, there are alternative methods to indirectly characterize OVs by examining the changes they bring in the structure or electronic state, as the production of OVs can alter the electronic configuration and coordination of the surrounding metals, which can serve as a unique identifier for the OVs in metal oxides.[77,87] For

instance, the STM (scanning tunneling microscope) can be used to visualize the OV caves,[88,89] while PAS (positron annihilation spectroscopy) can be used to monitor them.[90,91] Moreover, the XRD, ND (neutron diffraction), and XAS (X-ray absorption spectroscopy) techniques can detect changes in the crystalline structure caused by OVs.[92,93] XPS (X-ray photoelectron spectroscopy), EPR (electron paramagnetic resonance) spectroscopy, PL (photoluminescence) spectroscopy, and XAS (X-ray absorption spectroscopy) can be used to modify the electronic property.[77] A recent publication has discussed the various pathways available for characterizing OVs, which are illustrated in Fig. 3.[73] In this paper, our attention is directed toward the commonly employed effective strategies: XPS, EPR, and XAS.

3.1 X-ray absorption spectroscopy (XAS) technique

The characterization of OVs encompasses the investigation of changes in the electronic configuration and crystalline structure, requiring a detailed analysis of alterations in the electronic distribution and the arrangement of atoms within the crystal lattice. The chemical changes can be analyzed by using the XPS and EPR techniques, while both feature electronic and structural properties can be analyzed with XAS. The interaction of X-ray photons with core electrons in atoms gives rise to a distinctive peak in the absorption intensity at a particular energy level, which is referred to as the absorption edge. XAS can be categorized into two distinct groups depending on the absorption range; XANES (X-ray absorption near edge structure) covers the absorption region from the edge up to several tens of electrons volts (eV), while extended X-ray absorption fine structure (EXAFS) includes the absorption range from the edge to several hundreds of eV.[94] XANES can provide information about the extent of orbital occupation, specifically the number of electrons occupying a particular orbital. For instance, the study of oxygen deficiency in $CaMnO_3$ (Fig. 4b) has revealed an apparent decrease in the chemical state of Mn through Mn $L_{2,3}$-edge analysis.[95] Additionally, the formation of OV generates energy levels of oxygen defects in the band gap, resulting in changes to the XANES of the O K-edge. This phenomenon is demonstrated in Fig. 4c, which illustrates the change in the O K-edge of HfO_2 where OV induces a reduction in electron occupation and a band tail near the conduction band edge (inset Fig. 4). Zhu and his team[96] conducted an investigation using XANES analysis to explore the structural defects in Vd-V_2O_3. The results revealed that the V component in Vd-V_2O_3 has a higher oxidation state than c-V_2O_3, as indicated by the edge spectra observed at the B-site in Fig. 4f. The presence of vanadium vacancies in Vd-V_2O_3 might contribute to the elevated levels of V^{4+}, increasing the oxidation state of vanadium. As depicted in Fig. 4f (site A), the intensified pre-edge band indicates a reduction in the local symmetry in the Vd-V_2O_3 sample. This observation suggests that the structure of Vd-V_2O_3 experiences distortion around the vanadium atoms due to the lack of neighboring atoms. In contrast to XANES,

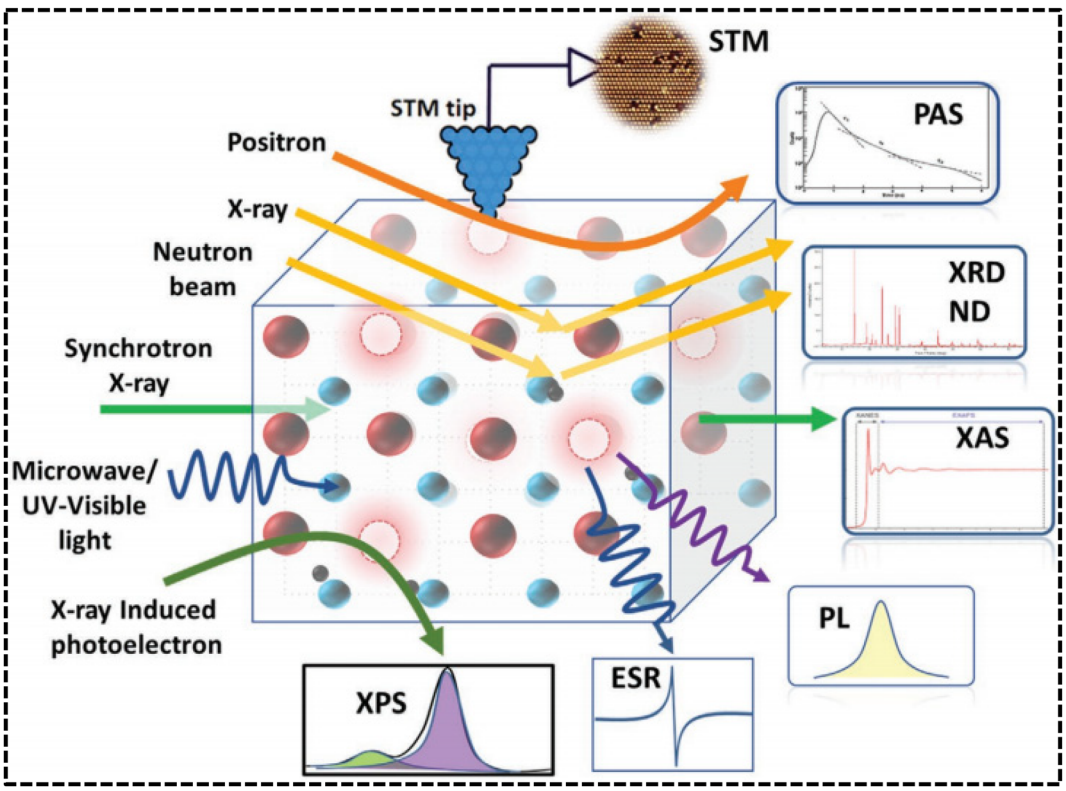

Fig. 3 A characterization technique used for the detection of OV. Reproduced from ref. 73.

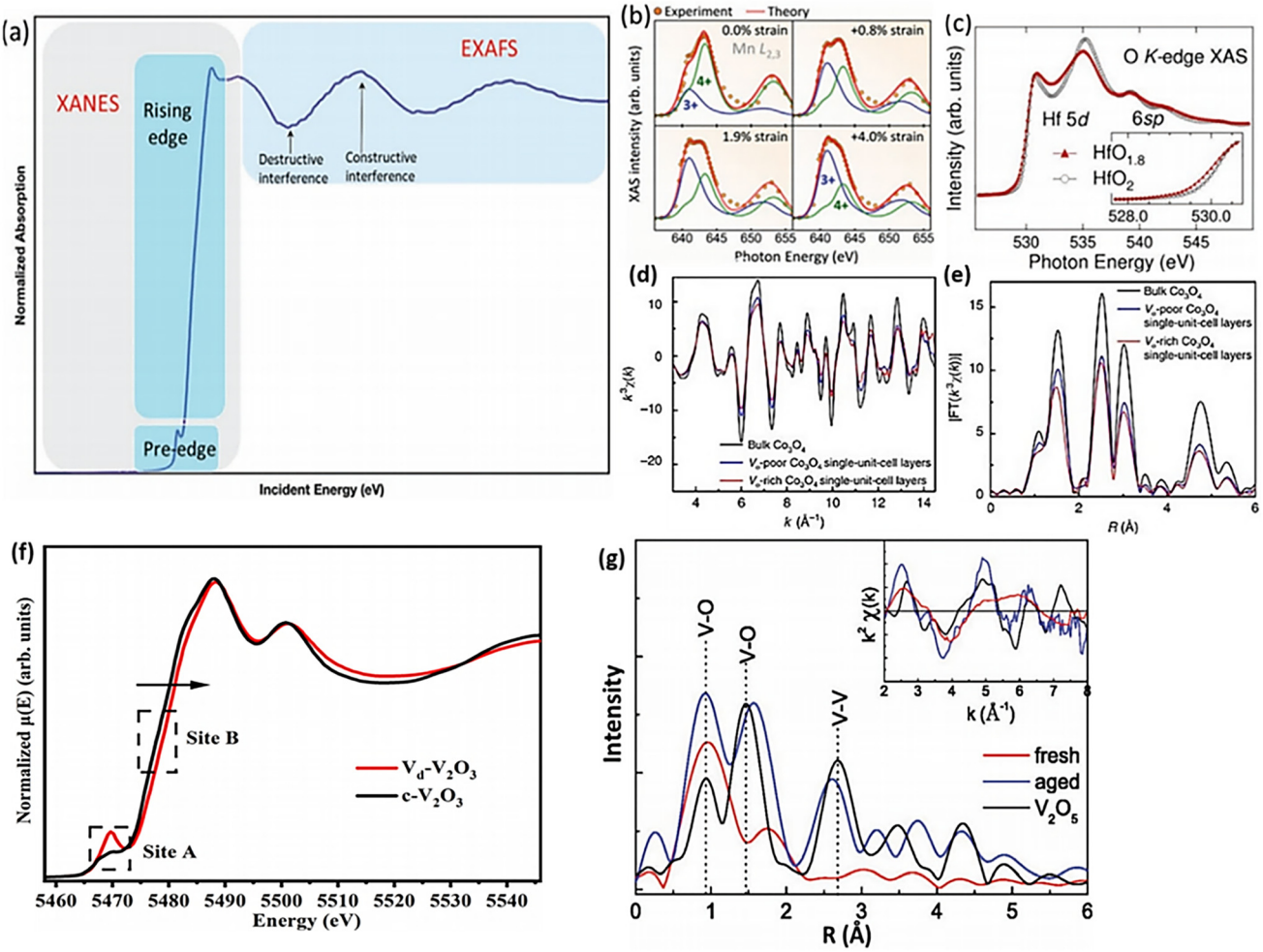

Fig. 4 Presents various XAS analyses used for characterizing OVs in metal oxides: (a) the typical profile of the XAS. Adapted with permission.[94] (b) The XANES of a Mn L-edge under different strains. Reproduced from ref. 95 with permission from the American Chemical Society, copyright 2017. (c) The XANES of an O K-edge of HfO_2 with OVs. Reproduced from ref. 97. (d) and (e) EXAFS oscillation and the corresponding Fourier transforms of VO-rich Co_3O_4 and VO-poor Co_3O_4 single-unit-cell layers. Reproduced with permission.[98] (f) Normalized XANES spectra of a V K-edge for Vd-V_2O_3 and c-V_2O_3. (g) The FFT of k^2-weighted EXAFS of a V L-edge for different V_2O_5 samples. Reproduced from ref. 99 with permission from AIP, copyright 2014.

EXAFS offers a more direct means of understanding changes in the crystalline structure of OV, such as variations in M–O bond length and M coordination number. When OV is produced in metal oxides (MOs), the crystal structure may undergo relaxation, which can alter the nearby M–O bond. Utilizing k^2-weighted EXAFS and subsequent fast-Fourier transforms (FFT), by examining the magnitude and relative distance of interatomic forces, it becomes feasible to calculate the average number of nearest neighbors and the interatomic distances, respectively.[97] As an illustration, Gao *et al.*[98] obtained a Co_3O_4 sample rich in OV by calcining a Co precursor at 320 °C in an air environment. The EXAFS analysis, shown in Fig. 4d and e, unveiled the significant concentration of V_O and indicated a decrease in the coordination number of Co–O bonds in the V_O-rich Co_3O_4 material. Another research study on V_2O_5 film found that the recently manufactured sample had much weaker V–O bonds than the conventional V_2O_5, suggesting that the presence of OVs inhibited V–O bond formation. However, the OV defect was restored with aging, leading to a significant increase in V–O bond strength. (Fig. 4g).[99]

3.2 Electron paramagnetic resonance (EPR) method

In the characterization of OVs, the electron that is compensated in OV can exhibit different behaviors depending on the concentration of OVs and the temperature. Metal ions can entrap it or position it close to the OV, leading to changes in the electron spin state of MOs, and this causes the magnetron to react to an external field.[100] Therefore, using the EPR technique can be an excellent method for detecting the presence of OV with high accuracy and sensitivity.[101,102] Electron spin resonance (ESR) spectroscopy, also known as EPR spectroscopy, was utilized to detect OV signals in several different types of material. For example, in FTO-E (Fe_2TiO_5) prepared by the electrospinning method and FTO-H (Fe_2TiO_5 prepared by

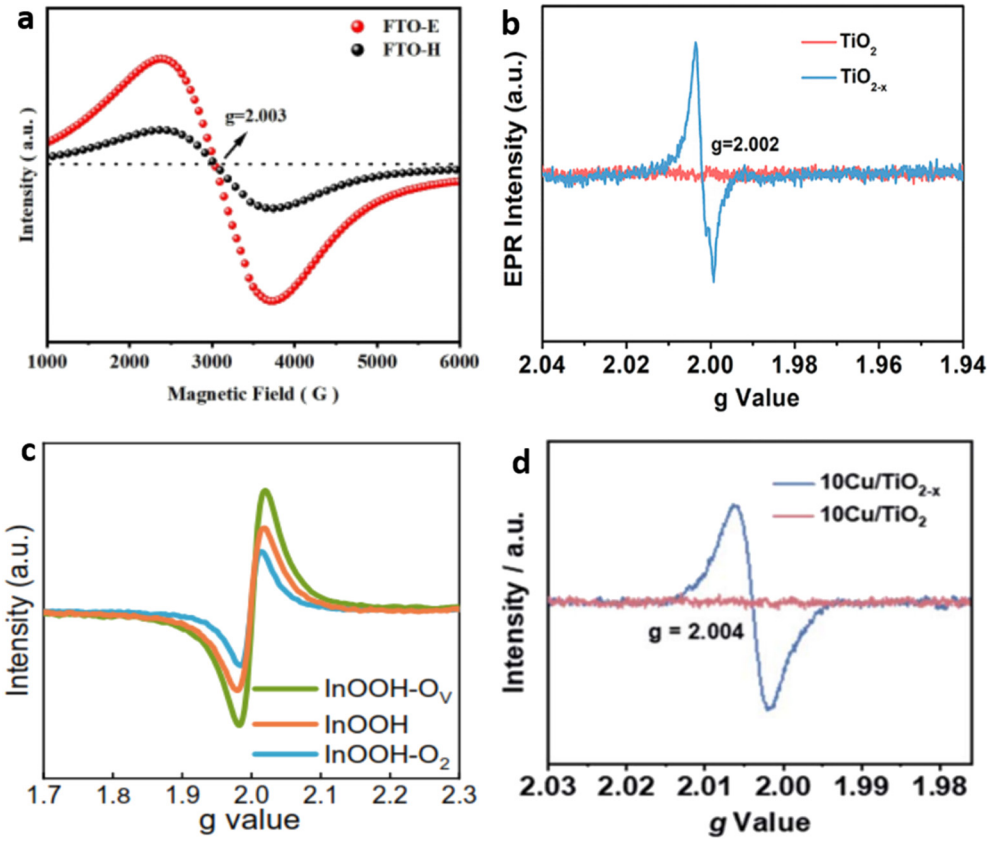

Fig. 5 Displays the EPR spectra of (a) FTO prepared by electrospinning and hydrothermal methods. Reproduced from ref. 103 with permission from Wiley, copyright 2022. (b) Prisitine TiO_2 and TiO_2 nanotubes. Reproduced from ref. 105 with permission from the American Chemical Society, copyright 2020. (c) Indium oxyhydroxide with different vacancies. Reproduced from ref. 22, and (d) Cu cluster deposited TiO_2. Reproduced from ref. 106.

the hydrothermal method), the ESR signal exhibited peak values at g = 2.003, indicating the presence of OVs[103,104] (Fig. 5a). Additionally, the larger magnitude of the ESR signal in FTO-E suggests that higher concentrations of OVs are generated in this sample compared with FTO-H. Similarly, the EPR spectroscopic technique has also been utilized to successfully detect the formation of OVs in various materials such as TiO_2 nanotubes,[105] Cu cluster TiO_2,[106] and indium oxyhydroxide (InOOH-OV) (Fig. 5b–d).[22]

3.3 X-ray photoelectron spectroscopy (XPS) analysis of the detection

XPS proves to be a highly effective and precise method for measuring the presence of defect sites in solid material. XPS measurements can be used to observe the shift in M–O bonding energy caused by the presence of OVs in a material.[107,108] The formation of OVs can result in charge compensation, leading to the reduction of metal ions and the subsequent formation of low-valence metal ions. This phenomenon is illustrated in the XPS spectra of the Mo 3d and O 1s of OV-MoO_3/Ce samples.[109] Upon the inclusion of OVs through Ce doping, the binding energy of Mo in the OV-MoO_3/Ce spectra demonstrates a declining pattern, suggesting the reduction of some Mo^{6+} to Mo^{5+}. The ratio of Mo^{5+} to Mo^{6+} gradually increased with the increasing amount of Ce doping, as illustrated in Fig. 6a, c, e, and g of the Mo 3d XPS pattern. The content of Mo^{5+} is considered a reliable indicator of the relative abundance of OVs; thus, a higher Mo^{5+} content corresponds to a greater amount of OVs. The O 1s spectrum further confirmed this result (Fig. 6b, d, f, and h). The presence of a prominent peak at 531.8 eV in OV-MoO_3/Ce, in contrast to OV-MoO_3, signifies the higher concentration of OVs in the OV-MoO_3/Ce sample.[57] The high-resolution X-ray photoelectron spectra (HRXPS) of In 3d and O 1s of InOOH showed a similar pattern,[22] where the peak for In 3d5/2 at 444.2 eV in InOOH moves down in binding energy after being exposed to Ar plasma and up in binding energy after being exposed to O_2 plasma (as shown in Fig. 6i). This change shows that InOOH-OV has the lowest indium valence of the samples tested.[110,111] The O 1s XPS data exhibited three peaks, at 529.8, 531.5, and 532.8 eV, which corresponded to the oxygen lattice (OL), OVs, and hydroxyl groups from adsorbed water, respectively, as depicted in (Fig. 6j).[112,113] Following Ar plasma treatment, the proportion of OV increases significantly to 40.9% in InOOH-OV, while the OL percentage drops to 19.9%, indicating that lattice oxygen atoms have been removed. In another example, the Co^{2+} and Co^{3+} ratio in Co_3O_4 was also examined before and after plasma treatment.[60] The deconvoluted Co 2p

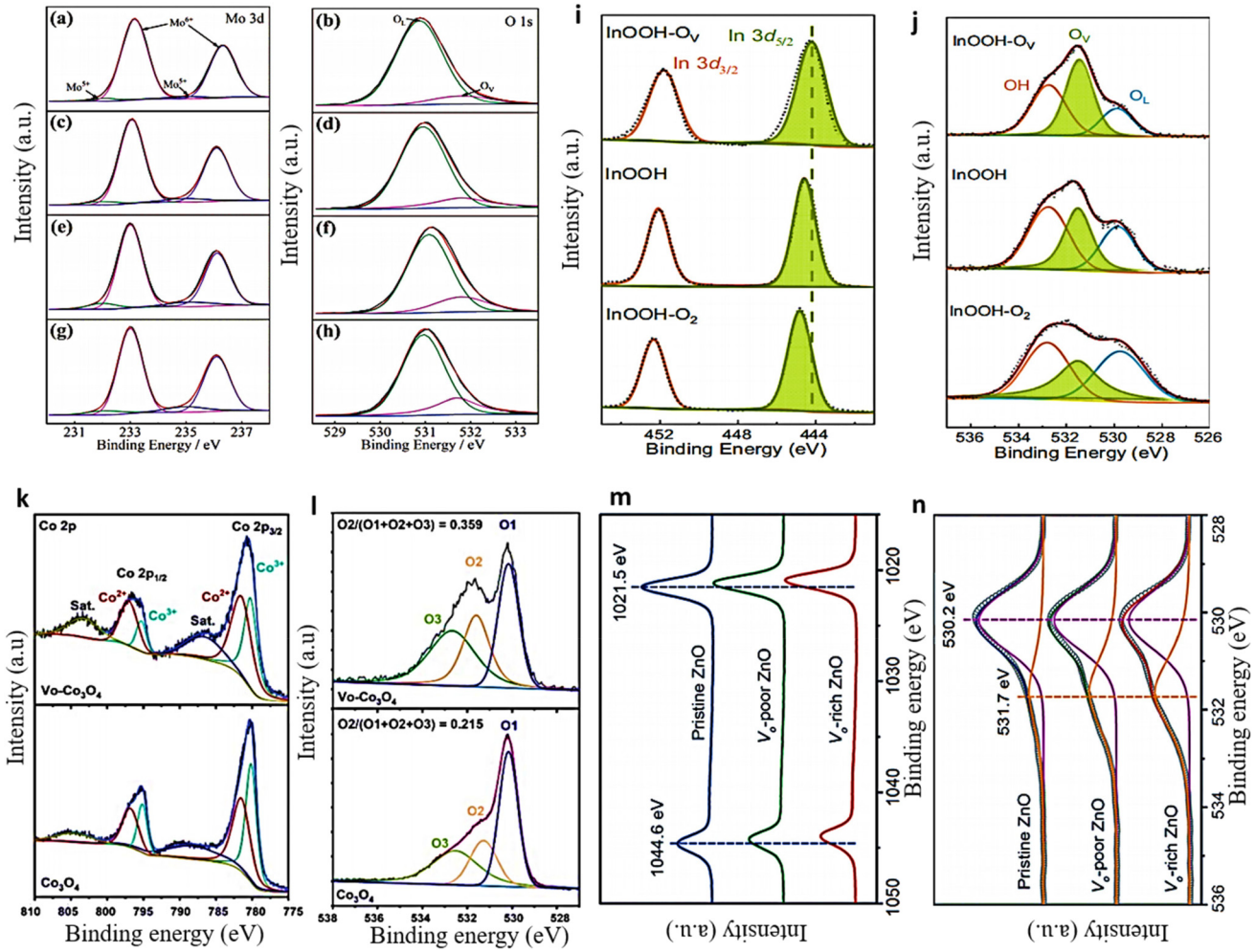

Fig. 6 (a and b) Mo 3d and O 1s deconvolution using XPS in OV-MoO_3. 1 (c and d) XPS analysis of OV-MoO_3/Ce = 40/1 indicates 0.62% doped, (e and f) OV-MoO_3/Ce = 30/1, and (g and h) OV-MoO_3/Ce = 20/1, respectively. Reproduced with permission.[109] (i and j) The corresponding HR-XPS spectra of 3d and O 1 s of InOOH. Reproduced with permission.[22] (k and l) VO-Co_3O_4 and Co_3O_4 Co 2p and O 1s XPS spectra. Reproduced with permission.[60] (m and n) Zn 2p and O 1s XPS spectra of ZnO nanosheets. Reproduced from ref. 111 with permission from Wiley, copyright 2018.

spectra demonstrate an increase in the intensity of Co^{2+} and a decrease in the intensity of Co^{3+} after plasma treatment (as shown in Fig. 6k). The Co^{2+}/Co^{3+} ratios were determined to be 1.48 for VO-Co_3O_4 and 1.10 for Co_3O_4, respectively. The high proportion of Co^{2+} observed in Co_3O_4 following plasma treatment suggests the occurrence of OV generation. The O 1s deconvoluted spectrum revealed the presence of three oxygen species. O_1 at 530.1 eV is associated with the typical M–O bond, while O_2 at around 531.3 eV and O_3 at 532.6 eV are linked to the OVs and adsorbed water, respectively.[114] After plasma treatment, oxygen defects are formed, as evidenced by an increase in oxygen content (from 0.215 to 0.359) and a shift in the O_2 peak to a higher binding energy of 531.6 eV (as shown in Fig. 6l). Likewise, the presence of OVs in ZnO nanosheet samples was detected, revealing that the binding energies of Zn (2p1/2 and 2p3/2) decreased as the concentration of OVs increased in the three ZnO nanosheets[111] (as depicted in Fig. 6m). The material's O 1s spectra exhibited an OV peak at 531.7 eV,[115] which was particularly prominent in the sample with a high concentration of OVs (Fig. 6n).

3.4 Positron annihilation spectroscopy (PAS)

In the realm of porous materials research, there has been a significant surge of interest in PAS in recent times.[91,116] Fig. 7a illustrates a direct approach for detecting cavities in metal–organic framework materials.[117] By interacting with the material matrix, positrons can recombine with electrons. The varying pore sizes within the material will induce distinct positron decay practices, consequently resulting in diverse time-resolved decay patterns, as depicted in Fig. 7b. Given that those vacancies (OVs) are also considered types of cavity within crystals, there is an interest in utilizing PAS to detect these OVs.[118,119] Recent work has used PAS to examine VO in TiO_2 samples synthesized at 350 °C and 550 °C (denoted m-350 and m-550, respectively).[119] Fig. 7c demonstrates two types of positron lifetime, $\tau 1$ and $\tau 2$, which correspond to different defects

found in the samples. The smaller lifetime (τ1) is associated with OV defects, while the larger lifetime (τ2) broadly indicates the existence of micro-pore defects.[120] Approximately 96% and 74% of τ1 may be found in the m-350 and m-550 samples, respectively. These results point to OV flaws as the predominant source of failure in m-350 and m-550. Another study also observed a comparable pattern in the PAS analysis of $Bi_{24}O_{31}Br_{10}$ samples (BOB),[91] and the findings are illustrated in Fig. 7d. It is important to acknowledge that the interpretation of PAS can vary, as stated by the authors of this study, who mention that both pore sizes and grain boundaries can influence the positron decay process. Furthermore, various types of defect, such as metal vacancies, can yield similar results in PAS, as illustrated in Fig. 7e.[121] In a specific investigation of the $BiVO_4$ system utilizing PAS, as depicted in Fig. 7f, the characteristics of vanadium vacancies, as opposed to VO vacancies, have been identified.[122] PAS allows for the quantification of the charge distribution associated with these vanadium vacancies.

4. Commonly used methodologies for the creation of OVs

The abundance of active sites primarily influences the electrochemical properties of electrode materials. Although many materials possess a significant surface area, certain regions within them remain electrochemically inert, impeding the transfer of small molecules or ions. These regions are commonly referred to as inert sites. By employing strategic defect engineering, it is possible to manipulate the chemical environments of these inert sites, rendering them accessible for rapid reaction kinetics.[76] Multiple techniques have been employed to induce the formation of oxygen vacancies in metal oxides,

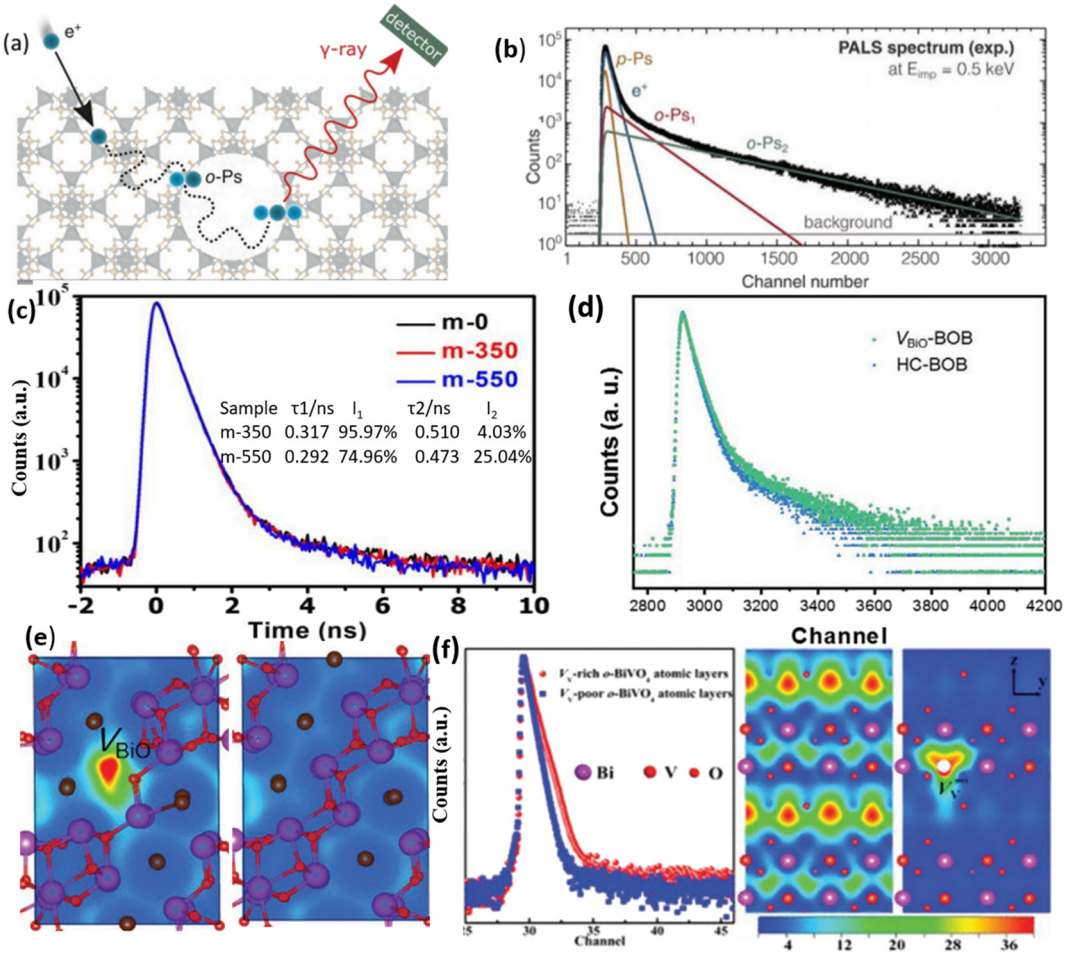

Fig. 7 (a) Positron annihilation model depicted schematically within a porous cave. (b) Analysis of the PAS spectrum and fitting of various degradation processes. Reproduced from ref. 117 with permission from Wiley, copyright 2021. (c) These are the positron annihilation spectra of samples of m-0, m-350, and m-550. The findings of the positron annihilation tests are displayed in the inset of figure (c); τ1 and τ2 are positron lifetimes; I1 and I2 are the concentrations of τ1 and τ2. Reproduced with permission.[119] (d) Positron annihilation lifetime spectrum of VBiO-BOB and HC-BOB, respectively. (e) Schematic representations of trapped positrons of VBiO-BOB and HC-BOB, respectively. Reproduced from ref. 91 with permission from Wiley, copyright 2021. (f) The use of PAS to characterize vanadium vacancies and the heat map that corresponds to the charge distribution around vanadium vacancies. Reproduced with permission.[122]

either during the synthesis process or through post-synthesis treatments. In the following section, we present a comprehensive review of several noteworthy techniques employed for the formation of oxygen vacancies in different materials.

4.1 Thermal annealing

Thermal annealing performed in a vacuum or inert condition can create OVs in metal oxides.[123,124] It is worth mentioning that the careful choice of appropriate reducing atmospheres, treatment durations, calcination temperatures, and types of working gas can control the concentration of OVs in the resulting as-calcinated metal oxide materials.[125,126] In their study, Li *et al.*[127] prepared Bi_2O_{3-x} by oxidizing Bi powder in the presence of air at a temperature of 453.15 K for 8 hours (Fig. 8a). The resulting sample demonstrated a conspicuous EPR signal at g = 2.001, providing evidence of the presence of OVs.[112,128] Conversely, the Bi powder did not exhibit any EPR signal. The EPR data strongly support the hypothesis that the calcined sample contains oxygen defects, which aligns with the absorption spectra depicted in Fig. 8b. The O 1s XPS spectra provided additional support for the EPR data, as evidenced by the presence of the OV peak at 531.2 eV.[129] Notably, the peak area at 531.2 eV was significantly larger in the calcinated sample compared with the Bi powder, indicating that the oxygen vacancies were predominantly obtained through the process of heat treatment (Fig. 8c). Considering all of the aforementioned findings, after the calcination procedure, it is possible to conclude that the sample did produce unique oxygen vacancies.

Similarly, OV-C/TiO_2 samples were synthesized by Qian *et al.*[130] by subjecting Ti_3C_2 MXene, serving as the precursor, to a single calcination step (Fig. 8d). The scientists observed that the temperature employed during the experiment influenced the number of OVs, as indicated by the findings from the XPS and EPR analyses (Fig. 8e and f). The O 1s spectra exhibited a prominent OV peak at 531.9 eV, further substantiated by an EPR signal at g = 2.003.[131,132] As the calcination temperature was increased, a noticeable decrease in the peak intensity was observed, suggesting that the temperature influ-

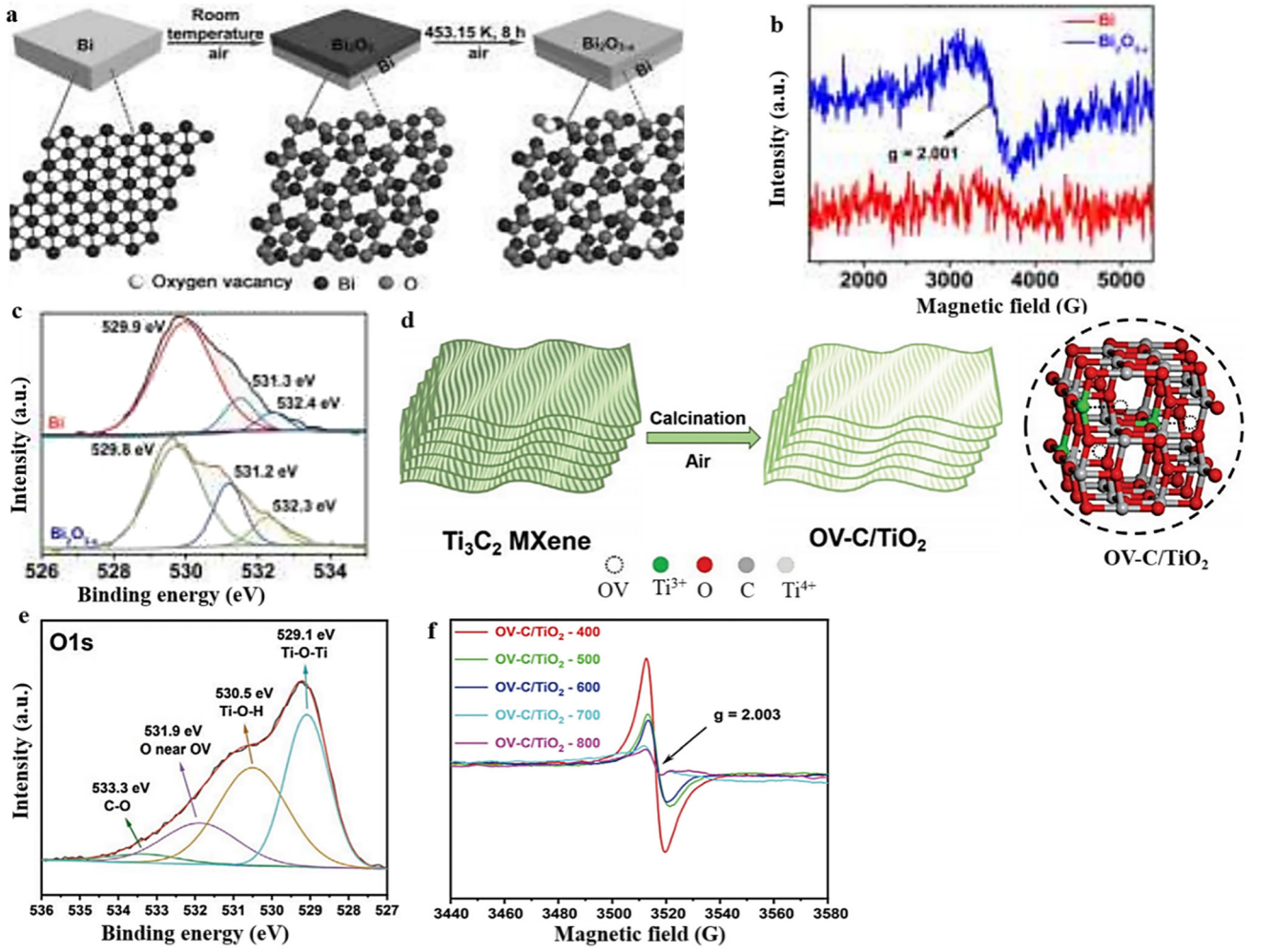

Fig. 8 (a) An illustration of the schematic process for the production of a layer of Bi_2O_{3-x} with oxygen vacancies. (b) and (c) EPR and O 1s XPS spectra of Bi_2O_{3-x}. Reproduced from ref. 127 with permission from Wiley, copyright 2020. (d) Diagram of the preparation process of OV-C/TiO_2. (e) and (f) The O 1s XPS and EPR spectra of OV-C/TiO_2. Reproduced from ref. 130 with permission from Wiley, copyright 2021.

ences the concentration of oxygen vacancies during the calcination process. Other studies have also documented the influence of heat treatment on the generation of OVs.[133,134]

4.2 Plasma treatment

The effectiveness of plasma treatment in producing surface OVs on metal oxides has been well established. During plasma treatment, OVs are formed through the impact of energetic species (*e.g.*, Ar^+, H_2O^+, N^{2+}) on the MO, causing the surface structure to become disordered and facilitating the controlled removal of oxygen atoms from the surface to create vacancies.[135,136] This approach, characterized by its simplicity, high efficiency, and short experimental time, has found extensive application in generating OVs across various materials for various purposes.[53,137,138] To demonstrate this phenomenon, OVs were induced on Co_3O_4 through a 2-minute treatment using Ar plasma (250 W) (Fig. 9a),[114] while H-doped black titania (TiO_2@$TiO_{2-x}H_x$) enriched with OVs was achieved by subjecting it to H_2 plasma.[139] XPS analysis and EPR investigation provided confirmation of the presence of OVs in the samples subjected to plasma treatment (Fig. 9e and f).

4.3 Wet-chemical reduction

The wet chemical redox method offers a scalable solution for introducing OVs into MOs under ambient conditions. This technique relies on the utilization of appropriate reducing agents and operates at low temperatures, ensuring the methodology's safety and cost-effectiveness. As an example, Liu *et al.*[140] demonstrated a simple and efficient chemical approach for the synthesis of oxygen-defective r-Bi_2O_3 (Fig. 10a). The method involved room temperature reduction using $NaBH_4$, resulting in enhanced active sites and an improved conductivity of Bi_2O_3. The O 1s XPS spectra exhibit a peak at approximately 531.8 eV, corresponding to oxygen defects in the prepared material (Fig. 10b).[141] Compared with Bi_2O_3/GN, r-Bi_2O_3/GN exhibits a higher intensity in the oxygen-defect peak, indicating a greater induction of oxygen defects in Bi_2O_3 after reduction. In a separate investigation, the induction of surface OVs in $BiOIO_3$ was achieved by treating the sample with a KI solution under continuous stirring for 14 hours at room temperature[142] (Fig. 10c). The sample prepared with 0.2×10^{-3} M KI was denoted as BIO-LOV$_2$. Fig. 10d and e illustrate the identification of the created OVs through

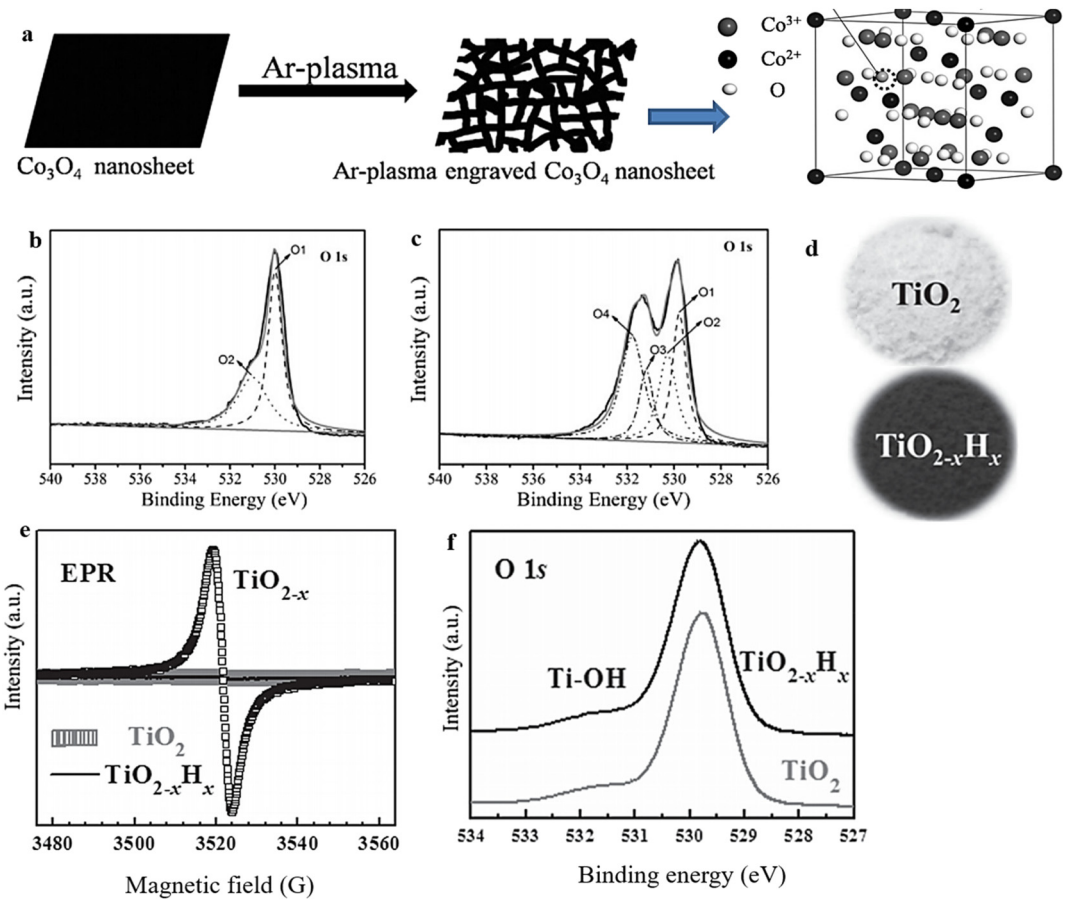

Fig. 9 (a) Illustration of the process for producing oxygen-vacancy-rich, high-surface-area Co_3O_4 that was etched using Ar-plasma. (b) and (c) XPS 1_S spectra of pristine Co_3O_4 and plasma-engraved Co_3O_4 respectively. Reproduced from ref. 114 with permission from Wiley, copyright 2016. (d) Photographs of pristine TiO_2 and black titania (TiO_{2-x} H_x). (e) and (f) EPR and XPS 1 Os spectra of pristine and OV-rich TiO_2 samples. Reproduced from ref. 139 with permission from Wiley, copyright 2013.

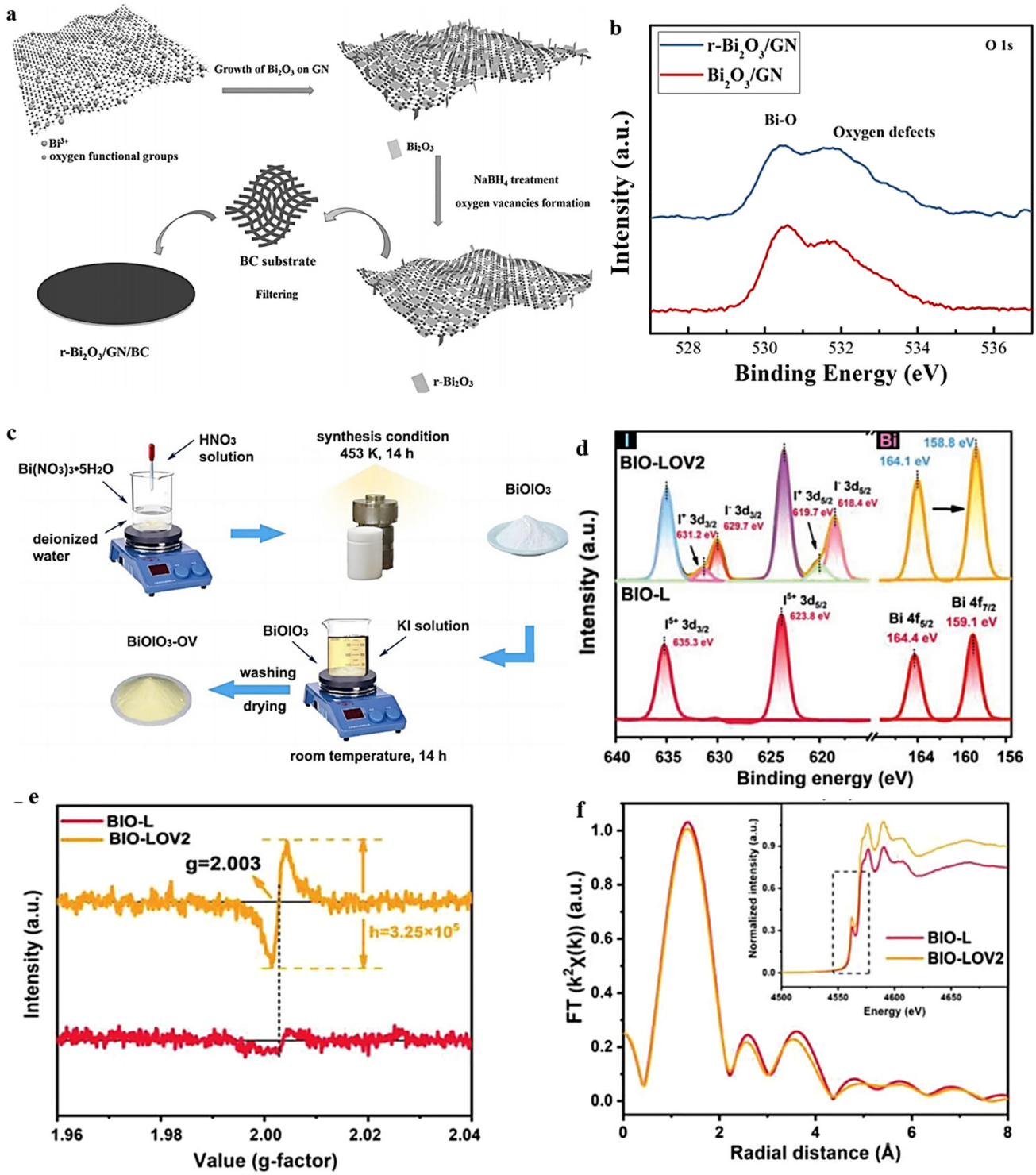

Fig. 10 (a) Schematic diagram showing the steps used to create a flexible r-Bi_2O_3/GN/BC electrode during the synthesis process. (b) XPS analysis Bi-O. Reproduced from ref. 140 with permission from Wiley, copyright 2017. (c) Schematic illustration for the preparation process of $BiOIO_3$ and $BiOIO_3$-OV samples. (d) The XPS of I 3d and Bi 4f. (e) EPR spectra and (f) Fourier-transform curves of EXAFS of BIO-L and BIO-LOV_2. Reproduced with permission.[142]

XPS and EPR analyses. The presence of lower-valence iodine ions (I^+ 3d3/2, I^+ 3d5/2, I^+ 3d3/2, and I^- 3d5/2) in BiO-LOV_2 serves as evidence for the existence of OVs (Fig. 10d).[143,144] Additionally, an XAS investigation was conducted to examine the modifications in the electronic states of the I element in the prepared samples. A notable distinction was observed

between BIO-L and BIO-LOV_2, with the I element in BIO-LOV_2 exhibiting a slight shift towards lower energy. This shift indicates a change in the valence state from I^{5+} to I ($^{(5-x)}$). The Fourier transform of BIO-LOV_2 displays a decrease in peak intensity, which can be attributed to a surface structural deformation resulting from the reduction of adjoining oxygen atoms around the I atoms (Fig. 10f). These findings follow the XPS and EPR data,[145,146] further supporting the presence of such surface structural changes. The results above, taken together, provide evidence of the presence of surface OVs in BIO-LOV_2. These OVs primarily originate from a lack of O atoms within the IO_3 polyhedra.

4.4 Hydrogen treatment

Hydrogen exhibits remarkable reducing capabilities, enabling it to selectively reduce specific metal ions to a lower oxidation state while simultaneously generating OVs in the resultant material. Compared with the thermal protocol in an oxygen-deficient condition, the hydrogenation procedure represents a simpler approach to generate OVs and transform different metal oxides (MOs) into their respective nonstoichiometric forms, as described in the following equation;

$$MO + \frac{x}{2}H_2 = MO_{1-x}(OH)_x$$

The generation of OVs can potentially occur through a mechanism where electrons from the reducing agent are induced into the d orbitals of metals, resulting in a significant weakening of the metal–oxide bonds.[77] As a result, the oxygen atoms have two potential routes to exit the crystal lattice: they can either form water vapor (in the presence of a hydrogen flow) or bond with metal atoms to create more stable oxides like Al_2O_3 or MgO.[147,148] Additionally, alongside the generation of oxygen vacancies, there is a notable reduction in the metal ions. For example, in 2011, a novel black TiO_2 variant was discovered due to subjecting it to high-pressure treatment with H_2. This transformation was attributed to the formation of Ti^{3+} and OV, which reduced the bandgap (Fig. 11b and c).[149] Furthermore, a more rigorous treatment involving magnesium metal and H_2 flow produced oxygen vacancy ZrO.[147] The evident color alteration observed in the samples (white to black), the shift in the chemical state of Zr, and the bandgap reduction (as depicted in Fig. 11e and f) provide evidence for the formation of oxygen vacancies.

4.5 Electrochemical reduction

There is an ongoing debate regarding the reduction process involving the application of reducing agents in the H_2 treatment procedure. One argument suggests that when TiO_2 is

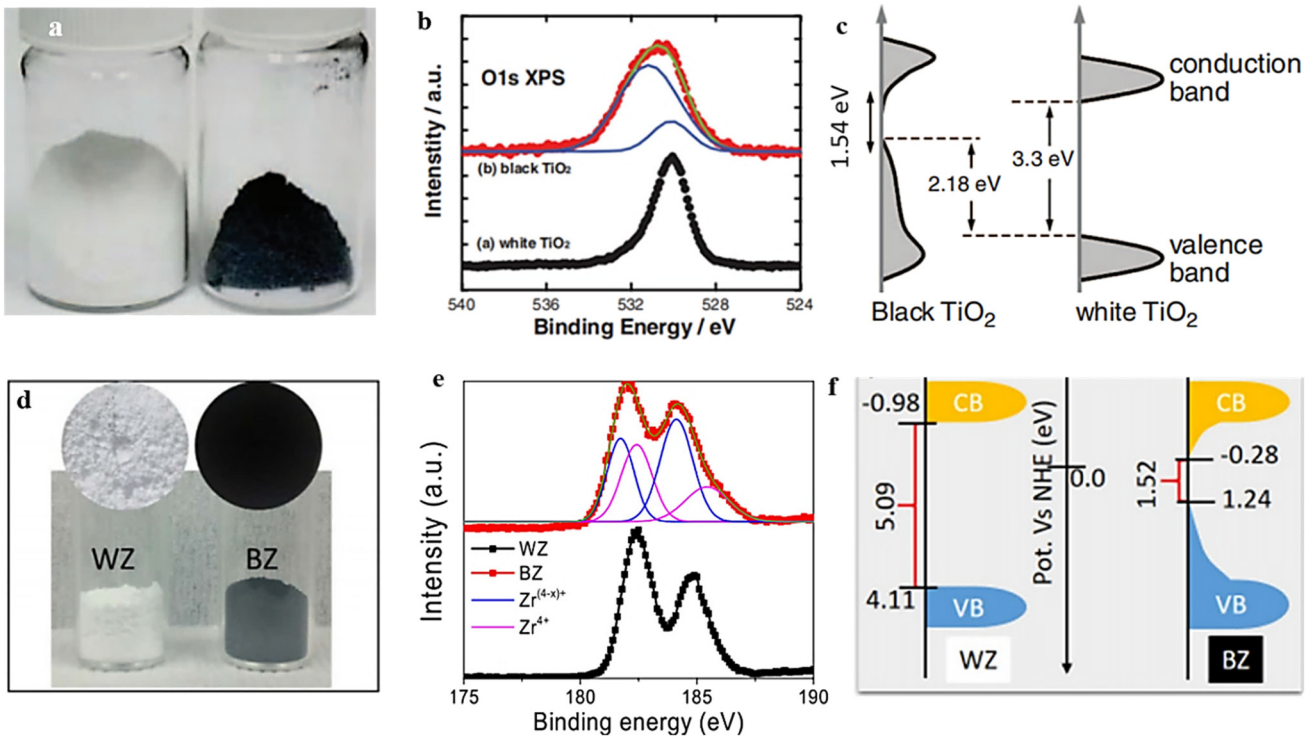

Fig. 11 (a) This image shows TiO_2 nanocrystals in their natural white and disorder-engineered black nanocrystals. (b) TiO_2 O 1s XPS spectra, both white and black. (c) Diagram comparing the DOS of disorder-engineered black TiO_2 nanocrystals with that of unmodified black TiO_2 nanocrystals. Reproduced from ref. 149 with permission from the American Association for the Advancement of the Science, copyright 2011. (d) A photograph of the powder samples, illustrating the difference in color between the white (WZ) and black (BZ) ZrO. (e) Zr 3d XPS spectra of WZ and BZ. (f) The most likely band energy diagrams of zirconia samples in black (BZ) and white (WZ) samples. Reproduced from ref. 147.

treated with hydrogen, H atoms can be inserted into its lattice, potentially creating an interstitial H (Hi) doped structure.[150] To circumvent any potential problems arising from reduction agents, an alternative approach is to introduce electrons directly into MOs *via* an electrochemical method. This method is commonly employed to induce OVs in MOs. The utilization of this approach provides a promising substitute that brings forth numerous benefits, including a swift reaction time, affordability, and convenient operation at lower temperatures. By manipulating electrochemical factors like voltage, reaction time, and current density during the procedure, precise control over the content of OVs in metal oxide catalysts can be achieved. Research has shown that OVs have been induced in various materials *via* electrochemical reduction protocols.[151–153]

Guo *et al.*[154] successfully synthesized a wide variety of materials rich in OVs by implementing the converse voltage utilization technique. Using $Co(OH)_2$ as a case study, we present an exemplified protocol to demonstrate the designed procedure in this paper. In the initial stage of the procedure, carbon paper served as a substrate for the electrochemical deposition of $Co(OH)_2$ nanosheets using a voltage of −1.5 V. This step resulted in the formation of hybrids known as Co-OH (Fig. 12a). Subsequently, a converse voltage of 1.5 V was applied, producing CoOOH nanosheets with high activity and an abundance of defects. Throughout this process, the $Co(OH)_2$ underwent partial oxidation and *in situ* conversion, resulting in the generation of EA-CoOOH (Fig. 12b and c), which exhibited significant oxygen vacancies and defects (Fig. 12d and c). Wang and colleagues employed a straight-

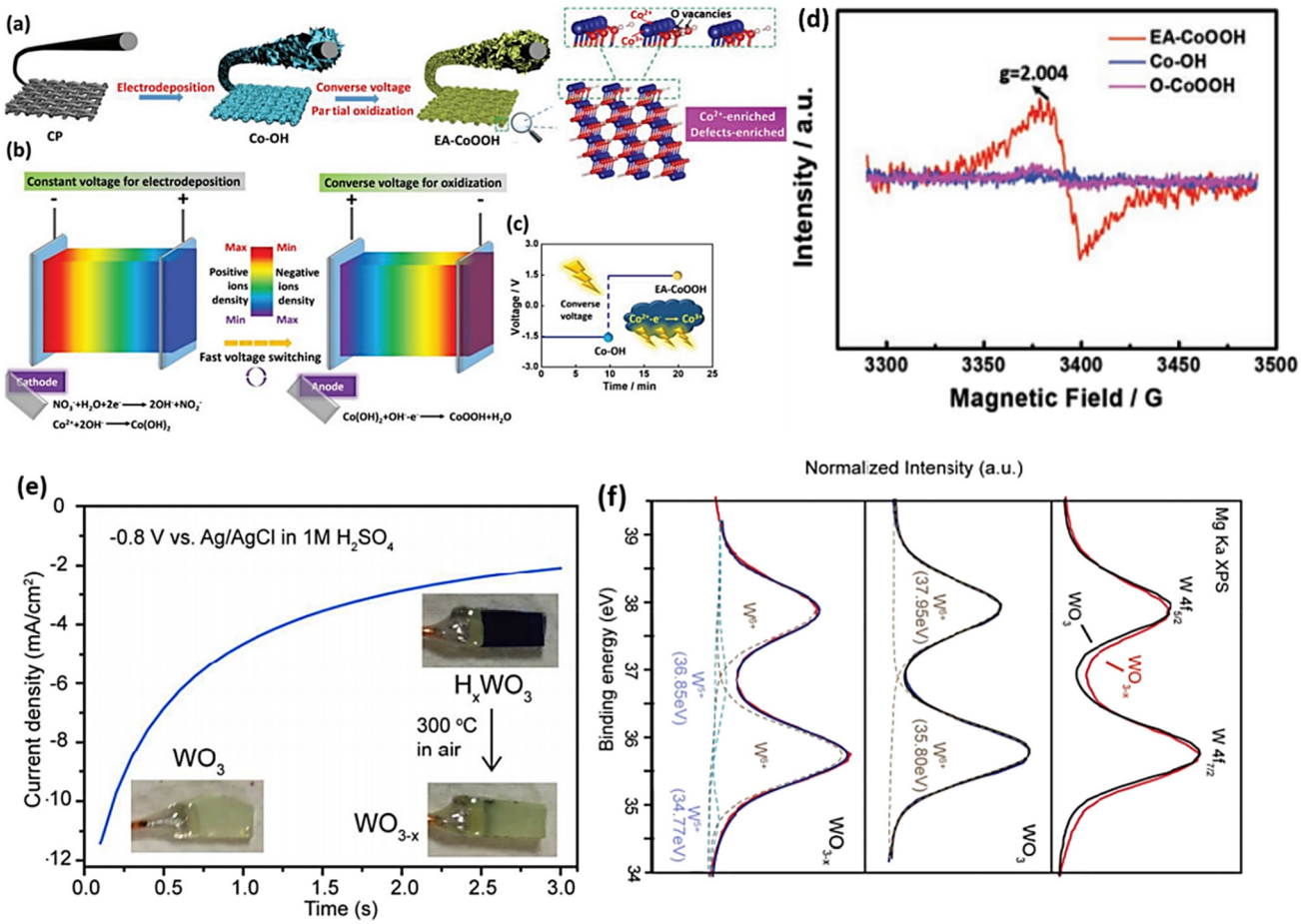

Fig. 12 (a) The molecular structure of EA-CoOOH exhibiting Co^{2+} and defect-enriched characteristics is shown schematically, and its synthesis through the converse voltage approach is also described. (b) Schematic representation of the process, showing a constant voltage used for electrodeposition and a reverse voltage used for oxidation. (c) Electrodeposition voltage and time employed schematic and reverse voltage process stages. (d) Spectra obtained by EPR from the as-prepared materials. Reproduced from ref. 154 with permission from Wiley, copyright 2019. (e) After being exposed to 1 M H_2SO_4 solution at −0.8 V *vs.* Ag/AgCl for 3 s, the cathodic current *vs.* time curve of the WO_3 film decreased. Inset: the electrochemical reduction of a light yellow WO_3 film results in a blue $HxWO_3$ film, which is then re-oxidized into WO_{3-x} when exposed to air. (f) Upper: WO_3 and WO_{3-x} XPS W 4f spectra after normalization. The synthetic peaks in the XPS W 4f spectrum of WO_3 that correspond to the W 4f5/2 and W 4f7/2 signal of W^{6+} are shown in the middle of the figure. The experimental data and the total of the synthetic peaks are shown by the black and blue curve. Synthetic peaks may be seen in the XPS W 4f spectrum of WO_{3-x} at the bottom. The red line represents the experimental data, which have been decomposed into two sets of peaks representing W^{6+} and W^{5+} (the dashed lines). The blue line represents a cumulative peak de-convolution. Reproduced from ref. 155 with permission from RSC, copyright 2016.

forward electrochemical reduction technique to produce a range of metal oxides integrated with OVs, namely WO_3, TiO_2, ZnO and $BiVO_4$.[155] In this study, we use WO_3 as a specific example to demonstrate the induction of OVs using the technique employed. The metal oxides treated electrochemically showed enhanced photoactivity compared with their prisitine states. This improvement can be attributed to the creation of oxygen vacancies. The identification of these oxygen vacancies was confirmed by analyzing the XPS data, which revealed a decrease in the valence state of W in OV-WO_3 (Fig. 12f).

4.6 Elemental doping

Doping with appropriate elements is a widely employed and strongly favored method for introducing oxygen vacancies into metal oxides. Extensive research has demonstrated that the presence of OVs varies considerably depending on the doping of diverse metal elements.[156–160] Doping elements in MOs can provide a wide range of options when considering dopants with similar ionic sizes and high solubility characteristics. Using a plasma technique, Huang and colleagues.[53] successfully created Mo-substituted Co_3O_4 nanoneedles on carbon cloth (Mo-Co_3O_4@CC), as depicted in Fig. 13a. The addition of Mo resulted in the induction of OVs, which were verified through XPS and EPR analysis. Theoretical investigations demonstrated that the presence of Mo with varying oxidation states effectively controlled the Co^{3+}/Co^{2+} atomic ratio and increased the abundance of OVs. As a result, this caused a reallocation of charges and the modulation of the d-band center of Co_3O_4, as depicted in Fig. 13b. Jiang *et al.*[161] prepared CuO doped with Sn through hydrothermal treatment. The incorporation of Sn led to the generation of OVs, which were confirmed through XPS and EPR analysis. Theoretical investigations indicate that the energy barrier for CO adsorption dimerization is reduced by Sn doping, and it effectively stabilizes the *CO and *OCCO species (Fig. 13d).

Moreover, it was observed that Sn alone is insufficient to achieve the desired outcomes. However, the combined effects

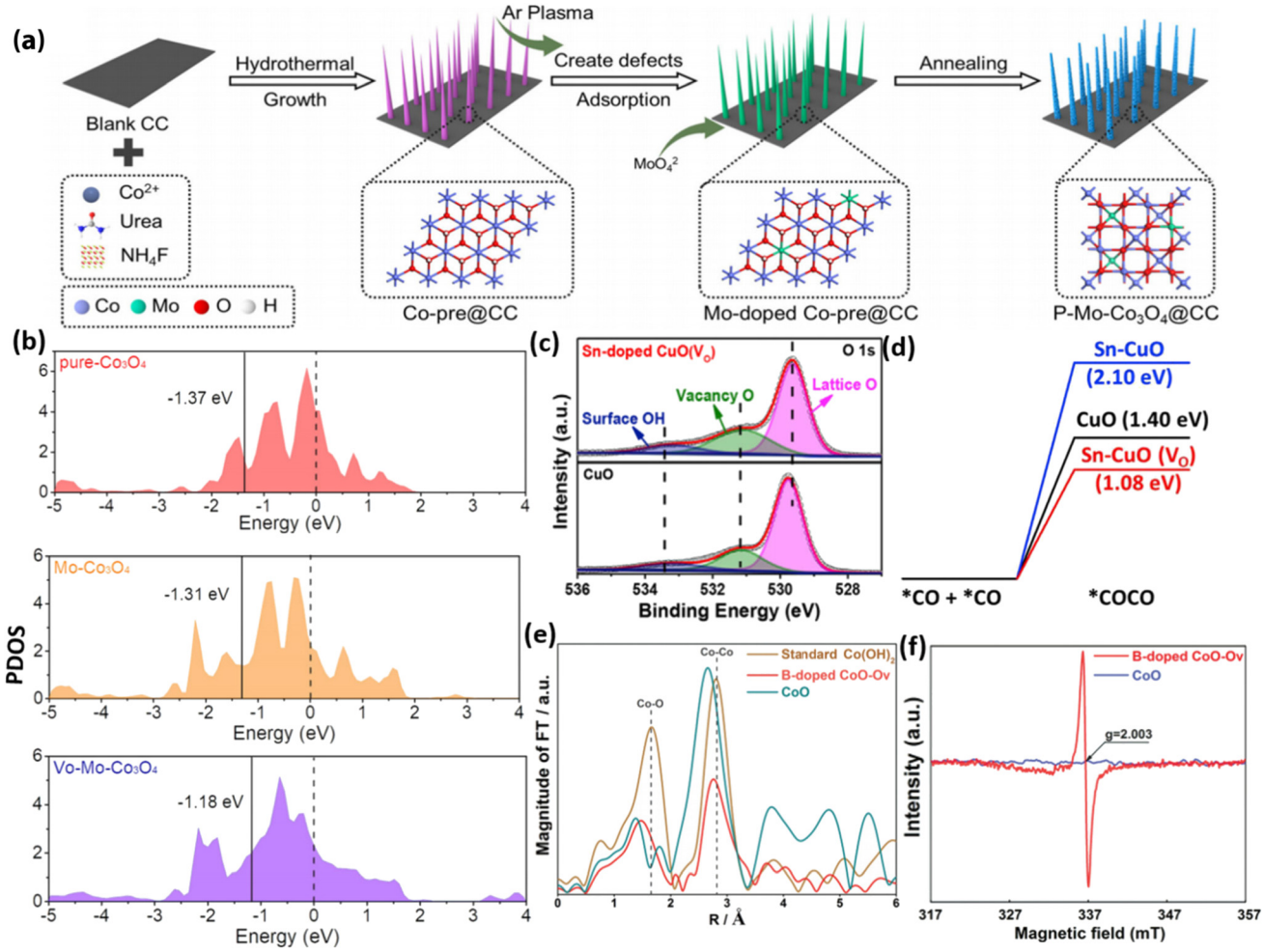

Fig. 13 (a) The figure provides a schematic depiction of the synthesis process for P–Mo-Co_3O_4@CC. (b) PDOS of pure-Co_3O_4, Mo-Co_3O_4, and V_O-Mo-Co_3O_4. Reproduced from ref. 53. (c) XPS O 1s spectra of CuO and CuO that have been doped with Sn (V_O). (d) Diagram illustrating the amount of energy required for CO dimerization (*CO + *CO *OCCO) on CuO (black), Sn-CuO (blue), and Sn-CuO(VO) (red). Reproduced with permission.[161] (e) The spectra were obtained using the Fourier transform at the Co K-edge for B-doped CoO-Ov, CoO, and conventional $Co(OH)_2$. (f) Spectra of EPR for B-doped CoO-OV and CoO. Reproduced from ref. 162 with permission from Elsevier, copyright 2021.

of Sn doping and OVs are the key contributors to enhanced catalytic activity. In the investigation by Zhang *et al.*[162] it was reported that the incorporation of non-metal elements can trigger the formation of OVs in the engineered material, as depicted in Fig. 13c. This was demonstrated by synthesizing CoO nanowires containing OVs by adding B using a straightforward pyrolysis technique. The evidence from EPR and XAS analysis supports the notion that the OVs in CoO primarily stem from the perturbation of the local structure induced by B doping (Fig. 13e). In summary, extensive investigations have demonstrated that metal and nonmetal dopants can generate OVs in metal oxides, leading to improved conductivity and rapid ion and electron transport. Nevertheless, the precise control of dopant concentration and spatial distribution within nanostructures of MOs has remained a persistent challenge.

Based on recent literature, the synthesis methods for creating OVs in metal oxide catalysts, along with the corresponding techniques to detect OVs, are summarized in Table 1. These approaches are widely used for introducing vacancies in metal oxides.

5. Recent progress in OV-based electrocatalysts in electrochemical NO_3^- reduction to NH_3

Modifying the electronic structure is crucial for optimizing the electrocatalytic activity, and one way to achieve this is through vacancy engineering. By introducing OVs, the electronic arrangement of the host materials can be modified, leading to local rearrangements of spin/charge density and facilitating of the adsorption of intermediates.[170] It is believed that the presence of OVs in TiO_2 can enhance the bonding between Ti^{3+} and oxygen, improving its ability to reduce the oxygen.[171] Based on this reasoning, it seems plausible that metal oxides containing OVs could effectively capture and electrochemically reduce nitrate. Nevertheless, there have been few reports on the investigation of OV-rich oxides as prospective electrocatalysts for ammonium synthesis through nitrate electroreduction. Additionally, as the number of OVs in a nanomaterial increases, so does its electrochemical performance. Recognizing the significance of OVs in metal oxides, Jia *et al.*[105] investigated the impact of OVs on the adsorption energy of NO_3^- on the $TiO_2(101)$ surface by varying the number of OVs from zero to one and two in TiO_{2-x}. The OVs were formed by subjecting the TiO_2 to a heating process at a rate of 5 °C per minute until it reached a temperature of 700 °C. It was then maintained at 700 °C for 4 hours under a hydrogen atmosphere, followed by a cooling phase (Fig. 14a). XPS and EPR investigations, depicted in Fig. 14b and c, provided evidence substantiating the formation of OVs within the specified material. The electrochemical performance results revealed a notable decline in adsorption energy as the concentration of OVs increased. Specifically, the adsorption energy decreased from −0.71 eV to −1.44 eV and −1.54 eV, respectively (Fig. 14d). The experimental findings revealed that TiO_{2-x} exhibited a two-fold increase in the yield rate, in addition to a high faradaic efficiency and ammonium selectivity for the electrochemical synthesis of ammonia, with respective values of 0.045 mmol h^{-1} mg^{-1}, 85.0%, and 87.1% when operated at −1.6 V *vs.* SCE. This performance significantly surpassed pristine TiO_2 under identical conditions, which recorded 0.024 mmol h^{-1} mg^{-1}, 66.3%, and 66.9% (Fig. 14e and f). This was achieved by eliminating bridge O, which produced active sites on the top surface of $TiO_2(101)$. The NO_3^- ions were prone to accumulate and be captured at these active sites, where their O atoms filled the vacancies while the adjacent unsaturated Ti^{3+} sites trapped another O atom. The presence of numerous OVs in TiO_2 nanotubes caused a shift of the Fermi energy (E_f) towards the CBM (conduction band minimum) by occupying the excess 3d electrons of Ti, as reported by the authors. This resulted in the emergence of metallic properties and increased the conductivity in the TiO_{2-x}. It is logical to assume that the engineering of OVs could enhance the conducting property of electrocatalysts for NO_3RR and the electron/proton transfer steps.

In line with these findings, Daiyan *et al.*[47] noted a comparable tendency where the introduction of additional OVs (three OVs) in CuO lowered the adsorption energy, which in turn facilitated a noteworthy adsorption of NO_3^-. The introduction of OVs aimed to expose more catalytic sites that can be utilized during the electrocatalytic process. The adsorption energy of NO_3^- on CuO(111) increased from −0.93 eV to −0.5 eV with the addition of one OV. Interestingly, as the number of OVs increased, the adsorption energy significantly decreased to −1.84 eV (two OVs) and −2.08 eV (three OVs), as shown in Fig. 14i. These results suggested that an "adequate amount" of OVs within CuO_x is energetically advantageous for NO_3^- adsorption, thereby impeding the adsorption of other competing anions on the catalyst surfaces. According to the authors, the defects formed during the process promoted the most energetically favorable path for ammonia production, wherein the crucial step involved the adsorption of nitrate ions with the release of −1.87 eV (CuO with two OVs) and −1.5 eV (Cu_2O), at −0.6 V *vs.* RHE. Furthermore, it was observed that introducing OVs beyond 1 raises the free energy of H*, which promotes the NO_3^- RR while making the HER more challenging (Fig. 14j). The oxygen-rich vacancy CuO_x that was prepared with 5 min plasma treatment (pCuO-5) demonstrated exceptional performance, yielding 292 μmol cm^{-2} h^{-1} of NH_4^+ (−0.6 V *vs.* RHE) and FE of 89% at −0.5 V (Fig. 14h). Based on the AES, XPS, and HRTEM data, it was inferred that an excessive amount of OVs on the CuO_x surface led to a decrease in electron density, reduction in surface crystallinity, and alteration in the surface chemical state.

Combining and forming OVs within a dual-cation framework is a promising approach to improve the electrochemical capabilities of the catalyst, resulting in a higher efficiency in converting NO_3^- to NH_3. Prior studies have demonstrated that TiO_2 containing vacant oxygen sites exhibits an exceptional

Table 1 Summary of commonly used approaches to construct OVs in metal oxides

Synthesis method	Catalysts	Detection techniques	Description of methods	Ref.
Calcination	(TiO_{2-x})	XPS, EPR	20 minutes of H_2 gas purging of TiO_2. Heating at a rate of 5 °C min^{-1} to 700 °C, then holding at that temperature under a H_2 atmosphere for 4 hours.	105
Plasma treatment	CuO	HAADF, Raman, XAS, EPR	Flame spray pyrolysis (FSP) was used to atomize a copper precursor solution using 5 mL min^{-1} of oxygen. A 30 mL min^{-1} He flow was used to introduce the resulting product into a reaction cell, where it was subjected to a plasma treatment for 5 and 10 minutes.	47
Electrospinning, calcination	Fe_2TiO_5	Raman, XPS, EPR,	To a 1.2 g PVP solution in 5 mL of DMF and 5 mL of ethanol, 1.212 g of $Fe(NO_3)_3{\cdot}9H_2O$, and 0.45 mL of butyl titanate were added and stirred for 24 h. The solution was then electrospun (20 kV). After electrospinning, the materials were heat-treated at 250 °C for 1 h and calcined at 650 °C for 3 h.	103
Calcination	a-RuO_2	XPS, XAS, Raman	20.0 mg ruthenium acetylacetonate ($Ru(acac)_3$) and 37.5 mg potassium bromide were dissolved in a 15.0 mL ethanol and distilled water mixed solution. A piece of carbon paper treated at 60 °C for 24 h using water, concentrated nitric acid, and concentrated sulfuric acid was immersed in the abovementioned mixed solution. The solution was dried at 50 °C until the liquid evaporated. Finally, the carbon paper with the dark red precipitates on the surface was heated in a tube furnace at 260 °C for 30 min with a heating rate of 5 °C min^{-1} under air.	163
Ar plasma	Cu_2O	XPS, XAS, EPR	Treatment times for the pure Cu_2O ranged from 20 to 60 minutes in Ar plasma. The plasma treatments were conducted in a 20 Pa-pressured vacuum chamber, with a radio frequency generator power of 200 W.	164
Elemental doping	Fe-TiO_2	XPS, EPR, Raman	0.1 g of the prepared TiO_2 was added into 10 mL of CH_3CN solution containing 30 mg of $Fe(acac)_3$. The obtained powders after filtration were dried at 70 °C in a vacuum for 6 h and calcined at 350 °C for 2 h under a reducing atmosphere (5 vol% hydrogen and 95 vol% argon) to obtain Fe-TiO_2 electrocatalysts.	165
Calcination	$LaCoO_3$. $LaMnO_3$, $LaCrO_3$, $LaFeO_3$	XPS, EPR	$La(NO_3)_3{\cdot}H_2O$ (2 mmol) and $Co(NO_3)_2{\cdot}6H_2O$ (2 mmol) were dissolved in 70 mL water. Then, $C_6H_8O_7$ (6 mmol) and $C_{10}H_{16}N_2O_8$ (4 mmol) were added as complexing agents. The pH of the mixed solution was adjusted to alkaline by adding$NH_3{\cdot}H_2O$ dropwise. Afterward, the solution was heated at 90 °C under stirring and slowly evaporated to obtain the gel. The resulting gel was roasted at 250 °C for 5 h to form a solid precursor and then calcined at 800 °C for 10 h in air. The precipitates were collected and ground to obtain a $LaCoO_3$ perovskite. The same procedure was used for the rest of the catalyst.	84
Nano-crystallization	TiO_2	XRD, XPS, UV-Vis DRS	$Ti(SO_4)_2$ was reacted with ammonia water in an ice-water bath for 2 hours, and then TiO_2 was obtained after centrifuging, washing, and drying the solution at 80 °C. The produced TiO_2 was subjected to an ultrasonic treatment at 80 °C for varying times (0.5 h, 1 h, 2 h, 4 h, and 8 h) with an output power density of 1500 W/100 mL.	166
Nano-crystallization	Bi_2O_3	HAADF STEM, XPS, ESR, PL	Hydrothermal treatment at 453 K for 12 hours was applied to a mixture of 800 mg bismuth, 60 mg propylamine, and 30 mL benzyl alcohol. Following centrifugation, 400 mg of the precipitates were redissolved in 100 mL of a 1 : 1 solution of isopropanol and water.	167
Elemental doping	MoO_3/Ce	XPS, EPR, PAS	In a cold water bath, 5×10^3 molar Mo powder was added to 10 mL of H_2O_2. While still stirring, 50 mL of deionized water and 10 mL of 100% ethanol were added to the aforementioned mixture. Then, $Ce(NO_3)_3{\cdot}6H_2O$ was added, and the mixture was agitated for a further 2 hours. The combined solution was heated to 140 °C for 18 hours to react. Collecting the dark blue goods, we cleaned them in deionized water and pure ethanol. The samples were then dried in an oven at 60 degrees celsius for 12 hours.	109
Elemental doping	Fe-TiO_2	XPS, EPR, XAS	600 mg of PVP dissolved in 5 mL of ethanol was stirred for 2 h at 60 C. 1 mL of acetic acid was added and stirred for 30 minutes. Then tetrabutyl titanate containing different mole fractions of acetylacetonate iron was added and stirred for 1 h. The final mixture was subjected to electrospinning under a 20 kV voltage at the rate of 2 mL h^{-1}. The obtained membrane was annealed at 550 °C for 2 h and held at 800 °C for 1 h with a heating rate of 5 °C min^{-1} in air.	168

Table 1 *(Contd.)*

Synthesis method	Catalysts	Detection techniques	Description of methods	Ref.
Plasma treatment	InOOH	XPS, EPR, HAADF-STEM	270 mg of $In(NO_3)_3{\cdot}4H_2O$ and 2 g of urea in 60 mL of ethanol were stirred. Then, 65 mg of CB (commercial XC-72R) was added, subjected to ultrasound treatment for 30 min, and heated at 90 °C for 12 h. The resulting sample was filtered, washed and dried at 60 °C for 12 h under a vacuum. The as-prepared InOOH was subjected to Ar plasma for 2 min to induce OVs in InOOH.	169
Self-assembly solvothermal method	$Bi_{24}O_{31}Br_{10}$	XPS, EPR, STEM and XAFS	0.243 g bismuth nitrate pentahydrate, 0.27 g mannitol and 0.2 g polyvinyl pyrrolidone (average mol wt 40 000) are added into 15 mL water and ultrasonicated. Then, the 3 mL KBr solution (0.5 mmol KBr) is injected under stirring. The pH is adjusted to 7.5 by 2 M sodium hydroxide solution and stirred for 0.5 h. After solvothermal treatment for 24 h under 160 °C, the sample is collected, washed with hot ethanol and water, and dried.	91

Table 2 The advantages and significance of the NO_3RR compared with other electrochemical NH_3 synthesis routes[238,242]

N_2 electrochemical reduction	NO electrochemical reduction	NO_3^- electrochemical reduction
• The solubility challenge of the conventionally used inert N_2 has consequences for the generation of ammonia (NH_3) in aqueous environments.	• The challenge of solubility in aqueous solutions directly impacts ammonia (NH_3) production.	• Nitrate ions (NO_3^-) have gained prominence as a significant nitrogen source in contrast to the conventionally inert N_2 for the electrochemical generation of NH_3, contributing to their widespread prevalence as water pollutants across the globe.
• The considerable energy needed to break the bonds in N_2 makes it economically unfeasible for the electrochemical production of NH_3.	• Environmental samples typically contain a low concentration of NO, necessitating an additional energy-intensive step to concentrate it for the electrochemical reaction.	• The low bond dissociation energy in NO_3^- renders this molecule an appealing candidate for NH_3 synthesis.
• Most catalysts investigated exhibit a low yield rate and low faradaic efficiency (FE). Thus, while utilizing N_2 gas as the nitrogen source for electrochemical NH_3 synthesis holds promise, it still requires significant progress to achieve substantial yields suitable for practical applications.	• Non-precious metal-based catalysts exhibit a drawback in the form of low yield rates and faradaic efficiency (FE). Nevertheless, achieving the practical implementation of cost-effective and long-lasting catalysts remains a distant aspiration.	• A broad range of electrocatalysts have shown noteworthy improvements in both faradaic efficiency (FE) and yield rates.
• The reaction potential closely aligns with that of the hydrogen evolution reaction (HER). As a result, the electrochemical reduction of N_2 is significantly hampered by the HER.	• Most of the investigated catalysts produce side products alongside the reduction of NO to NH_3. Further advancements in catalyst design are necessary since the reduction of NO to NH_3 is still in an early developmental stage.	• There is a significant disparity between the reaction potential of NO_3^- (0.69 V) and that of the hydrogen evolution reaction (HER). Therefore, the reduction of NO_3^- to NH_3 successfully circumvents the impediments posed by the hydrogen evolution reaction (HER). • Lastly, the presence of NO_3^- in water samples poses a threat to human health, and the transformation of this waste into a valuable product holds significant importance, serving both environmental remediation and the production of versatile chemicals.

electrochemical performance.[106,172] Iron (Fe), a key component in the Haber–Bosch process, has been identified as a potential catalyst for nitrate reduction. In a recent study, Du *et al.*[103] were inspired by the double-cation model and proposed the use of defective pseudobrookite Fe_2TiO_5 nanofiber (FTO-E) as a new electrocatalyst to reduce nitrate to ammonia under ambient conditions. This electrocatalyst was prepared using the electrospinning technique and contains abundant oxygen vacancies (Fig. 15a and i). Oxygen vacancies in the prepared material were confirmed through spectral analyses using the XPS and EPR techniques (Fig. 15j and k). The higher intensity of the ESR signal suggests a greater number of oxygen vacancies (V_O) formed in FTO-E than in FTO-H (FTO prepared by the hydrothermal method). This observation is likely due to the tendency of high-reducibility Fe^{3+} ions to replace Ti^{4+} ions, thereby inducing the formation of oxygen vacancies. The density of states calculations have revealed that introducing OVs into FTO significantly enhances its conductivity, with electronic contributions from O and Fe atoms evident based on the band contribution calculations (Fig. 15l and m). Moreover, the d-band center (ε_d) is observed to shift to a higher level upon generating a V_O, which contributes to the catalyst's higher catalytic activity. The thermodynamic study indicates that the adsorption of the NO_3^- group on pristine FTO results in a free energy of 0.09 eV, significantly reduced to −0.28 eV upon adding V_O (Fig. 15n). In contrast, the adsorption energies

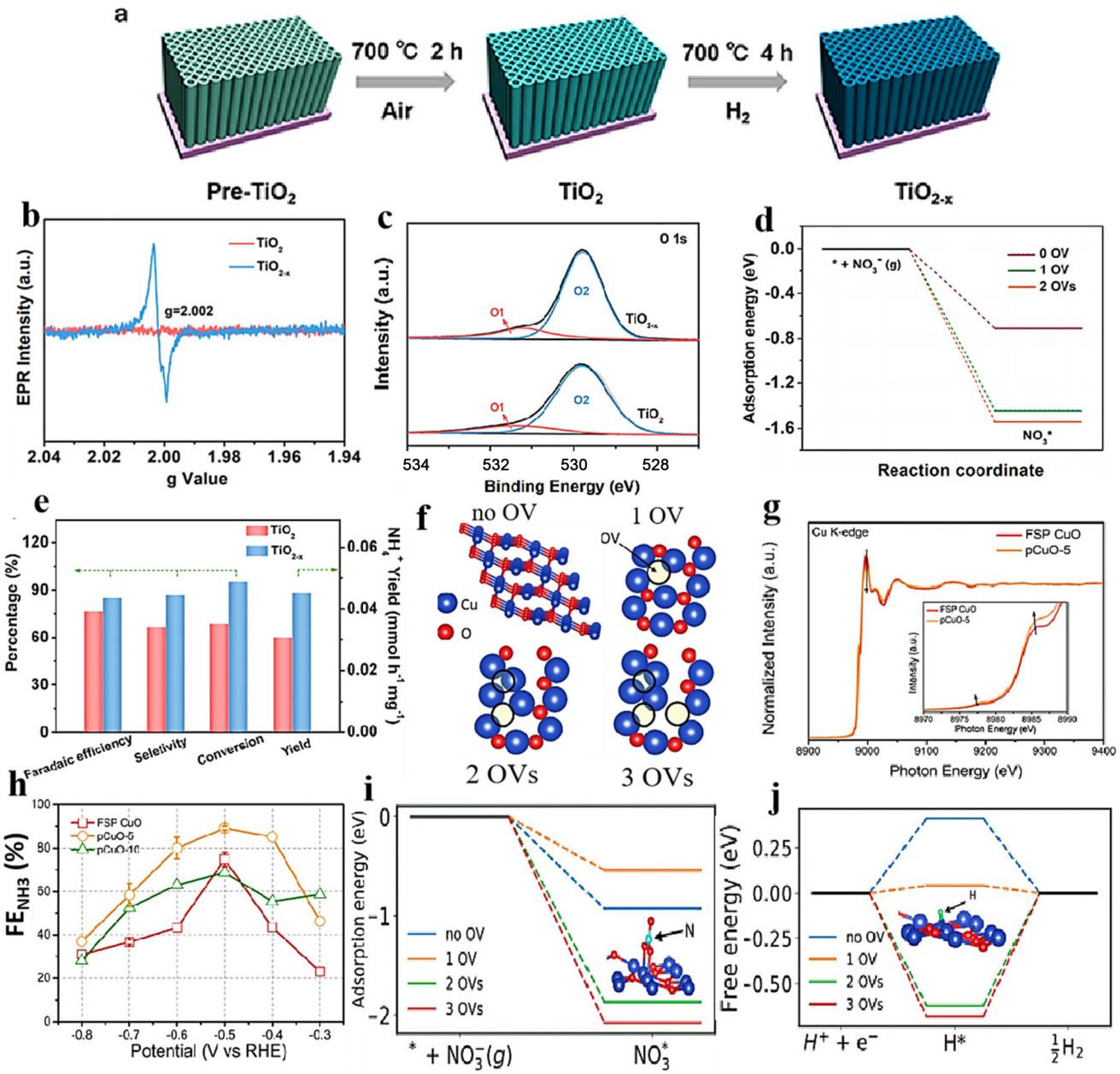

Fig. 14 (a) TiO_{2-x} synthesis diagram. (b) EPR spectral analysis. (c) TiO_2 and TiO_{2-x} XPS spectra. (d) Energy required for NO_3^- adsorption on TiO_2(101) surfaces with 0 OVs, 1 OVs, and 2 OVs. (e) TiO_{2-x} and TiO_2 were compared with respect to their NH^{4+} FE, selectivity, yield, and NO_3^- conversion rate. Reproduced from ref. 105 with permission from the American Chemical Society, copyright 2020. (f) Top view of the relaxed structures of the CuO (111) surface with 1, 2, and 3 OVs, with the missing oxygen atoms indicated by the circles in the pristine CuO(111) slab model used in DFT calculations. (g) XANES spectra obtained experimentally near the Cu K edge, as well as enlarged curves (insets) of FSP CuO and pCuO-5. (h) The dependency of the $FE_{NH^{4+}}$ concentration on the applied potential for FSP CuO, pCuO-5, and pCuO-10 in 0.05 M KNO_3 and 0.05 M H_2SO_4. (i) NO_3^- adsorption energies on CuO(111) were calculated for 0 OVs, 1 OVs, and 3 OVs. (j) The corresponding HER free energy diagram. Reproduced from ref. 47 with permission from RSC, copyright 2021.

of NO_3^- on pristine TiO_2 and TiO_2-VO are much higher, at 1.52 eV and 0.45 eV, respectively, compared with the 0.28 eV value observed for FTO-V_O. The electrochemical efficiency of the FTO-E catalyst was studied and it was observed that at −1.0 V *vs.* RHE, it achieved a high FE of 87.6% and a large NH_3 yield of 13.3 mg h^{-1} mg_{cat}^{-1}. These values were further enhanced to 96.06% and 1.36 mmol h^{-1} mg_{cat}^{-1} at 0.9 V *vs.* RHE (Fig. 15o). The catalytic importance of iron (Fe) has also been evidenced across multiple catalysts employed in the electrochemical process of reducing nitrate to ammonia. For example, the introduction of Fe doping into V_2O_5 (resulting in Fe-V_2O_5) has been documented to generate Lewis acid sites on the catalyst's

surface, leading to an increased electrochemical conversion of nitrate to ammonia.[173] Similarly, the incorporation of Fe within FeB_2-based MBenes has been observed to greatly elevate the catalytic capabilities of the tandem MBene catalyst.[174,175]

The degree of structural disorder is crucial for a catalyst's catalytic performance, yet its impact on NO_3^- reduction is often overlooked. It is crucial to investigate how the level of disorder affects the electrocatalytic NO_3^- reduction performance. To tackle this issue, Wang *et al.*[163] created a-RuO_2, which comprises amorphous RuO_2 nanosheets grown on a carbon paper substrate, using a straightforward molten-salt preparation method. To facilitate a comparison with a-RuO_2, the researchers prepared two variations of RuO_2 with different degrees of crystallinity, referred to as lc-Ru_2O (low crystallinity) and hc-RuO_2 (high crystallinity). Structural disorder in the prepared samples was identified through an investigation using EXAFS (extended X-ray absorption fine structure). The values obtained from the EXAFS spectral study confirmed the formation of structural disorder in the samples (Fig. 16f). The XPS study successfully identified the presence of OVs, and it

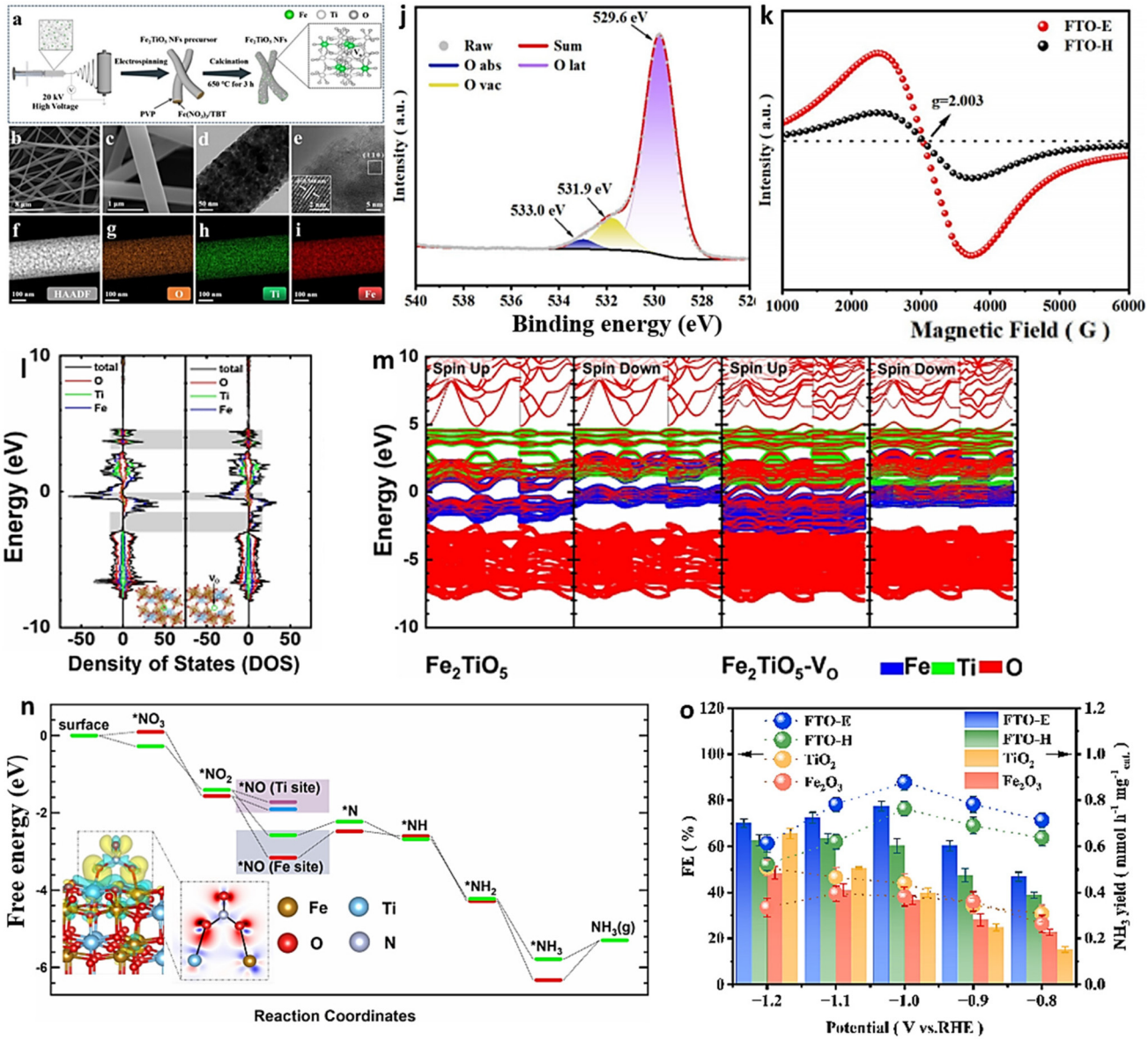

Fig. 15 (a) Illustration of the schematic for the manufacturing process of the FTO-E electrocatalyst. (b) and (c) Images of FTO-E taken at different SEM magnifications. (d) TEM analysis of FTO-E. (e) HR-TEM photo of FTO-E. (f) HAADF STEM image and EDX mapping of the O (g), Ti (h) and Fe (i) elements in FTO-E. (j) XPS spectra of O in FTO-E. (k) EPR spectra of FTO-E and FTO-H. (l) Calculated density of states (DOS) of Fe_2TiO_5 and Fe_2TiO_5-VO. (m) The band structures of both Fe_2TiO_5 and Fe_2TiO_5-VO were calculated. The contributions to the band made by iron, titanium, and oxygen are denoted by the colors blue, green, and red, respectively. (n) Fe_2TiO_5 and Fe_2TiO_5-VO free energies. The bottom left shows the NO_3^- charge density differential on Fe_2TiO_5-VO. Yellow and blue indicate charge surplus and deficiency. (o) FEs and NH_3 yield of various samples at each given potential. Reproduced from ref. 103 with permission from Wiley, copyright 2022.

was observed that among the three samples, a-RuO_2 exhibited the largest peak area for O1. This observation indicates that a-RuO_2 possesses a significantly higher number of oxygen vacancies than the other two samples (Fig. 16d). Remarkably, a-RuO_2 demonstrates exceptional performance in NO_3^- reduction, surpassing its crystalline counterparts lc-RuO_2 (FE: 55.27%, selectivity: 77.76% and YR 0.0222 mmol h^{-1} cm^{-2}) and hc-RuO_2 (FE: 7.03%, selectivity: 19.22%, YR 0.0013 mmol h^{-1} cm^{-2}) by exhibiting a high FE of 97.46%, a significant selectivity of 96.42%, and a YR of 0.1158 mmol h^{-1} cm^{-2} at −0.35 V *vs.* RHE. Through both experimental and theoretical calculations, it can be deduced that a-RuO_2's disordered atomic arrangement provides an abundance of oxygen vacancies. The remarkable selectivity and faradaic efficiency of this specially designed disordered structure can be attributed to the following factors, which have been determined through experimental and theoretical observations: 1: The disordered framework of a-RuO_2, which is rich in oxygen vacancies, is found to influence the hydrogen affinity and d-band center, thereby reducing the energy required for the potential-determining step ($NH_2^* \rightarrow NH_3^*$). 2: The vacancies also cause the d-band electrons to distribute closer to the Fermi level (PDOS), resulting in an improved adsorption of critical intermediates and a lower reaction energy for the potential-determining step (Fig. 16e). 3: Unlike c-RuO_2 (0.33 eV), a-RuO_2 needs a higher energy of 0.73 eV to generate the by-product H_2 (Fig. 16g), which means it suppresses H_2 production and enhances selectivity for a maximum product yield (Fig. 16h).

CeO_2, a significant rare earth metal oxide, displays impressive electronic and ionic conductivity. This is due to its ability to transition between the oxidation states of Ce^{3+} and Ce^{4+} flexibly. Moreover, the Ce^{3+} groups that are exposed can serve as potential active sites, effectively absorbing catalytic reaction intermediates.[176] Combining CeO_2 with OV and highly conductive carbon creates an appealing catalyst that can potentially enhance the electrocatalytic performance of NO_3 reduction. This approach inspired Li *et al.*[177] to integrate CeO_2 nanoparticles with V_O decorated N-doped carbon nanorods grown on graphite paper (CeO_{2-x}@NC/GP) to transform NO_3^- into NH_3. The identification of OVs was accomplished through XPS and EPR investigations. A noticeable peak at 530.8 eV in the oxygen spectral analysis and a significant signal at $g = 2$ in the EPR spectrum confirmed the OV formation (Fig. 16i and j). The CeO_{2-x}@NC/GP catalyst yielded a significant amount of NH_3, with a value of 712.75 μmol·h^{-1}·cm^{-2} at −0.8 V *vs.* RHE, and demonstrated an impressive FE of 92.93% at −0.5 V *vs.* RHE in a solution containing 0.1 M NaOH and 0.1 M NO_3^- (Fig. 16k and l). Theoretical calculations indicate that CeO_2(111) with oxygen vacancies (−1.47 eV) is much more susceptible to adsorbing NO_3^- than pristine CeO_2(111) (1.96 eV), leading to efficient reduction to NH_3 (Fig. 16m). During the NO_3^- adsorption process on CeO_2(111) containing V_O, one O atom takes up the V_O site, another O atom binds with the Ce atom, while the remaining O atom is exposed to the surrounding environment. Therefore, CeO_2(111) with oxygen vacancies can better adsorb and activate NO_3^- in the electrochemical conversion process.

Previous research has indicated that the morphology of nanomaterials has a significant impact on their electroactivity. The electrocatalytic performance can be significantly enhanced, in particular, by using hollow nanocatalysts because they expose more active sites and optimize atom utilization.[178,179] Wang *et al.*[46] recognized the significance of vacancies and a hollow architecture in catalysis and developed defective Cu_2O nanocubes, referred to as Cu_2O h-NCs (Fig. 17A and B), using a straightforward reduction method. The examination of O 1s spectra through XPS displayed a distinct peak at 531.2 eV, confirming the formation of OVs in the engineered material (Fig. 17D). A faradaic efficiency (FE) of 92.9% and NH_3 yield of 56.2 mg h^{-1} mg_{cat}^{-1} for NH_3 synthesis at 0.85 V (*vs.* RHE) were both signs of the exceptional performance of the resultant catalyst (Fig. 17E). According to the researchers, the high performance of the catalyst may be owing to its abundant oxygen vacancies, hollow structure, and remarkable adsorption capacity towards NO_3^- ions. Similarly, nanosheets with two dimensions (2D) are considered to have potential as electrocatalytic structures due to their effective surface efficiency, which results in more surface atoms being available as active sites.[180] However, the high aspect ratio of 2D structures creates limitations on mass transfer, which makes their NO_3RR kinetic reaction less desirable.[181,182] A multiscale defect method could be used to combat this problem and boost active sites through oxygen vacancies while enhancing mass transfer on 2D nanosheets. To improve the catalytic and mass transfer capabilities, Zhao *et al.*[183] implemented a successful electrodeposition and calcination technique (Fig. 17F) to create a multi-scale, defective Co_3O_4/Co material with an interwoven nanosheet structure. This approach introduces atomic defects, specifically OVs on Co_3O_4, which increases the number of low-coordinated sites. Moreover, the nanoscale defects, *i.e.*, nanoholes, create additional channels for easier mass transfer. Regarding the fine spectra of Co_3O_4 O 1s, the appearance of an obvious peak at 531.1 eV, along with a prominent EPR signal at 2.004 g, verifies the presence of OVs in the synthesized samples (Fig. 17G and H).[184] Comparatively, the Co_3O_4/Co-h spectrum exhibits higher intensity than the Co_3O_4/Co-l spectrum, indicating a greater concentration of OVs This higher concentration is advantageous for generating additional electrochemical sites and sequestrating more nitrates. The Co_3O_4/Co catalyst demonstrates exceptional NO_3RR properties in a neutral electrolyte thanks to its porosity, defective nanosheet architecture, and controlled oxygen vacancy. The catalyst can accommodate more nitrate on active sites, leading to an impressive ammonia yield rate of 4.43 mg h^{-1} cm^{-2} and a high faradaic efficiency of 88.7%. Theoretical calculations suggest that the oxygen vacancy enhances nitrate adsorption energy, suppresses the HER, and modifies the rate-limiting step of *NO → *HNO. The energy required for NO_3^- adsorption on Co_3O_4 with no vacancies is 0.68 eV, which is higher than that of Co_3O_4-1Ov (−1.44 eV) and Co_3O_4-2Ov (−1.81 eV) (Fig. 17I). This indicates that the presence of

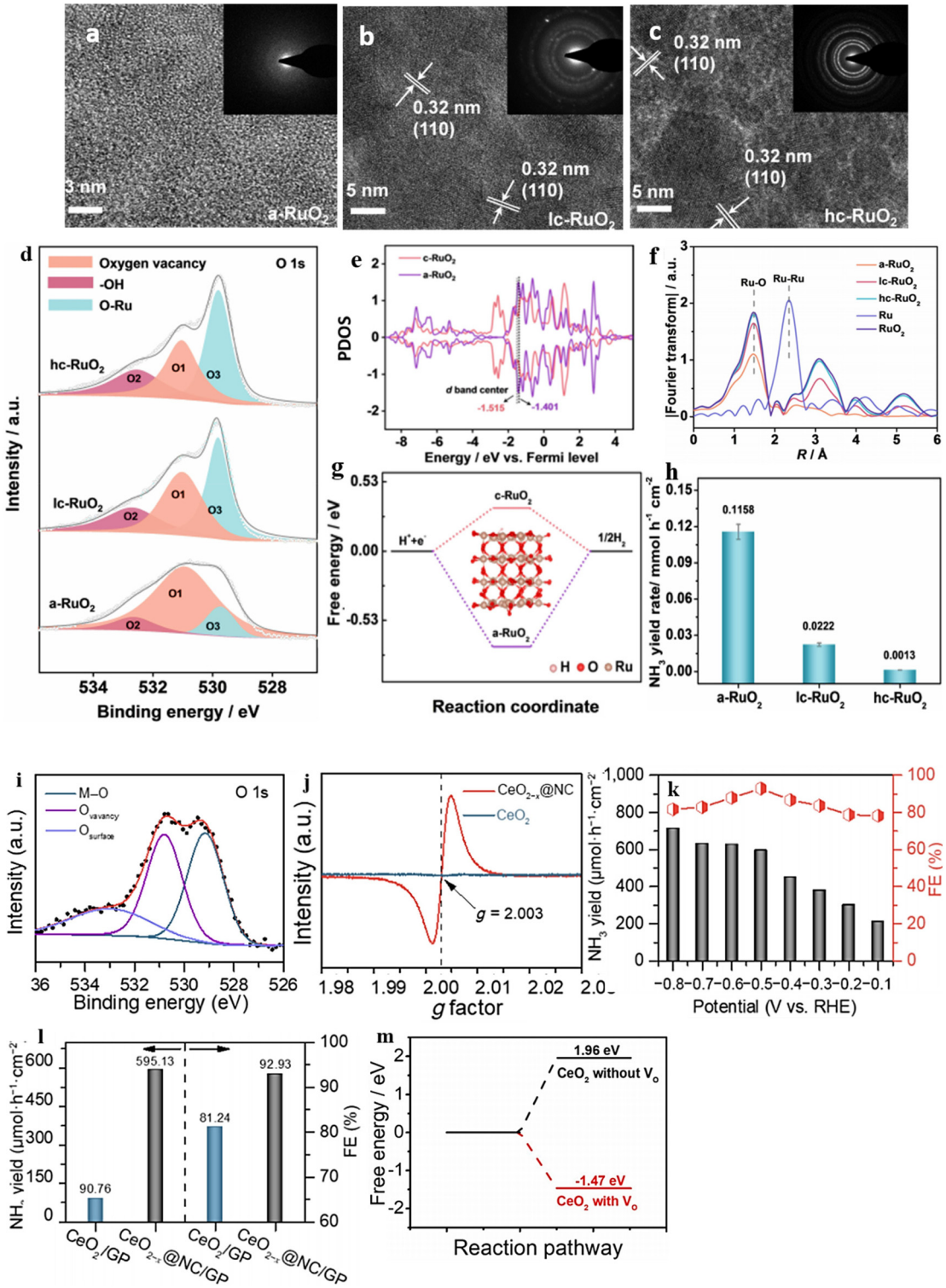

Fig. 16 HRTEM images of (a) a-RuO_2, (b) lc-RuO_2, and (c) hc-RuO_2. The insets in (a)–(c) are the corresponding SAED images. (d) O 1s XPS spectra of a-RuO_2, lc-RuO_2, and hc-RuO_2. (e) PDOS of d-bands for a-RuO_2 and c-RuO_2 and the corresponding d-band centers. (f) k^3-Weighted Fourier-transformed EXAFS spectra of Ru K-edge of the as-prepared a-RuO_2, lc-RuO_2, and hc-RuO_2. (g) The reaction energies of H_2 formation over a-RuO_2 and c-RuO_2. (h) The NH_3 yield rate on a-RuO_2 and c-RuO_2. Reproduced from ref. 163 with permission from Wiley, copyright 2023. (i) and (j) XPS spectra of O 1s and EPR spectra of CeO_{2-x}@NC and CeO_2. (k) and (l) NH_3 yield at different potentials on CeO_{2-x}@NC and the NH_3 yield of different materials. (m) Calculated free energy on CeO_2 with and without OV. Reproduced from ref. 177 with permission from Springer Nature, copyright 2022.

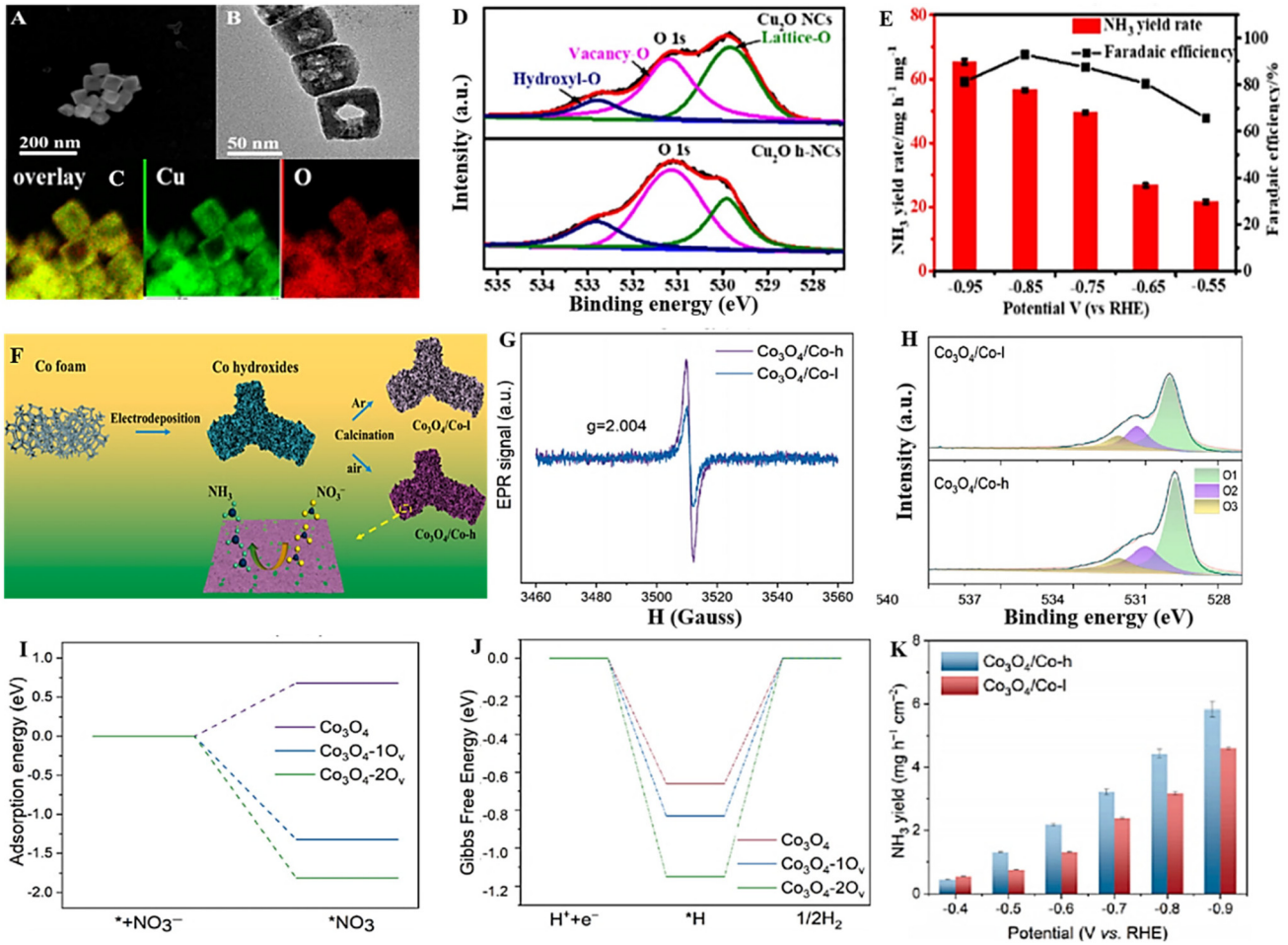

Fig. 17 (A) SEM, (B) TEM, and (C) EDX map images of Cu_2O h-NCs. (D) O 1s XPS spectra and (E) NH_3 yield and the corresponding FE of NO_3^- reduction to NH_3 on Cu_2O h-NCs. Reproduced from ref. 46 with permission from the American Chemical Society, copyright 2022. (F) A graphic photograph of the Co_3O_4 synthesis process. (G) EPR spectra, (H) XPS O 1s spectra. (I) The adsorption energy of NO_3^- on various Co_3O_4 models. (J) Gibbs free energy of H_2 generation. (K) NH_3 yield of Co_3O_4 samples at different potentials. Reproduced from ref. 183 with permission from Elsevier, copyright 2023.

sufficient oxygen vacancy defects on Co_3O_4 promotes energetically favorable NO_3 adsorption and enhances NO_3RR activity. In terms of the HER (Fig. 17J), the energy barrier required for hydrogen evolution is higher for Co_3O_4-2Ov (1.15 eV) compared with Co_3O_4-1Ov (0.83 eV) and Co_3O_4 (0.66 eV). This implies that the HER on Co_3O_4-2Ov is less feasible than the other two, and the presence of oxygen vacancies acts as an inhibiting factor for the HER. These favorable features help to clarify the reason for the high FE of the Co_3O_4-2Ov sample (Fig. 17K).

Gong *et al.* conducted a study using an Ar plasma treatment method to produce Cu_2O with oxygen vacancies. XPS measurements were employed to analyze the oxygen analysis of both untreated and plasma-treated Cu_2O samples (Fig. 18a and b). The amount of OVs increased gradually as the plasma treatment time was extended, aligning with the observations in the EPR spectra (Fig. 18c). However, a slight decrease in OV content was observed at a plasma treatment time of 60 minutes, possibly due to numerous surface oxygen species formation. The XAS analysis revealed two peaks at 934.7 and 937.4 eV in the Cu-L edge spectra, signifying the Cu(I) and Cu (II) states. The Cu(II) peak exhibited significantly higher intensity in the Ar-40 sample, indicating a greater abundance of the unoccupied density of states on the Cu sites (Fig. 18d and e). The study revealed that Cu_2O exposed to plasma treatment (40 minutes) exhibited the highest activity in the NO_3RR, yielding an NH_3 selectivity and FE of 85.7% and 89.54%, respectively, at −1.2 V *vs.* Ag/AgCl (Fig. 18f). According to the results of several DFT calculations, the polarization charge density of copper surrounding an oxygen vacancy ($10.78e^-$) is higher than the polarization charge density of copper in the initial sample ($10.46e^-$) (Fig. 18g). This increased charge density in the vicinity of the Cu sites, combined with an upshifted d-orbital, could enhance electron transfer between the surface and reaction intermediates,[185–187] resulting in a notable improvement in the NO_3RR. Likewise, Cu_2O with one oxygen

vacancy (Cu_2O with OV) on the (111) surface shows a significant reduction in the adsorption energy of NO_3^- (−2.25 eV) compared with the pristine Cu_2O surface (−0.97 eV). This trend is also observed for other reaction intermediates, which display lower adsorption energies on Cu_2O with OV than on the pristine surface. The enhanced performance of the defective Cu_2O can be attributed to the combination of an increased charge density, upshift of the d-orbital, and reduced adsorption energies of NO_3 and other reaction intermediates. Cu/TiO_2 hybrid catalyst was prepared by Zhang and their team,[106] which involved the uniform dispersion of Cu clusters on TiO_2 nanosheets with a high concentration of OVs (Fig. 18h). The XPS and EPR spectral studies in Fig. 18i and j confirmed the presence of an oxygen vacancy in the designed catalyst. According to a DFT study, the incorporation of both OVs and Cu clusters can augment the interstitial states and improve the electroconductivity, which is advantageous for enhancing the reactivity of the NO_3RR (Fig. 18k). Bader analysis demonstrated that the transfer of 1.47 and 1.39 electrons occurred from Cu clusters to TiO_2 and TiO_{2-x}, respectively. Consequently, the Cu/TiO_2 functioned as a donor–acceptor pair, thereby promoting the absorption/separation of NO_3^- and the desorption of NH_3. The hybrid catalyst 10Cu/TiO_{2-x} was able to significantly enhance the performance of ammonia synthesis, yielding a faradaic efficiency of 81.34% and a rate of NH_3 production of 0.1143 mmol h^{-1} mg^{-1} at a voltage of −0.75 V (Fig. 18l).

In a recent study, Wang and colleagues[165] introduced Fe atoms to TiO_2 nanowires, resulting in many OVs and a charge redistribution in the designed material. This, in turn, led to the formation of numerous active sites essential for nitrate reduction while simultaneously inhibiting proton reduction. Furthermore, the positively charged surface of Fe sites played a critical role in preventing proton access, suppressing hydrogen evolution, and promoting the adsorption and activation of nitrate. The electronic structure of $FeTiO_2$ was examined through DOS analyses (Fig. 19e), revealing that the O 2p state predominantly contributes to the VBM (valence band maximum). In contrast, the Ti 3d state controls the CBM (conduction band minimum). Bader charge investigation indicated that the average Bader charges for Fe-TiO_2-V_{O1}, Fe-TiO_2-V_{O2}, and Fe-TiO_2-V_{O3} were decreased to 1.85, 1.87, and 1.84, respectively, all of which were lower than that of pristine TiO_2 (1.97) (Fig. 19f). This indicates that introducing Fe atoms led to a charge redistribution in the system. Based on the Gibbs free energy pattern, it can be observed that the Fe-TiO_2-V_{O3} material was the most stable structure with induced defects for both NO_3^- adsorption and subsequent reduction among the prepared materials (Fig. 19g). In addition, Fe-TiO_2-V_{O3} demonstrated a higher energy barrier for competitive H_2 generation (1.44 eV) than pristine TiO_2 (−0.46 eV), indicating a stronger suppression of H_2 production in the Fe-doped system (Fig. 19h and i). This effect can be attributed to the positively charged surface of Fe, which repels protons more effectively. The suppression of H_2 production in Fe-TiO_2 promotes a high faradaic efficiency. As a result, Fe-doped TiO_2 demonstrated enhanced catalytic performance in the NO_3RR. Fe-TiO_2 exhibited a significantly improved electrocatalytic performance in nitrate reduction, with an ammonia yield rate of 137.3 mg h^{-1} $mg_{cat.}^{-1}$ and a faradaic efficiency of 92.3% at −1.4 V (*vs.* RHE), as compared with pristine TiO_2 (which had an ammonia yield rate of 28.8 mg h^{-1} $mg_{cat.}^{-1}$ and a faradaic efficiency of 54.7%).

$ZnCr_2O_4$ nanofiber, a zinc-rich spinel, was synthesized by Dong *et al.*[188] and used as a high-performance NO_3RR electrocatalyst for ambient NH_3 synthesis. The electrocatalytic performance was effectively boosted by substituting bivalent Zn ions for trivalent chromium, which modulated the OVs. The catalyst with the highest OVs achieved an optimal NH_3 yield rate of 20.36 mg h^{-1} $mg_{cat.}^{-1}$ and an FE of 90.21% at −1.2 V *vs.* RHE. According to theoretical calculations, $ZnCr_2O_4$ forms OVs that alter the energy levels of the d-band center (ε_d) of Cr and Zn, raising it for Cr and lowering it for Zn. These energy level shifts create primary sites for nitrate adsorption and ammonia desorption. Additionally, the insertion of Zn and V_O results in the creation of more antibonding states.[189] Moreover, the Zn-rich surface of the $ZnCr_2O_4$ catalyst facilitates the transfer of electrons from the metal active site, resulting in the efficient reduction of NO_3^- to NH_3.

Due to its cost-effectiveness and eco-friendliness, manganese oxide has demonstrated promising performance in various electrochemical reactions, including the NO_3RR.[190,191] Likewise, Cu-based materials have exhibited significant outcomes in the electrochemical reduction of NO_3^- to NH_3.[192,193] As a result, incorporating copper into MnO catalysts could be a beneficial approach for enhancing the reaction efficiency. In their research, Jang *et al.*[194] produced a range of amorphous $MnCuO_x$ catalysts with varying concentrations of oxygen vacancies using plasma treatments (Fig. 20a). OVs were detected using XPS and EPR analyses (Fig. 20d and e). The presence of a distinct peak at 531 eV in the oxygen 1s spectra and a strong signal around $g = 2$ in the EPR spectrum provided evidence for the formation of OVs. The higher intensity of the EPR spectrum for $MnCuO_x$-H indicates a larger quantity of OVs following plasma irradiation. The $MnCuO_x$ catalyst with a high concentration of OVs ($MnCuO_x$-H) exhibited a significant ammonia yield rate of 9.4 mg cm^{-2} h^{-1} and FE of 86.4%. The authors hypothesized that the OVs present in the catalyst contributed to a reduction in the binding energy of NO_3^- and a weakening of the N–O bond, leading to a superior performance. Similarly, a dual-site electrocatalyst for NO_3^- reduction was developed by Wang *et al.*[195] which was composed of MnO_2-O_v nanosheets enriched with OVs, and Pd nanoparticles that were deposited onto 3D porous nickel foam (Pd-MnO_2-O_v/Ni foam). XPS and EPR spectral studies revealed the presence of OVs. The Pd-MnO_2-O_v/Ni foam exhibits a higher concentration of OVs than the Pd/Ni foam, with percentages of 35.25% and 26.75%, respectively (Fig. 20f and g). The electrocatalyst was found to be effective in adsorbing, immobilizing, and activating NO_3^- and other intermediates through the MnO_2-O_v nanosheets, while the Pd provided sufficient adsorbed hydrogen (H*) to the oxygen vacancy sites for both NO_3^- reduction and OV regeneration, as evidenced by experi-

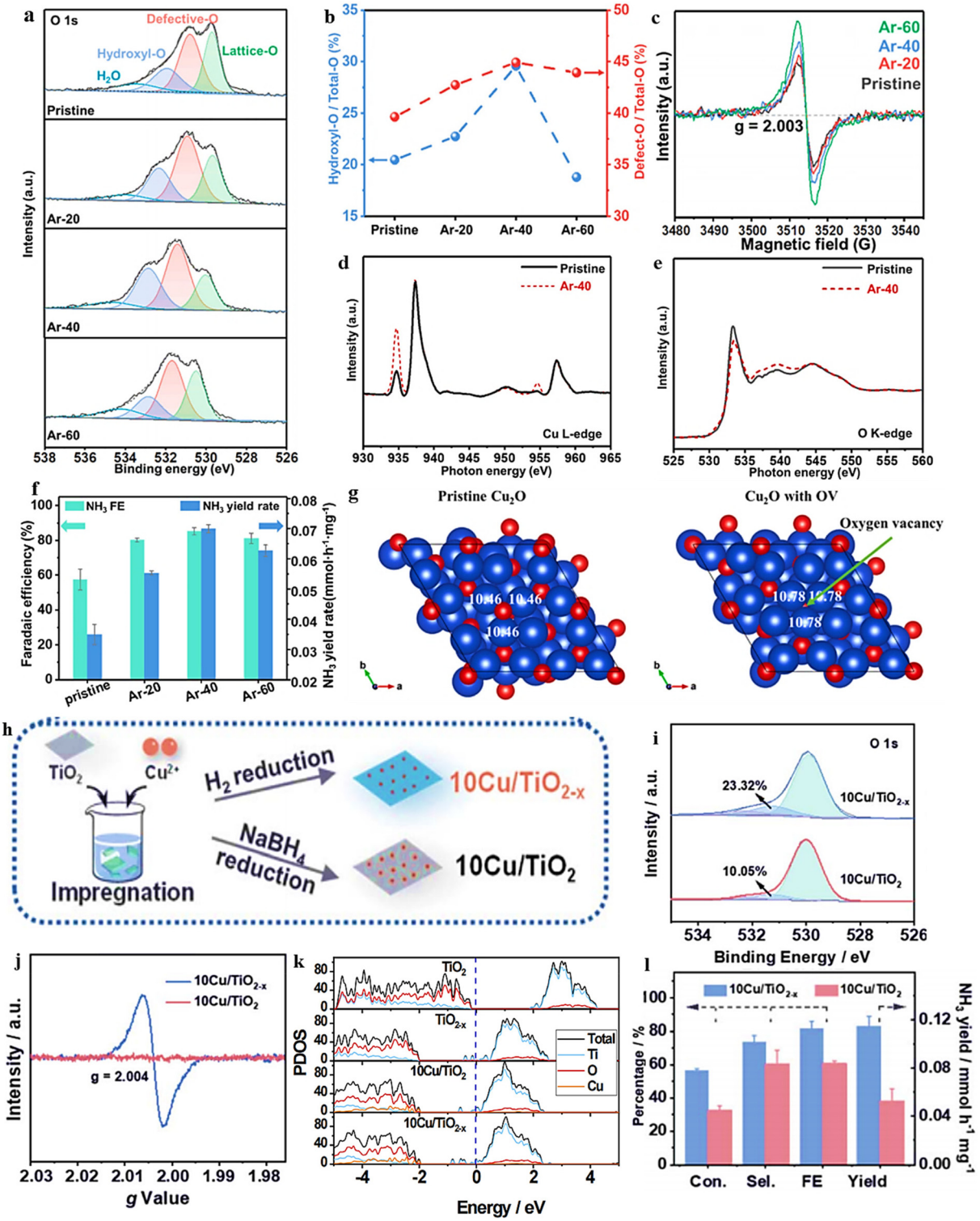

Fig. 18 (a) O 1s XPS spectra of pristine, Ar-20, Ar-40, and Ar-60. (b) The proportion of pristine, Ar-20, Ar-40, and Ar-60 areas that are occupied by O species. (c) The pure Ar-20, Ar-40, and Ar-60 EPR spectra. (d and e) X-ray absorption spectra (XAS) of pure Cu L-edge and Ar-40. (f) Ammonia production catalyzed by pristine Ar, Ar-20, Ar-40, and Ar-60 with 50 ppm N-NO_3^- at −1.2 V *vs.* Ag/AgCl for 6 hours: FE and yield rate. (g) Bader charge analysis was used to determine the polarization charge density before (left) and after (right) the creation of oxygen vacancies. Reproduced from ref. 169 with permission from Elsevier, copyright 2023. (h) Schematic presentation of the catalyst synthesis. (i and j) O 1s XPS spectra and EPR spectra of the prepared materials. (k) PDOS of the different materials and (l) $10Cu/TiO_{2-x}$ and $10Cu/TiO_2$ for NO_3^- reduction at 0.75 V: conversion rate (Con), selectivity (Sel), FE, and NH_3 production rate. Reproduce from ref. 106 with permission from Elsevier, copyright 2023.

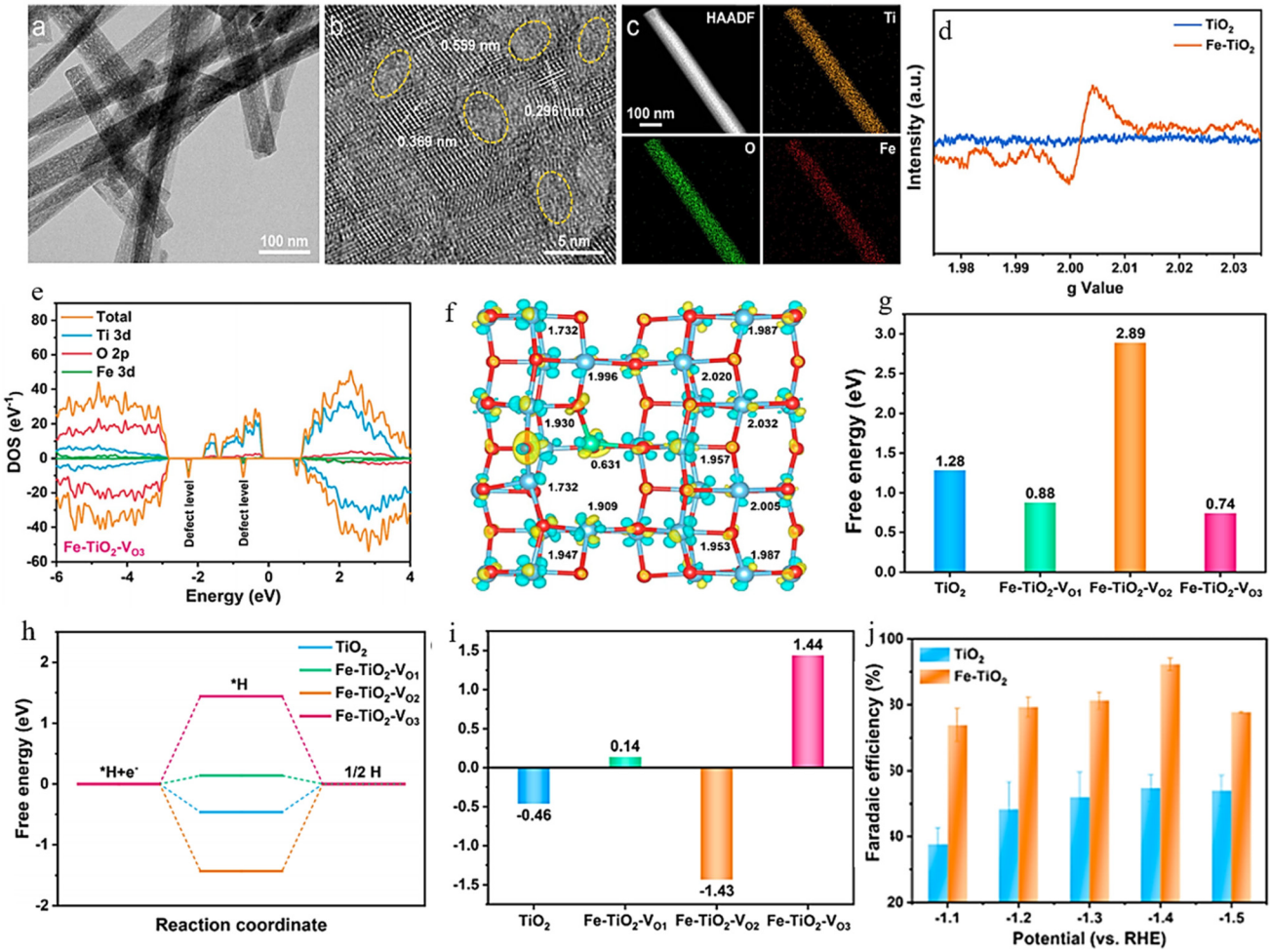

Fig. 19 Morphological and *ex situ* characterization: (a) TEM image. (b) HR-TEM observation (areas with yellow dots have morphological irregularities), (c) HAADF-STEM and EDS mapping of Fe-TiO_2 images. (d) The TiO_2 and Fe-TiO_3 spectral analysis by EPR. (e) DOS of Fe 3d, Ti 3d, and O 2p of the compound Fe-TiO_2-VO_3. (f) The Bader charge values of the surface Ti atoms in the hybrid Fe-TiO_2-VO_3. The level of the isosurface is between 0.05 and 0.05 e $Bohr^{-3}$. (g) The RDS of the NO_3RR over pure TiO_2 and Fe-doped TiO_2 is expressed in terms of Gibbs free energies. (h) Hydrogen evolution process over pure TiO_2 and Fe-doped TiO_2 – free energy diagrams. (i) The Gibbs free energies for the RDS of the HER over pristine TiO_2 and Fe-doped TiO_2 samples. (j) Efficiency of ammonia formation by faradaic reactions on TiO_2 and Fe-TiO_2 at various potentials. Reproduced from ref. 165 with permission from the American Chemical Society, copyright 2023.

mental characterizations and theoretical calculations (Fig. 20h). Palladium (Pd) has also been documented to synergistically trigger the activation of NO_3^- and disrupt *NO on the Bi1Pd catalyst. This results in a lowered energy barrier for the potential-determining step (NO → NOH) and improved protonation dynamics along the NO_3^--to-NH_3 pathway.[196] In another study, Wang and colleagues[197] were able to successfully create a new type of material, namely Cu/Cu-Mn_3O_4 NSAs/CF (Fig. 20i), which contained a significant number of interfaces between Cu and Cu-Mn_3O_4, as well as a high concentration of OVs. This material exhibited exceptional electrocatalytic activity in converting nitrate to ammonia, obtaining remarkable results in terms of NO_3^- conversion (95.8%), NH_3 selectivity (87.6%), NH_3 production rate (0.21 mmol h^{-1} cm^{-2}), and FE (92.4%) when an applied potential of −1.3 V (*vs.* SCE) was applied. XPS and EPR investigations revealed a higher abundance of oxygen vacancies in Cu/Cu-Mn_3O_4 compared with the Mn_3O_4 NSs sample (Fig. 20l and m). The superior electrocatalytic performance of the material was attributed to the combined effects of the numerous Cu/Cu-Mn_3O_4 interfaces and the abundance of OVs, which together assisted in the modification of the surface electrical structure, allowing for the adsorption and activation of NO_3^- (Fig. 20o).

Meng and colleagues[198] utilized a novel method to generate ammonia using a Co_2O_3 catalyst that contained multiple OVs. The catalyst was synthesized using a precipitation technique (Fig. 21a), and the OVs were identified through XPS analysis (as shown in Fig. 21b and c). The NH_3 synthesis was accomplished by combining non-thermal plasma oxidation and electroreduction (Fig. 21d). To initiate plasma activation of air in the first step, a Ti bubbler was introduced, resulting in the effective production of nitrate/nitrite (NO_x^-) in an absorption

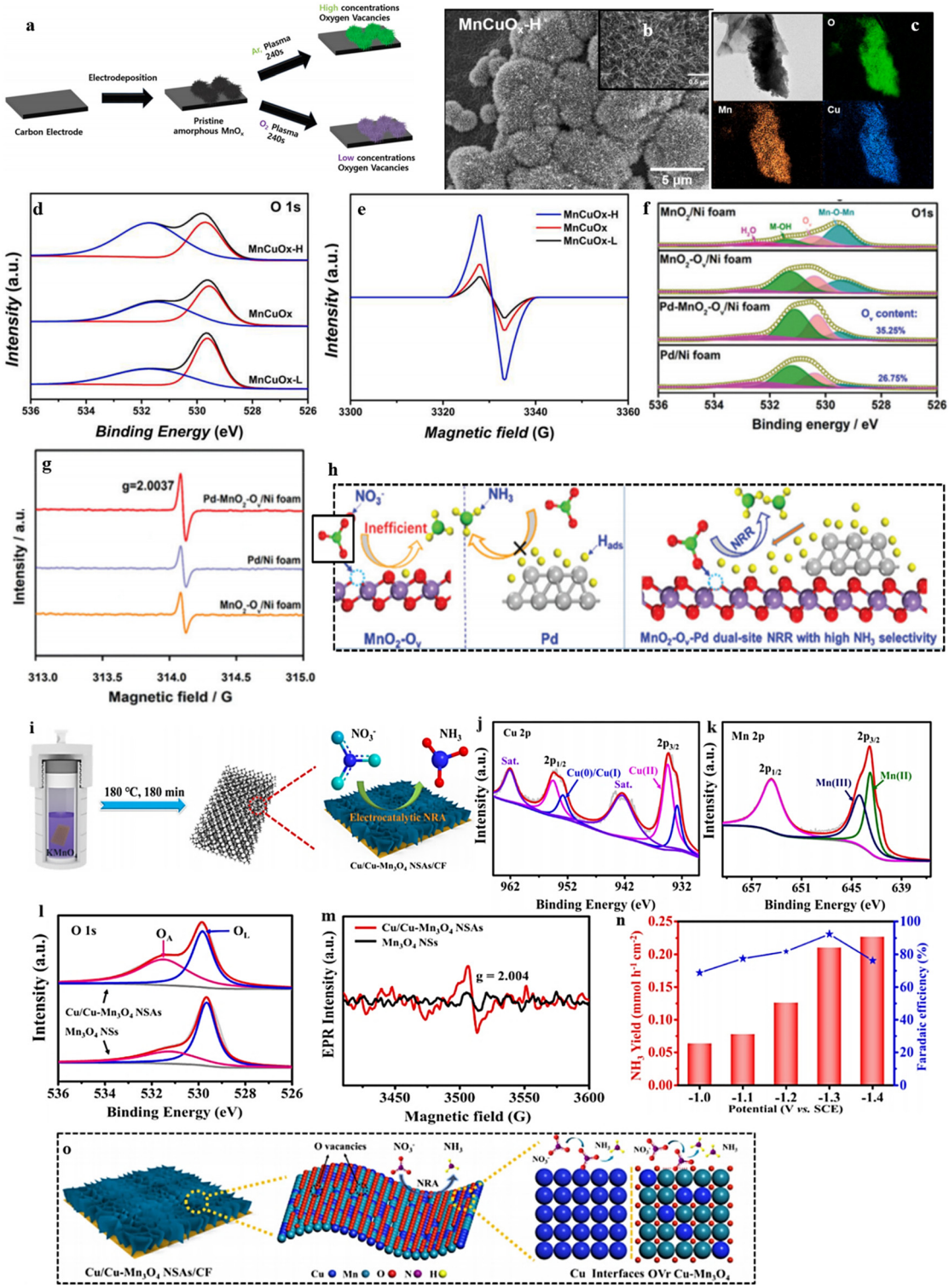

Fig. 20 (a) Illustration in the form of a schematic showing the complete synthesis process for $MnCuO_x$ catalysts. (b) SEM morphology of $MnCuO_x$-H. (c) The elemental distribution of oxygen, manganese, copper, and their overlay in a selected area of $MnCuO_x$-H, as shown by EDX. (d and e) The XPS spectra of O 1s and the EPR spectra of the $MnCuO_x$ catalysts. Reproduced from ref. 194 with permission from Elsevier, copyright 2023. (f and g) XPS analysis of O 1s of a $PdMnO_2$ sample and (h) a schematic of the high-NH_3 selectivity MnO_2-Ov-Pd dual-site NRR mechanism. Reproduced with permission.[195] (i) Electrocatalytic NO_3^- reduction by Cu/Cu-Mn_3O_4 NSAs/CF: a preparation and illustration scheme. (j–l) XPS spectra of distinct Cu 2p, Mn 2p, and O 1s orbitals in various Cu/Cu-Mn_3O_4 samples. (m) EPR of Cu/Cu-Mn_3O_4 samples. (n) Production of NH_3 and FE at different potentials. (o) A schematic representation of the electrocatalytic reduction of NO_3^- to NH_3 conversion on Cu/Cu-Mn_3O_4 NSAs/CF. Reproduced from ref. 197 with permission from American Chemical Society, copyright 2021.

solution, with a production rate reaching a maximum of 55.29 mmol h^{-1} (Fig. 21e). The NO_x^- in aqueous solution was employed directly as the catholyte for the second electroreduction process, using oxygen vacancy-rich Co_3O_4 nanoparticles as the catalyst. By utilizing DFT calculations, it was discovered that including OVs in Co_3O_4 nanoparticles enhances the activity of adjacent Co atoms. This, in turn, leads to an increase in the adsorption and hydrogenation of NO_x^- by reducing the ΔG of the rate-limiting step while simultaneously impeding the hydrogen evolution reaction (Fig. 21g and h). Consequently, these oxygen vacancy-rich Co_3O_4 nanoparticles exhibit an outstanding NH_3 production rate of 39.60 mg h^{-1} cm^{-2}, a high faradaic efficiency of 96.08% (at −0.8 V), and a large current density of 376.48 mA cm^{-2} (Fig. 21i). This study demonstrates the possibility of generating NH_3 from air sustainably for industrial purposes and inspires further innovation in the entire NH_3 production system. This includes the exploration of alternative reaction routes, the development of improved devices, and the discovery of novel catalysts. Similarly, metal doping and oxygen vacancies in transition metal oxides are believed to be effective in achieving high activity and NH_3 selectivity in the NO_3RR. To this end, Sam and colleagues[199] synthesized Cu-doped Co_3O_4 with abundant oxygen vacancies (Cu-Co_3O_{4-x}) on carbon cloth (Fig. 21j). The O 1s spectra of Cu-Co_3O_{4-x} were analyzed using XPS, and the results showed three peaks at 530.8, 531.9, and 533.5 eV (Fig. 21m). These peaks corresponded to lattice oxygen (O1), oxygen vacancy (O2), and surface-adsorbed oxygen species (O3), respectively.[200] The Cu-Co_3O_{4-x} sample contained 25.9% OVs, which was considerably higher than the oxygen vacancy content of Co_3O_4 (17.2%), demonstrating that the increased concentration of oxygen vacancies was successfully achieved in Cu-Co_3O_{4-x}.

Similarly, Cu-Co_3O_{4-x} displays a more intense EPR signal than Co_3O_4, suggesting a higher concentration of oxygen vacancies in Cu-Co_3O_{4-x} (Fig. 21n). These findings provide conclusive evidence that Cu-Co_3O_{4-x} nanoarrays were effectively synthesized. The Cu-Co_3O_{4-x} produced in this study exhibited an excellent performance in selectively reducing nitrate to NH_3, achieving high faradaic efficiencies of approximately 90% and a substantial NH_3 yield of 0.83 mmol h^{-1} cm^{-2} in the neutral electrolyte (Fig. 21o). The authors attributed the greatly improved NO_3RR activity and selectivity towards NH_3 to both the Cu doping and the presence of abundant oxygen vacancies in the $CuCo_3O_{4-x}$. Moreover, the Cu-Co_3O_{4-x} sample with the greater active surface area among the Cu-Co_3O_{4-x} samples exposed more catalytically active sites, further contributing to its high NO_3RR activity.

5.1 Perovskite-based electrocatalysts

Owing to its exceptional catalytic activity, flexible structure, and composition, perovskite oxides have recently been recognized as a potential candidate for a new kind of catalyst material. Perovskite oxides, in contrast to other types of metal oxide, promote their metal cations in non-standard or mixed valence states, which results in an abundance of oxygen vacancies in the structures of the catalysts. Perovskite oxides possess a unique characteristic, unlike other metal oxides, where the concentration of oxygen vacancies can be effectively controlled.[54] Doping at B-sites in ABO_3-typed perovskites has been demonstrated to enhance the electrocatalytic performance by increasing the presence of oxygen vacancies. Typically, the oxygen anions coordinated with B-sites exhibit higher reactivity for electrochemical reactions, as evidenced by prior studies.[63,201] This potential inspired Zheng *et al.*[84] to investigate the performance of perovskite oxides in electrochemical nitrate reduction reactions. The researchers prepared four different ABO_3-type perovskite oxides (A = La; B = Cr, Mn, Fe, Co) with distinct crystal structures. Among the four perovskites ($LaCoO_3$, $LaMnO_3$, $LaCrO_3$, $LaFeO_3$), the O 1s XPS spectra revealed a prominent OV band at 531.3 eV,[202] with $LaCoO_3$ exhibiting the highest percentage at 47.1% (Fig. 22a and b). Furthermore, the investigation of OVs was also conducted using the EPR technique, revealing that $LaCoO_3$ exhibited a robust EPR signal, suggesting the highest percentage of oxygen vacancies compared with the other perovskites (Fig. 22c). Using density functional theory (DFT) analysis, it was discovered that incorporating OVs into the $LaCoO_3$ perovskite enhances the adsorption of $*NO_2$ intermediates and significantly lowers the energy barrier required for nitrate reduction to ammonia catalysis. This results in improved activity and selectivity. In comparison with $LaCrO_3$ (21.7%, 0.44 mmol mg^{-1} h^{-1}), $LaMnO_3$ (49.1%, 0.88 mmol mg^{-1} h^{-1}), and $LaFeO_3$ (78.4%, 3.54 mmol mg^{-1} h^{-1}), the $LaCoO_3$ electrode has a higher faradaic efficiency of 91.5% and a greater NH_3 yield rate of 4.18 mmol mg^{-1} h^{-1} at −1.0 V (*vs.* RHE) (Fig. 22d and e).

Although perovskite oxides based on cobalt have shown a significant amount of potential in electrocatalysis,[203,204] their ability to accelerate NO_3^- electrochemical reduction to generate NH_3 has not been explored. Liu *et al.*[205] have addressed this by proposing an effective strategy to promote NO_3ER activity by adjusting the A-site deficiencies of cobalt-based perovskite oxides. To demonstrate this, they used a series of $(Ba_{0.5}Sr_{0.5})_{1-x}Co_{0.8}Fe_{0.2}O_{3-d}$ (x = 0, 0.05, 0.10, 0.15, and 0.20) catalysts as a proof-of-concept, finding that their NO_3ER activity followed a volcano-like dependence on the x values, peaking at x = 0.15. With the increasing A-site cation deficiencies, the XRD data presented in Fig. 22g revealed a slight shift towards higher angles for the main peak associated with the (110) plane. The presence of OVs in the $(BS)_{1-x}CF$ samples was determined using XPS analysis. Fig. 22h and i display the O 1s XPS spectra, which show a distinct peak at 530.9 eV alongside three other peaks, indicating the presence of surface-generated OVs.[206] The percentage of OVs in BSCF, (BS)0.95CF, (BS)0.90CF, (BS)0.85CF, and (BS)0.80CF was approximately 38.0%, 39.9%, 49.6%, 53.4%, and 55.1%, respectively. These findings demonstrate a direct correlation between the amount of A-site cation deficiencies and the quantity of OVs. As anticipated, the introduction of A-site deficiencies resulted in significant changes to the physicochemical properties of the cobalt-based perovskite oxides. Specifically, the A-site deficiencies led to the creation of

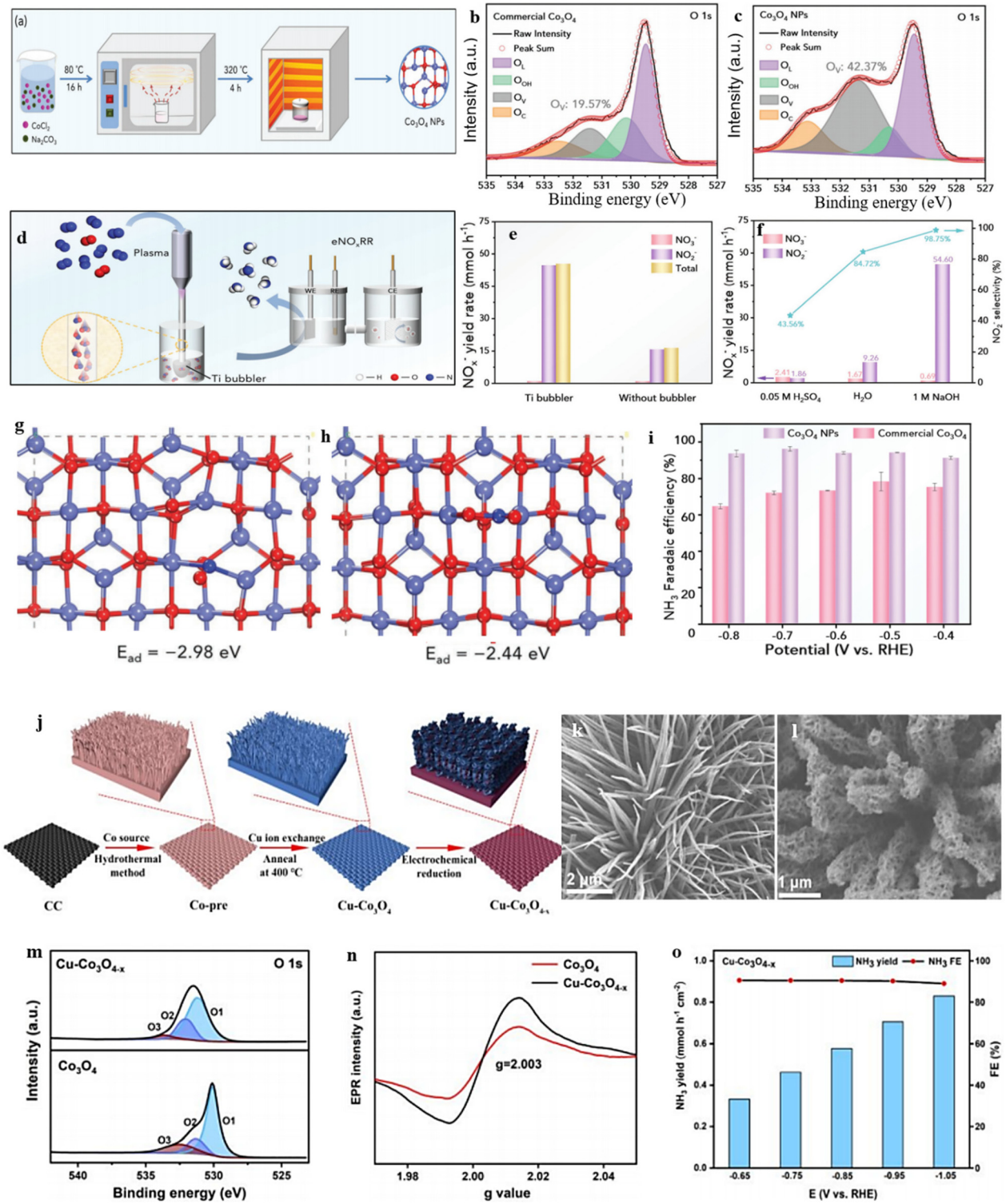

Fig. 21 (a) Schematic illustration of the preparation of Co_3O_4 NPs. (b) and (c) XPS spectra of Co O 1s for commercial Co_3O_4 and Co_3O_4 NPs respectively. (d) Complete system of N_2 fixation to NH_3. (e) NO_x^- yield rate with and without a Ti bubbler in NaOH (1 M) absorption solution after 10 min plasma activation. (f) NO_x^- yield rate and NO_2 selectivity absorbed by different solutions after 10 min plasma activation with a Ti bubbler. (g) and (h) Adsorption configurations and corresponding E_{ad} of NO_2^- on (g) OV-Co_3O_4 and (h) Co_3O_4. (i) NH_3 FEs. Reproduced from ref. 198 with permission from Wiley, copyright 2023. (j) Schematic illustration of the synthesis process for Cu-Co_3O_{4-x} on carbon cloth. (k) and (l) SEM images of Cu-Co_3O_4, and Cu-Co_3O_{4-x} respectively. (m) and (n) XPS spectra of O 1s and EPR spectra of Co_3O_4 and Cu-Co_3O_{4-x}. (o) NH_3 yield rate and FE of Cu-Co_3O_{4-x}. Reproduced from ref. 199 with permission from RSC, copyright 2023.

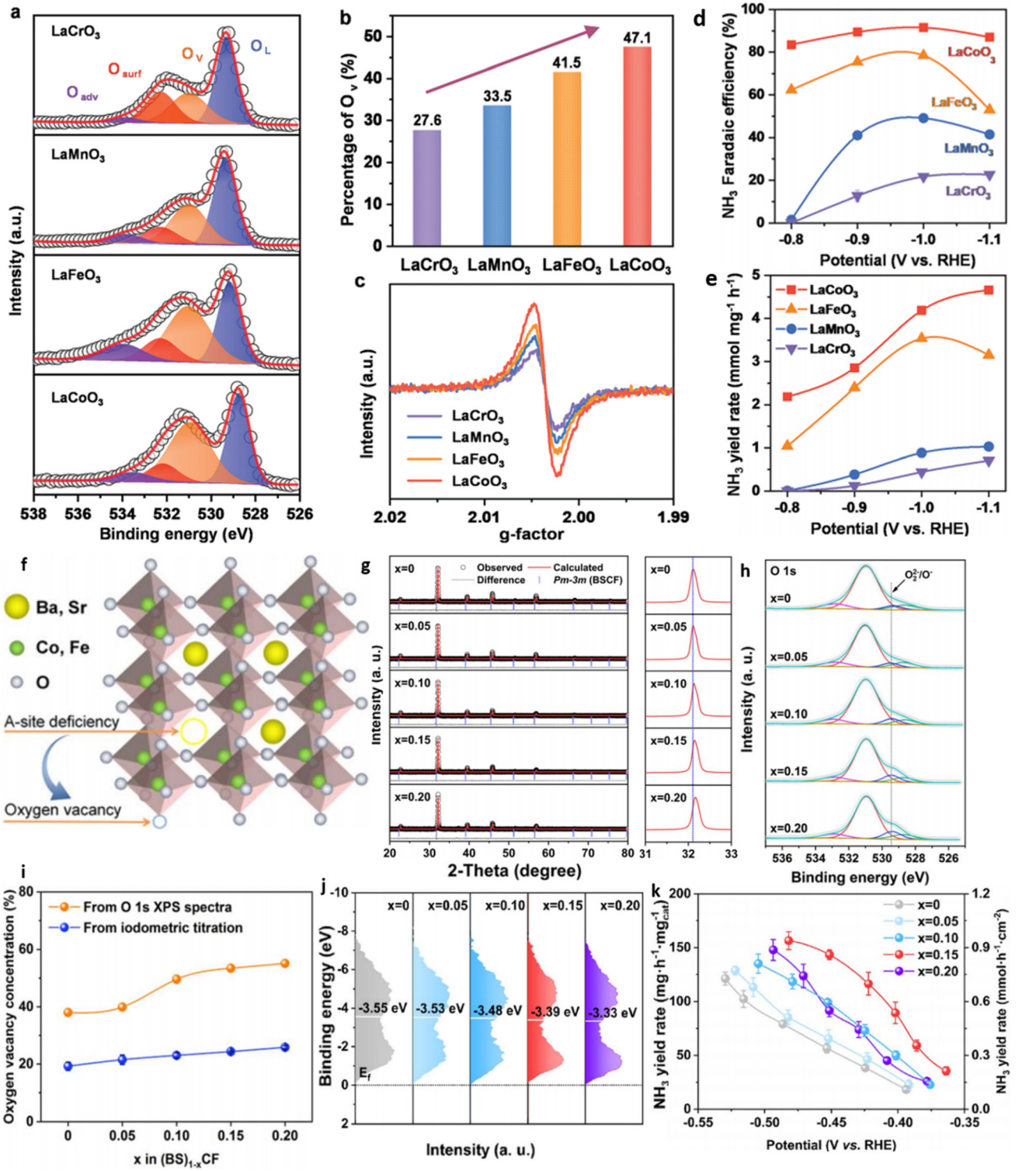

Fig. 22 (a) $LaCrO_3$, $LaMnO_3$, $LaFeO_3$, and $LaCoO_3$ O 1s spectra with high resolution by XPS analysis. (b) The percentage of oxygen vacancies for $LaCrO_3$, $LaMnO_3$, $LaFeO_3$, and $LaCoO_3$ from XPS analysis. (c) EPR spectra of $LaCrO_3$, $LaMnO_3$, $LaFeO_3$, and $LaCoO_3$. (d) NH_3 FE at different potentials, and (e) NH_3 yield rate at different potentials. With permission. (f) An illustration in the form of a schematic showing the formation of oxygen vacancies in A-site-deficient $(BS)_{1x}CF$. (g) Rietveld refinement plots of $(BS)_{1-x}$ CF sample XRD data with enlargements in the 2-theta region of 31–33°. (h) O 1s XPS spectra of the samples made from $(BS)_{1-x}CF$. (i). oxygen vacancy concentration. (j) XPS spectra of the surface valence bands, with the d band center determined. (k) The rate of NH_3 production by the $(BS)_{1x}CF$ samples at a variety of potentials. Reproduced from ref. 205 with permission from RSC, copyright 2023.

varying amounts of oxygen vacancies that increased with higher x values. Additionally, as x increased, the band center gradually shifted closer to the Fermi level (Fig. 22j). The results of this research pave the way for a hopeful approach toward the rational development of innovative cobalt-based perovskite oxides for facilitating NO_3ER catalysis. Among them, the (BS)0.85CF catalyst exhibited the highest activity (143.3 mg h^{-1} mg_{cat}^{-1} or 0.86 mmol h^{-1} cm^{-2}) and selectivity (97.9%) for ammonia at −0.45 V (*vs.* RHE), and maintained excellent stability for up to 200 hours, surpassing most previously reported NO_3ER catalysts (Fig. 22k).

The manipulation of the electronic structure, material properties, and catalytic efficiency has been attributed to the recognition of factors such as the 2D architecture, structural defects, and the interface effect.[207–211] Taking inspiration from the aforementioned material characteristics, Wang *et al.*[212] employed the chemical oxidation of Cu foam to produce an in-plane heterostructured nanosheet structure, Cu/CuO_x/CF, characterized by a high abundance of OVs (Fig. 23a, d, and e). The authors suggested that the arrays of 2D nanosheets could offer a plentiful number of active sites and greatly improve the process of mass/charge transfer during electrocatalysis. Furthermore, the presence of in-plane heterojunctions and the high concentration of OVs worked synergistically to enhance the electronic properties of the catalytic sites. As a result, it became possible to control the adsorption properties of reactant intermediates and minimize the generation of undesired byproducts. The excellent physicochemical characteristics of Cu/CuO_x/CF result in its outstanding catalytic performance for electrocatalytic NO_3^--to-NH_3 conversion. Notably, the NH_3 yield rate on Cu/CuO_x/CF can achieve 0.23 mmol h^{-1} cm^{-2} at −1.3 V (*vs.* SCE), with an excellent NO_3^- conversion efficiency (99.52%), NH_3 selectivity (95.00%), and NH_3 faradaic efficiency (FE, 93.58%) (Fig. 23g, h, and i).

Tungsten (W) catalysts having OVs are extensively utilized to enhance selective NH_3 synthesis. For instance, WO_{3-x} nanosheets and WO_{3-x} nanowires with OVs can influence the adsorption of N species and mitigate the competing HER to some degree.[213] Consequently, it is expected that OVs in W-based catalysts can efficiently capture and reduce N species. Nevertheless, there is a scarcity of research focusing on tungsten-based perovskite oxide (nanosheets) with OVs for nitrate reduction to ammonia. A comprehensive investigation was conducted by Feng *et al.*[214] regarding the synthesis (Fig. 24a) and electroreduction of nitrate to ammonia using $NbWO_6$ nanosheets with oxygen vacancies ($NbWO_{6-x}$). The presence of oxygen vacancies was confirmed through XPS and EPR techniques, as illustrated in Fig. 24b and d. The analysis of the density of states (DOS) for $NbWO_6$ reveals that oxygen (O), niobium (Nb), and tungsten (W) make the most significant contributions to both the valence band and conduction band. Additionally, the DOS analysis demonstrates the presence of distinct defect energy levels in the conduction band of $NbWO_{6-x}$, indicating enhanced electron transitions (Fig. 24e). The introduction of oxygen vacancies on the surface results in the Fermi level shifting towards the CBM (conduction band minimum) due to the acquisition of excess 4d electrons from tungsten (W). Consequently, this imparts metallic behavior to the $NbWO_{6-x}$, leading to improved conductivity, which is advantageous for electrochemical reduction. Moreover, the adsorption energy of NO_3^- on $NbWO_{6-x}$ (−1.27 eV) is significantly lower compared with $NbWO_6$ (−0.53 eV), making it more favorable for NO_3^- adsorption (Fig. 24f). This enhanced adsorption capability facilitates nitrate reduction to NH_3.

Nb-based materials have garnered considerable attention in heterogeneous catalysis due to their promising properties. Among them, NbO_2 is highly regarded for its semiconductor properties, exhibiting high capacitance and exceptional electrical conductivity.[215] Moreover, Nb_2O_5 has been identified as an effective catalyst for favorable ammonia synthesis, even under challenging conditions.[216] Consequently, Nb oxides hold great potential as electrocatalysts for nitrate to NH_3 conversion, as the d-orbitals (partially occupied) of Nb^{4+} facilitate π back bonding with reactants. Taking inspiration from these advantageous properties, Wan *et al.*[217] have recently presented pioneering research introducing an NbO_x catalyst containing OVs for nitrate reduction to produce NH_3. The XPS spectra of Nb_2O_5 exhibit a single peak at 530.5 eV, whereas NbO_x displays an additional peak at 531.8 eV, suggesting the presence of OVs in the NbO_x sample (Fig. 24h).[57] Furthermore, the investigation conducted by Pl demonstrated that the NbO_x sample contains a higher concentration of OVs compared with the Nb_2O_5 counterpart (Fig. 24i). The OV-rich material demonstrated an impressive faradaic efficiency (FE) of 94.5% and achieved an NH_3 formation rate of 55.0 μg h^{-1} mg_{cat}^{-1} (Fig. 24j and k). A detail investigation revealed that the presence of OVs significantly influenced the chemical state of Nb, resulting in an enhancement of the binding energy of crucial intermediates during electrolysis.

Crystal facet engineering has been widely acknowledged as a means to adjust material properties and electrocatalytic efficiency. The use of catalysts with controllable crystal facets provides an excellent opportunity to investigate how catalyst properties influence surface reaction kinetics.[218,219] In their study, Zhong *et al.*[220] synthesized Cu_2O samples with various facets, including (100), (111), and a combination of (100) and (111) (Fig. 25a–c). These samples were prepared with different levels of oxygen vacancies and OH groups as observed from XPS investigations (Fig. 25d). Notably, Cu_2O with (111) facets demonstrated the highest presence of oxygen vacancies and hydroxyl groups on its surface. Based on their findings, the researchers concluded that on the Cu_2O(111) surface, the presence of OVs improves the adsorption kinetics of reactants and other intermediates. At the same time, hydroxyl groups play a crucial role in inhibiting the unwanted hydrogen evolution side reaction and facilitating the reduction process of NO_3^- (Fig. 25g). The combined impact of these two factors is responsible for the exceptional NO_3^- reduction activity observed in the Cu_2O(111) facet when compared with other facets (Fig. 25j).

Although the role of OV and ion clusters has been studied in electrochemical catalysis, the synergistic interaction between these two species has received limited attention.

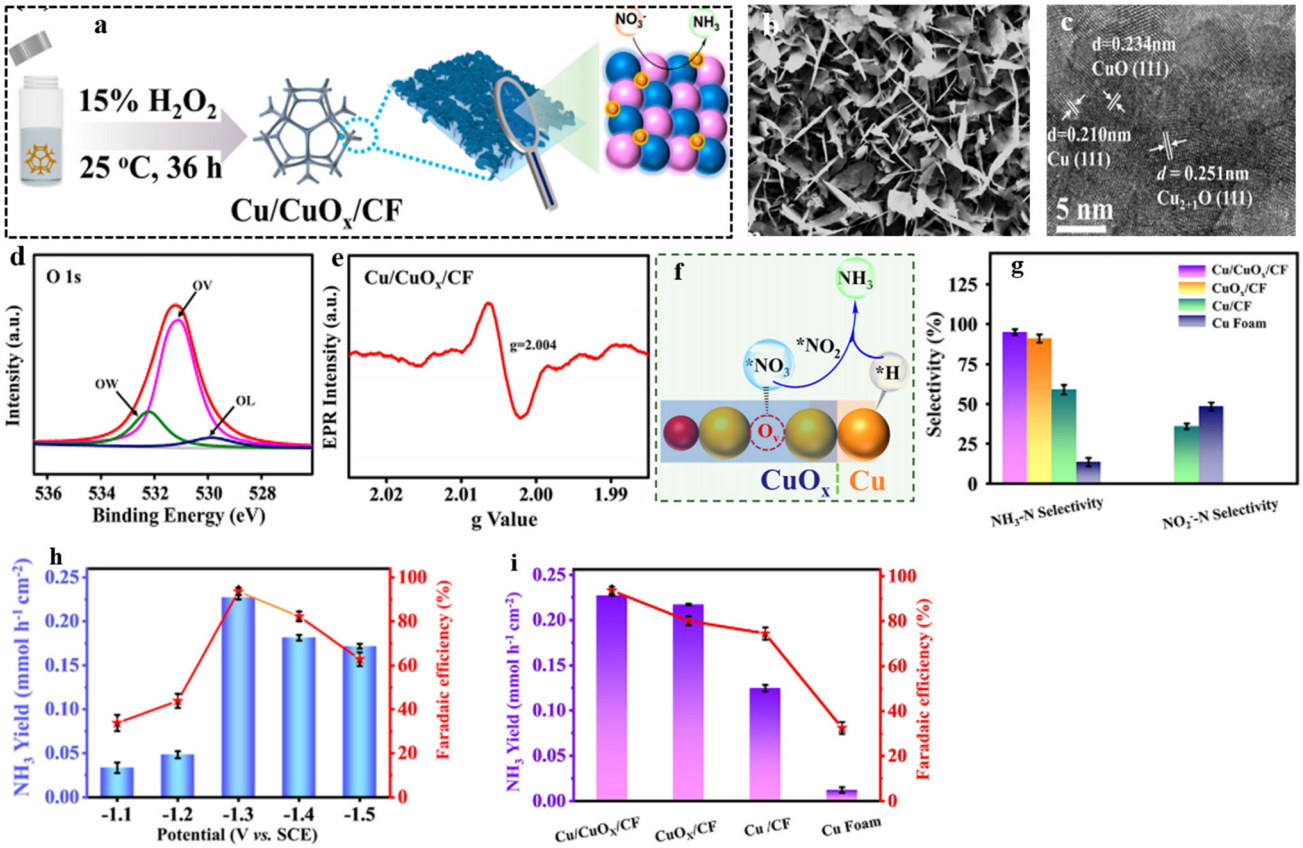

Fig. 23 (a) A schematic depicting the production of Cu/CuO_x/CF as well as its subsequent electroreduction using NO_3^-. (b and c) Images of Cu/CuO_x/CF were obtained using SEM and HRTEM. XPS spectra of O 1s as item (d). (e) EPR spectra. (f) A schematic representation of the electrochemical reaction that converts NO_3^- to NH_3, which is catalyzed by the Cu/CuO_x/CF system. Selectivity of the NH_3-N and NO_2-N, yield rate, and the FE of NH_3 for various samples (g–i). Adopted with permission.[212] With permission from the American Chemical Society, copyright 2022.

Chen *et al.*[221] developed a Cu-based electrocatalyst called Cu-Ov-W, which incorporates neighboring Mo clusters (Fig. 26a). The goal was to introduce asymmetric Ov properties to fine-tune the local electronic environment surrounding the active sites of the catalyst. The formation of OVs in CuW is supported by both XPS and EPR analyses (Fig. 26b and c). Notably, the hollow CuW (H-CuW) exhibits a higher intensity of OV compared with other counterparts, as confirmed by these investigations. The combined effect of the asymmetric Cu-Ov-W and the enhanced protonation process resulting from the Mo clusters contributes to a significant performance boost in the overall process. Consequently, this leads to a high Faradaic efficiency and yield rate of NH_3, achieving 94.60% and 5.84 mg h^{-1} mg_{cat}^{-1}, respectively, at 0.7 V *vs.* RHE. According to DFT calculations, an elevated concentration of oxygen vacancies leads to a notable shift of the d-band center in CuW towards the Fermi energy (H-CuW, −3.36 eV and L-CuW, −3.79 eV) (Fig. 26d and e). The d-band centers are indicating that as the concentration of OVs increases, the d-band center moves closer to the Fermi energy. These upshifts in the d-band center highlight the essential role of the Cu-Ov-W sites in adjusting the local environment to favor the adsorption of NO_3^-. Additionally, this adjustment weakens and activates the N═O bond, thereby influencing the overall catalytic process.

5.2 Reaction mechanism from NO_3^- to NH_3

The electrochemical synthesis of NH_3 from NO_3^- proceeds through an eight-electron transfer reaction, with the oxidation states of the reactant changing from +5 in (NO_3^-) to −3 in the product (NH_3).[222] The specific reaction pathway depends on various factors such as the catalyst composition, the current density, and the electrolyte environment.[223–228] Several possible pathways for the electrochemical reduction of NO_3^- have been identified. One pathway involves the direct electroreduction of NO_3^- as shown in (Fig. 27a).[229,230] This pathway has been observed on Pt- and Sn-based electrocatalysts, where the hydrogenation of adsorbed NO (NO_{ads}) occurs, leading to the formation of hydrogenated products such as HNO, H_2NO, H_2NOH, and finally NH_3 (Fig. 27c).[229,230] Another pathway involves an H-assisted mechanism, where H_2O molecules are first reduced to generate adsorbed H (H_{ads}) (Fig. 27b).[20] The synchronized adsorption of H_{ads} and NO_{ads} leads to their hydrogenation and the formation of various hydrogenated

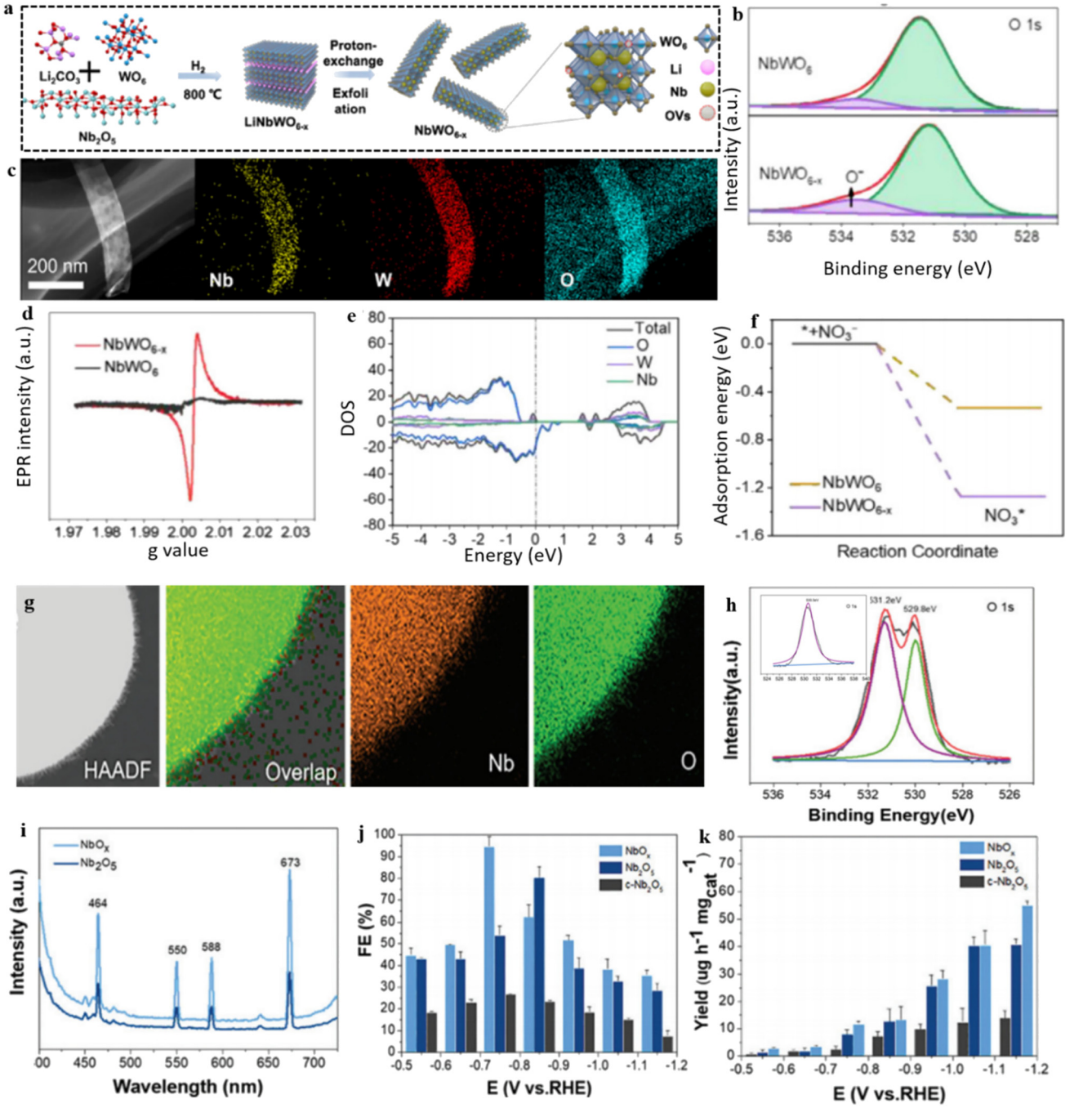

Fig. 24 (a) Schematic illustration of the $NbWO_{6-x}$ nanosheet synthesis. (b) O 1s XPS spectra. (c) The HAADF-STEM picture of the $NbWO_{6-x}$ nanosheets and their elemental mapping of Nb, W, and O. (d) EPR spectra, (e) The DOS diagram of $NbWO_{6-x}$ and (f) calculated adsorption energies of NO_3^- on $NbWO_6$ and $NbWO_{6-x}$. Reproduced from ref. 214 with permission from Elsevier, copyright 2023. (g) EDX elemental mapping images of Nb and O for NbO_x. (h) O 1s XPS spectra of NbO_x and Nb_2O_5 (inset). (i) PL spectra of NbO_x and Nb_2O_5. (j and k) Faradaic efficiency and NH_3 yield rates at different potentials. Reproduced from ref. 217 with permission from RSC, copyright 2022.

intermediates, ultimately resulting in NH_3 production (Fig. 27d).[228,231,232] Ru-clusters have also been to support this mechanism by producing a reductive environment that facilitates the hydrogenation of NO_3^-.[20] The specific reaction conditions such as pH, concentration, and applied potential can influence the *in situ* reaction mechanism of electrochemical reduction of NO_3^-. For instance, under acidic conditions, NH_3 production increases while NO_2^- decreases. In alkaline conditions, the main product is observed as NH_2OH, but NO_2^- also appeared as well, indicating that the pathway can be pH-dependent.[231] Further studies, such as FTIR, have been conducted to investigate the detailed mechanism of NO_3^- reduction in the Cu(100) and Cu(111) facets in the presence of alkaline and acidic conditions. Likewise, the recent DFT

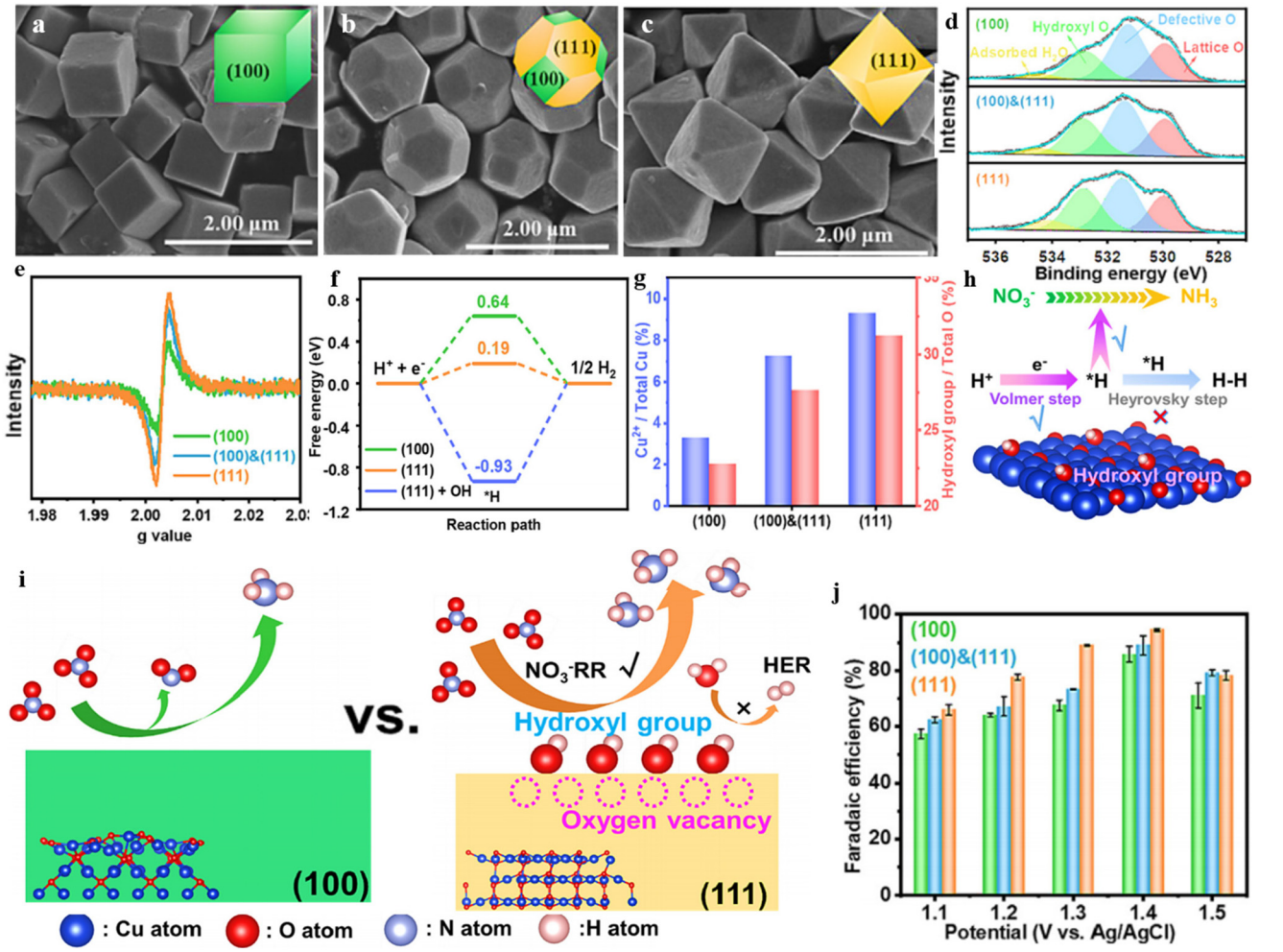

Fig. 25 (a–c) SEM morphologies (inset) of the exposed facet. (d) O 1s XPS. (e) EPR spectra. (f) A schematic illustrating the free energy of the HER as estimated by the DFT computation. (g) The percentage of Cu^{2+}, which is shown on the left side of the *y*-axis, and the hydroxyl group, which is shown on the right side of the *y*-axis, on the surface of $Cu_2O(100)$, $Cu_2O(100)$ and (111), and $Cu_2O(111)$. (h) A schematic illustrating how the presence of hydroxyl groups on the (111) facet could hinder the HER side reaction while simultaneously increasing hydrogenation in the NO_3RR. (i) Schematic represntation of the surface oxygen species role in the NO_3RR to NH_3 reaction on the (100) facet (a) and the (111) facet (b). (j) FE for different aspects of the Cu_2O structure. Reproduced from ref. 220 with permission from Elsevier, copyright 2023.

analyses[32,233] explained various reaction mechanisms involved in the electrochemical reduction of NO_3^-. For example, DFT calculations for Fe single-atom catalysts proposed a mechanism where the hydrogenation of NO_3^- serves as the initiation step, followed by the reduction of intermediates, including NO_2^-, HNO_2, NO, and the final product NH_3 (Fig. 27e).[32] Transition metals have also been found to form NOH_{ads} as an intermediate precursor for NH_3 synthesis (Fig. 27f) during the electrochemical reduction process.[233] This formation of NOH_{ads} occurs through H_2O-mediated hydrogenation of NO_{ads} which has a lower activation energy barrier compared with the dissociation of NO_{ads}. A similar mechanism has been reported for Cu-based solid catalyst, where NO_{ads} undergoes water-mediated hydrogenation to form NOH_{ads} (Fig. 27g).[234] Yao *et al.*[235] synthesized a Rh-based electrocatalyst and investigated the reaction intermediates in alkaline media *via* the use of surface-enhanced infrared-absorption spectroscopy and DEMS analysis and observed N_2H_2 as an intermediate of NH_3 production. N_2H_2 can be further split into N_2 and NH_3 production, although the dissociation into H_2 and N_2 or further reduction remains uncertain. The adsorption energy of the electrochemical reaction intermediate NO_{ads} is one of the most essential parameters that affect the product distribution in the electrochemical reduction of NO_3^-. Therefore the reduction of NO_{ads} is considered to precisely determine the selectivity of the reaction.[236–238] Moreover, the theoretical analysis of NO reduction on various metals disclosed that the binding strength of NO* is uncovered to predict the reactivity of NO, which is an important intermediate step for the NO_3^- reduction.[239] However, the supplied current density should also be carefully taken into consideration as a key parameter that can play a crucial role in influencing product distribution.[240] The nature, composition, and applied potential of the electrocatalysts play a vital role in determining selectivity

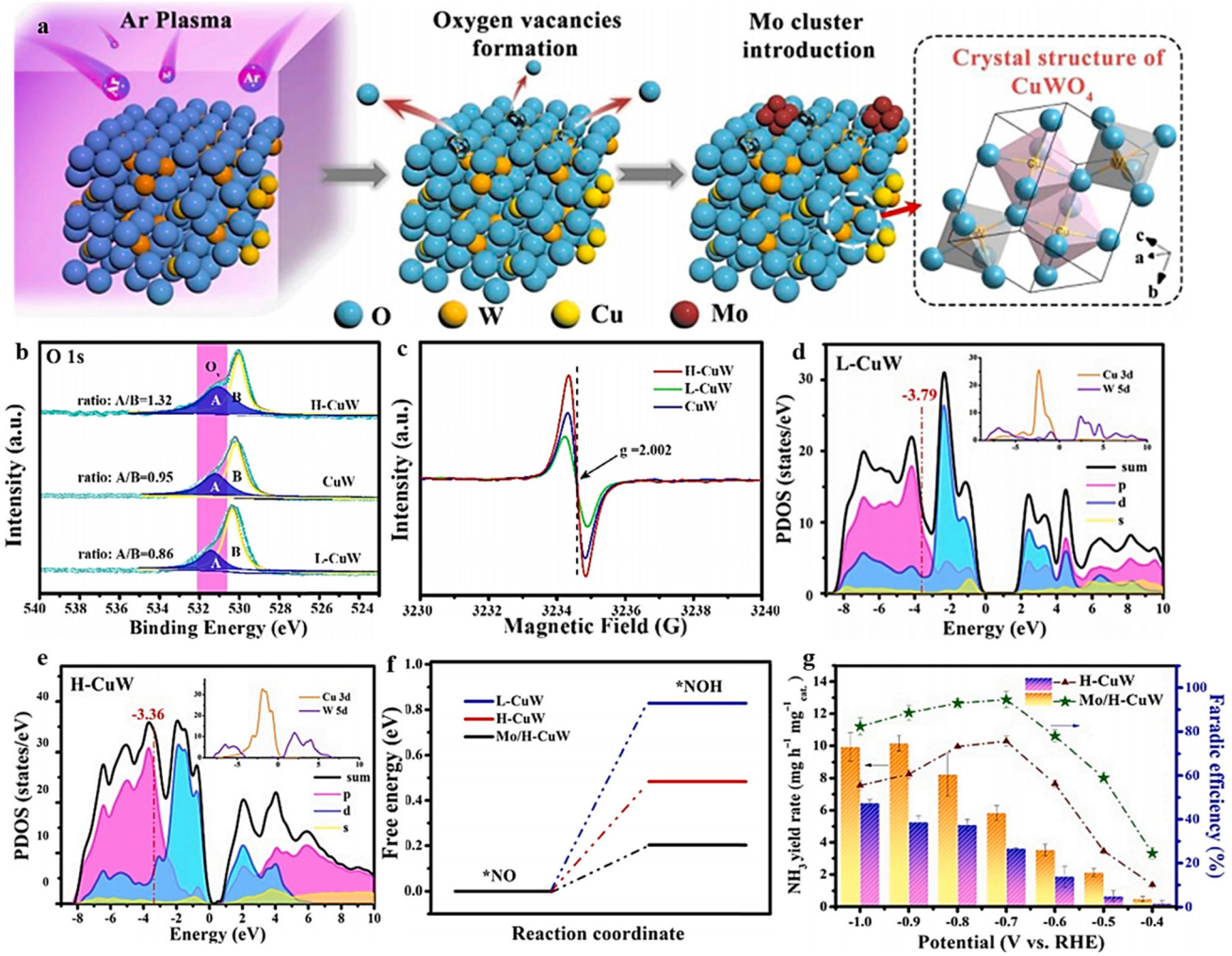

Fig. 26 (a) A diagrammatic representation of the steps involved in the Mo/H-CuW fabrication process. (b) and (c) show the XPS O 1s and EPR spectra of various materials. (d) PDOS of L-CuW and (e) PDOS of H-CuW, respectively. (f) A comparison of the changes in the Gibbs free energy that takes place during the rate-determining step of NO_3RR for L-CuW, H-CuW, and Mo/H-CuW. (g) The rate at which NH_3 is produced as well as the FE of H-CuW and Mo/H-CuW. Reproduced from ref. 221 with permission from Elsevier, copyright 2023.

in the electrochemical reduction of NO_3^-. In the study of Jia *et al.*[105] OVs were introduced into TiO_2 to unveil the reaction mechanism for the selective generation of NH_3. Different models of $TiO_2(101)$ surfaces were considered, including those with single OVs, two OVs, and without OVs. The density of states (DOS) analysis indicates that $TiO_2(101)$ without OVs exhibited semiconductor behavior. However, the introduction of OVs on the surface led to a switch in the Fermi level towards the conduction band minimum. This resulted from the excess 3d orbital electrons of Ti filling the OVs, giving rise to the metallic characteristic of TiO_{2-x} and improving the conductivity. This improved conductivity is beneficial for the electrochemical reduction reaction. The adsorption energy of NO_3^- on the surface of $TiO_2(101)$ was investigated for different configurations. It was found that $TiO_2(101)$ with a single inserted OV (−1.44 eV) or two OVs (−1.54 eV) showed much higher adsorption energy as compared with $TiO_2(101)$ without OVs (−0.71 eV) (Fig. 27i). This indicates a stronger binding of NO_3^- on TiO_2 surfaces with OVs. The reaction Gibbs free energy (ΔG) of NO_3^- was calculated for different configurations.

In the case of NO_3^- adsorption on the surface of $TiO_2(101)$ in the absence of OV, as shown in (Fig. 27j), the NO_3^- O1 makes bond-coordination *via* unsaturated Ti, while O2 and O3 are shown exposed to the ambient reaction environment. The NO_3* is hydrogenated and formed HNO_3*, in this case, H makes a bond with O3 which is the most suitable active site as compared with O1 and O2. The hydrogenation process continues, another proton–electron pair is caught by O3, and the previous intermediate HNO_3* leaves H to form NO_2* and a water molecule. NO_2* is automatically transformed to make NO_2 or HNO_2, thus further hindering the reduction of NO_2*. Considering $TiO_2(101)$ with the insertion of a single OV, the O1 of the NO_3* can participate in filling the OV site, and the O2 makes a bond with its neighboring unsaturated Ti (Fig. 27k). N-O1 bond is broken by adsorbing a proton-coupled with an electron with an energy release of 2.10 eV. Similarly,

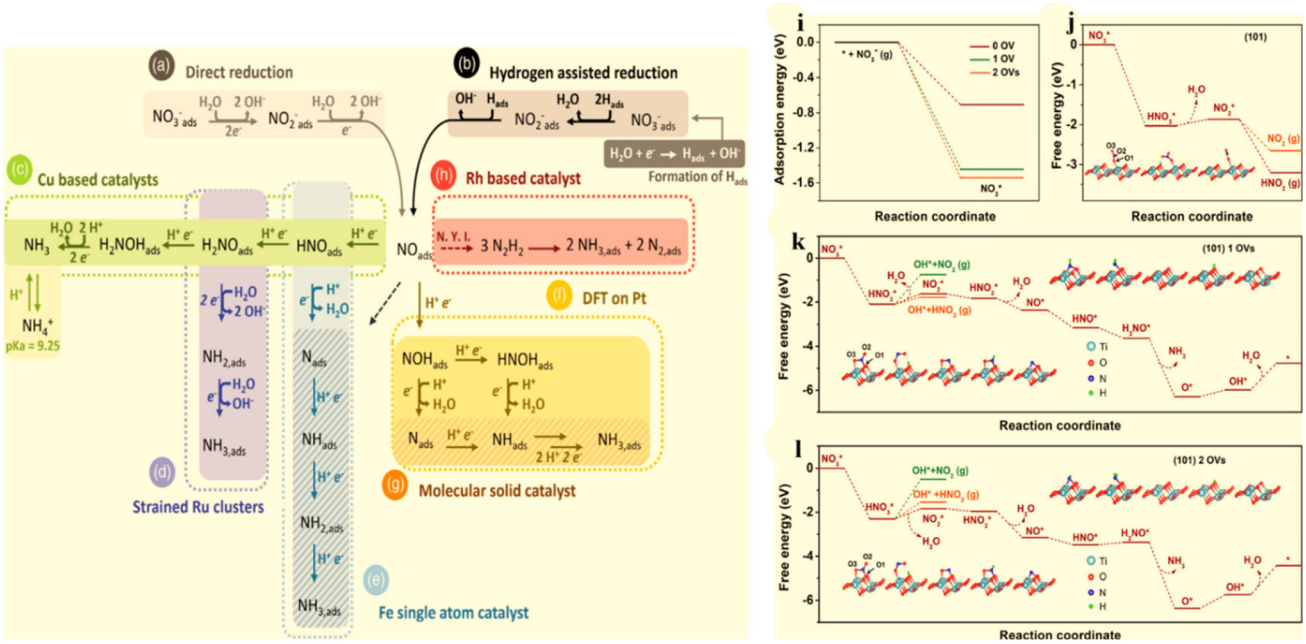

Fig. 27 (a–h) Proposed reaction pathways for ammonia synthesis reported by various latest literature reports.[241] (i) Nitrate adsorption energies on the surface of TiO_2(101) *via* zero, one and two OVs, (j) without OVs, (k) with one OV, and (l) two OVs at 0 V *vs.* RHE.[105] With permission from the American Chemical Society, copyright 2020.

O3 is attacked at a second proton–electron pair, making a coordination with an uphill energy change of 0.47 eV, and creates NO_2*. The possible probability of making HNO_2 byproducts with a smaller amount of energy release is 0.31 eV. N further activates and adsorbs the third proton to form HNO_2*. In a similar vein, O2 is released by the fourth hydrogenation step to form NO*. Moreover, three proton–electron pairs couple *via* N to form NH_3 gas, which leaves O1 on the OV site. Finally, O1 will be reduced by two protons to form water, recovering the oxygen vacancy on the surface. For TiO2 (101) with two vacancies, the nitrate reduction process is similar to that on one vacancy surface in (Fig. 6l), but in the form of two OVs on the surface of TiO_2(101), requiring a higher reaction barrier for HNO_2, and therefore inhibiting the undesired byproducts. In summary, OVs not only involve filling *via* oxygen in NO_3^- to lose the oxygen–nitrogen bond but also motivate the interaction of the NO_3RR intermediate and catalysts to control the reaction pathway and suppress the synthesis of parasitic byproducts.[105]

6. Conclusion, challenges, and perspectives

In conclusion, this review provides a comprehensive exploration of recent research advancements in catalysts focused on oxygen vacancies (OVs) and their critical role in the electrocatalytic conversion of NO_3^- into NH_3. This approach holds significant promise in its ability to surmount low energy barriers, address energy-related challenges, and make notable contributions to environmental sustainability. At the outset, our attention was directed toward elucidating the techniques for examining oxygen vacancies (OVs) in catalysts primarily based on metal oxides. Notably, we emphasized methods such as X-ray absorption spectroscopy (XAS), X-ray photoelectron spectroscopy (XPS), electron paramagnetic resonance (EPR) spectroscopy, and positron annihilation spectroscopy (PAS). Subsequently, we explored the methods frequently employed to generate OVs. The induction of OVs has been shown to effectively control the electronic properties, mitigate undesirable reactions, and enhance the catalytic activity for NO_3^- reduction. This technique opens new possibilities for the development of high-performance catalysts. However, there are still unresolved scientific inquiries that require further investigation to fully understand the significance and function of OVs in this context.

In terms of achieving a precise and controllable generation of OVs, it is important to modulate the contents of OVs and manipulate the position of defects in materials. This can be done to induce changes in the adsorption energies of intermediates and surface electronic configurations, ultimately impacting the overall performance of catalysts. The concentration of defects also plays a pivotal role in determining the effectiveness of OVs. While a low defect concentration may not yield significant improvements, an excessive number of defects can lead to structural distortion and impede further improvements in conductivity by restricting charge mobility. Recent studies have focused on the production of defective metal oxides, and researchers have reached a unanimous conclusion that the concentration of surface OVs in the oxides increases with prolonged plasma treatment. This increase in

OVs leads to alterations in the chemical state, a decline in crystallinity, and reduced conductivity.[47,243,244] However, an important question arises: is there a trade-off between the content of OVs and the catalytic behavior of defective catalysts? The mechanism by which an excessive quantity of OVs can trigger alterations in crystal structure and hinder charge transfer remains elusive and has yet to be fully understood. To address the aforementioned question, it is imperative to address these apprehensions, as they can contribute to a more comprehensive comprehension of the alterations in bulk and surface electronic distribution resulting from defects.

When considering the applicability of electrocatalysts for industrial applications, the stability of these catalysts becomes a crucial factor alongside their overall performance. However, a notable concern arises regarding the stability of OVs in different electrolyte environments. Although earlier studies have demonstrated the resilience of surface OVs under mild conditions through extensive long-term tests and *in situ* analysis,[111] their stability under harsh conditions remains a challenge. For instance, in highly alkaline media (1 M KOH), several studies have reported the disappearance of unsaturated vacancies, attributed to the replenishment influences of OH^- species present in the solution.[245] Additionally, the diffusion of O_2 can catalyze the oxidation of surface OVs, thereby impeding optimal electrocatalytic activity.[57] Furthermore, there is still a lack of comprehensive understanding regarding how factors such as electrolyte composition and catalyst assembly influence the stability of OVs. Several investigations have also revealed the mobility of OVs within the bulk of a metal oxide.[246,247] The continuous relocation of these OV defects can potentially lead to the development of microcracks in the catalyst.[248] When OVs are generated through H_2 treatment, the concurrent formation of surface OH groups and H_2 impurities is consistently observed. The presence of these impurities can impact the electronic behavior of MOs,[249,250] making it challenging to differentiate the specific effects attributed to oxygen vacancies from other potential factors.

The intermediate states of oxygen-defective MOs during these cycling processes remain unknown. Furthermore, surface OVs can activate dissolved O_2, leading to the formation of superoxide radicals.[251] These radicals can hinder the NO_3RR at the cathode.[252] Therefore, it is essential to gain a thorough understanding of the mechanistic effects of variables such as pH, dissolved O_2, and temperature on the stability of OVs, as well as their impact on the overall electrocatalytic reaction. This knowledge is particularly crucial due to the significant fluctuations of these variables in real wastewater streams. Furthermore, it is important to note that OVs could potentially introduce transitional layers within the electrocatalyst, especially in highly acidic or alkaline electrolytes. These transitional layers influence reaction pathways, which in turn impact the adsorption of intermediates and the rate-limiting steps. In addressing these complexities, there is a critical need for *in situ* characterization techniques that provide unequivocal evidence and in-depth insights into the reaction mechanisms. Methods like *in situ* Fourier-transform infrared spectroscopy (FTIR), *in situ* Raman spectroscopy, and *in situ* X-ray absorption fine structure (XAFS) spectroscopy offer real-time observations that can illuminate the dynamic interplay of OVs and NO_3RR mechanisms.

Despite these advancements, the current catalyst materials' performance falls short of seamless industrial application, warranting further refinement. A promising path lies in the integration of experimental observations and theoretical insights. This synergy has the potential to yield enhanced, durable, and cost-effective electrocatalysts for NO_3RR. By merging experimental findings with theoretical predictions, a comprehensive understanding can emerge, ushering in a new era of electrocatalytic platforms for NO_3RR that are both sustainable and industrially feasible.

Data availability

The data that support the findings of this review are available from the corresponding author upon reasonable request.

Conflicts of interest

The authors declared that there is no conflict of interest.

Acknowledgements

The authors acknowledge financial support from the National Natural Science Foundation of China (22178055 and 22108032), the Guangdong Basic and Applied Basic Research Foundation (2020A1515110820), and the Dongguan Introduction Program of Leading Innovative and Entrepreneurial Talents.

References

1 H. E. Kim, J. Kim, E. C. Ra, H. Zhang, Y. J. Jang and J. S. Lee, Photoelectrochemical Nitrate Reduction to Ammonia on Ordered Silicon Nanowire Array Photocathodes, *Angew. Chem., Int. Ed.*, 2022, **61**, e202204117.
2 Y. Wang, C. Wang, M. Li, Y. Yu and B. Zhang, Nitrate electroreduction: mechanism insight, in situ characterization, performance evaluation, and challenges, *Chem. Soc. Rev.*, 2021, **50**, 6720–6733.
3 B. H. Suryanto, H.-L. Du, D. Wang, J. Chen, A. N. Simonov and D. R. MacFarlane, Challenges and prospects in the catalysis of electroreduction of nitrogen to ammonia, *Nat. Catal.*, 2019, **2**, 290–296.
4 X. Liang, H. Zhu, X. Yang, S. Xue, Z. Liang, X. Ren, A. Liu and G. Wu, Recent Advances in Designing Efficient Electrocatalysts for Electrochemical Nitrate Reduction to Ammonia, *Small Struct.*, 2022, 2200202.
5 S. Zhang, X. Zhang, C. Liu, L. Pan, C. Shi, X. Zhang, Z.-F. Huang and J.-J. Zou, Theoretical and Experimental

Progress of Metal Electrocatalysts for Nitrogen Reduction Reaction, *Mater. Chem. Front.*, 2023, **7**, 643–661.
6 G. Marnellos and M. Stoukides, Ammonia synthesis at atmospheric pressure, *Science*, 1998, **282**, 98–100.
7 H. Liu, J. Timoshenko, L. Bai, Q. Li, M. Rüscher, C. Sun, B. Roldan Cuenya and J. Luo, Low-Coordination Rhodium Catalysts for an Efficient Electrochemical Nitrate Reduction to Ammonia, *ACS Catal.*, 2023, **13**, 1513–1521.
8 X. Zhang, Y. Wang, C. Liu, Y. Yu, S. Lu and B. Zhang, Recent advances in non-noble metal electrocatalysts for nitrate reduction, *Chem. Eng. J.*, 2021, **403**, 126269.
9 D. Kim, K. Alam, M.-K. Han, S. Surendran, J. Lim, J. Y. Kim, D. J. Moon, G. Jeong, M. G. Kim and G. Kwon, Manipulating wettability of catalytic surface for improving ammonia production from electrochemical nitrogen reduction, *J. Colloid Interface Sci.*, 2023, **633**, 53–59.
10 T.-Y. An, S. Surendran, S. C. Jesudass, H. Lee, D. J. Moon, J. K. Kim and U. Sim, Promoting electrochemical ammonia synthesis by synergized performances of Mo2C-Mo2N heterostructure, *Front. Chem.*, 2023, **11**, 1122150.
11 M. S. Yu, S. C. Jesudass, S. Surendran, J. Y. Kim, U. Sim and M.-K. Han, Synergistic interaction of MoS2 nanoflakes on La2Zr2O7 nanofibers for improving photoelectrochemical nitrogen reduction, *ACS Appl. Mater. Interfaces*, 2022, **14**, 31889–31899.
12 D. Kim, S. Surendran, G. Janani, Y. Lim, H. Choi, M.-K. Han, S. Yuvaraj, T.-H. Kim, J. K. Kim and U. Sim, Nitrogen-impregnated carbon-coated TiO2 nanoparticles for N2 reduction to ammonia under ambient conditions, *Mater. Lett.*, 2022, **314**, 131808.
13 S. C. Jesudass, S. Surendran, J. Y. Kim, T.-Y. An, G. Janani, T.-H. Kim, J. K. Kim and U. Sim, Pathways of the Electrochemical Nitrogen Reduction Reaction: From Ammonia Synthesis to Metal-N2 Batteries, *Electrochem. Energy Rev.*, 2023, **6**, 27.
14 S. L. Foster, S. I. P. Bakovic, R. D. Duda, S. Maheshwari, R. D. Milton, S. D. Minteer, M. J. Janik, J. N. Renner and L. F. Greenlee, Catalysts for nitrogen reduction to ammonia, *Nat. Catal.*, 2018, **1**, 490–500.
15 S. J. Li, D. Bao, M. M. Shi, B. R. Wulan, J. M. Yan and Q. Jiang, Amorphizing of Au nanoparticles by CeOx–RGO hybrid support towards highly efficient electrocatalyst for N2 reduction under ambient conditions, *Adv. Mater.*, 2017, **29**, 1700001.
16 G.-F. Chen, X. Cao, S. Wu, X. Zeng, L.-X. Ding, M. Zhu and H. Wang, Ammonia electrosynthesis with high selectivity under ambient conditions via a Li+ incorporation strategy, *J. Am. Chem. Soc.*, 2017, **139**, 9771–9774.
17 C. Tang and S.-Z. Qiao, How to explore ambient electrocatalytic nitrogen reduction reliably and insightfully, *Chem. Soc. Rev.*, 2019, **48**, 3166–3180.
18 P. H. van Langevelde, I. Katsounaros and M. T. Koper, Electrocatalytic nitrate reduction for sustainable ammonia production, *Joule*, 2021, **5**, 290–294.
19 J. X. Yao, D. Bao, Q. Zhang, M. M. Shi, Y. Wang, R. Gao, J. M. Yan and Q. Jiang, Tailoring oxygen vacancies of BiVO4 toward highly efficient noble–metal–free electrocatalyst for artificial N2 fixation under ambient conditions, *Small Methods*, 2019, **3**, 1800333.
20 J. Li, G. Zhan, J. Yang, F. Quan, C. Mao, Y. Liu, B. Wang, F. Lei, L. Li and A. W. Chan, Efficient ammonia electrosynthesis from nitrate on strained ruthenium nanoclusters, *J. Am. Chem. Soc.*, 2020, **142**, 7036–7046.
21 L. Li, C. Tang, X. Cui, Y. Zheng, X. Wang, H. Xu, S. Zhang, T. Shao, K. Davey and S. Z. Qiao, Efficient nitrogen fixation to ammonia through integration of plasma oxidation with electrocatalytic reduction, *Angew. Chem.*, 2021, **133**, 14250–14256.
22 F. Ye, S. Zhang, Q. Cheng, Y. Long, D. Liu, R. Paul, Y. Fang, Y. Su, L. Qu and L. Dai, The role of oxygen-vacancy in bifunctional indium oxyhydroxide catalysts for electrochemical coupling of biomass valorization with CO2 conversion, *Nat. Commun.*, 2023, **14**, 2040.
23 C. J. Van der Ham, M. T. Koper and D. G. Hetterscheid, Challenges in reduction of dinitrogen by proton and electron transfer, *Chem. Soc. Rev.*, 2014, **43**, 5183–5191.
24 A. R. Singh, B. A. Rohr, J. A. Schwalbe, M. Cargnello, K. Chan, T. F. Jaramillo, I. Chorkendorff and J. K. Nørskov, Electrochemical Ammonia Synthesis. The Selectivity Challenge, *ACS Catal.*, 2017, **7**, 706–709.
25 V. Rosca and M. T. Koper, Mechanism of electrocatalytic reduction of nitric oxide on Pt (100), *J. Phys. Chem. B*, 2005, **109**, 16750–16759.
26 A. De Vooys, M. Koper, R. Van Santen and J. Van Veen, Mechanistic study of the nitric oxide reduction on a polycrystalline platinum electrode, *Electrochim. Acta*, 2001, **46**, 923–930.
27 D. Kim, D. Shin, J. Heo, H. Lim, J.-A. Lim, H. M. Jeong, B.-S. Kim, I. Heo, I. Oh and B. Lee, Unveiling electrode–electrolyte design-based NO reduction for NH3 synthesis, *ACS Energy Lett.*, 2020, **5**, 3647–3656.
28 Y. Zeng, C. Priest, G. Wang and G. Wu, Restoring the nitrogen cycle by electrochemical reduction of nitrate: progress and prospects, *Small Methods*, 2020, **4**, 2000672.
29 Y. Ren, C. Yu, L. Wang, X. Tan, Z. Wang, Q. Wei, Y. Zhang and J. Qiu, Microscopic-Level Insights into the Mechanism of Enhanced NH3 Synthesis in Plasma-Enabled Cascade N2 Oxidation–Electroreduction System, *J. Am. Chem. Soc.*, 2022, **144**, 10193–10200.
30 F.-Y. Chen, Z.-Y. Wu, S. Gupta, D. J. Rivera, S. V. Lambeets, S. Pecaut, J. Y. T. Kim, P. Zhu, Y. Z. Finfrock and D. M. Meira, Efficient conversion of low-concentration nitrate sources into ammonia on a Ru-dispersed Cu nanowire electrocatalyst, *Nat. Nanotechnol.*, 2022, **17**, 759–767.
31 W. Jung and Y. J. Hwang, Material strategies in the electrochemical nitrate reduction reaction to ammonia production, *Mater. Chem. Front.*, 2021, **5**, 6803–6823.
32 Z.-Y. Wu, M. Karamad, X. Yong, Q. Huang, D. A. Cullen, P. Zhu, C. Xia, Q. Xiao, M. Shakouri and F.-Y. Chen,

Electrochemical ammonia synthesis via nitrate reduction on Fe single atom catalyst, *Nat. Commun.*, 2021, **12**, 2870.
33 W. Chen, X. Yang, Z. Chen, Z. Ou, J. Hu, Y. Xu, Y. Li, X. Ren, S. Ye, J. Qiu, J. Liu and Q. Zhang, Emerging Applications, Developments, Prospects, and Challenges of Electrochemical Nitrate-to-Ammonia Conversion, *Adv. Funct. Mater.*, 2023, **33**, 2300512.
34 H. Shen, C. Choi, J. Masa, X. Li, J. Qiu, Y. Jung and Z. Sun, Electrochemical ammonia synthesis: mechanistic understanding and catalyst design, *Chem*, 2021, **7**, 1708–1754.
35 Y. Li, Q. Zhang, Z. Mei, S. Li, W. Luo, F. Pan, H. Liu and S. Dou, Recent advances and perspective on electrochemical ammonia synthesis under ambient conditions, *Small Methods*, 2021, **5**, 2100460.
36 Z. Xu, L. Wan, Y. Liao, M. Pang, Q. Xu, P. Wang and B. Wang, Continuous ammonia electrosynthesis using physically interlocked bipolar membrane at 1000 mA cm−2, *Nat. Commun.*, 2023, **14**, 1619.
37 W. Chen, X. Yang, Z. Chen, Z. Ou, J. Hu, Y. Xu, Y. Li, X. Ren, S. Ye and J. Qiu, Emerging Applications, Developments, Prospects, and Challenges of Electrochemical Nitrate–to–Ammonia Conversion, *Adv. Funct. Mater.*, 2023, 2300512.
38 K. Fan, W. Xie, J. Li, Y. Sun, P. Xu, Y. Tang, Z. Li and M. Shao, Active hydrogen boosts electrochemical nitrate reduction to ammonia, *Nat. Commun.*, 2022, **13**, 7958.
39 S. Han, H. Li, T. Li, F. Chen, R. Yang, Y. Yu and B. Zhang, Ultralow overpotential nitrate reduction to ammonia via a three-step relay mechanism, *Nat. Catal.*, 2023, 1–13.
40 S. N. V. Skorodumova, S. S. I. Simak, L. B. I. Lundqvist, A. I. A. Abrikosov and J. B. Johansson, Quantum origin of the oxygen storage capability of ceria, *Phys. Rev. Lett.*, 2002, **89**, DOI: 10.1103/PhysRevLett.89.166601.
41 C. Belkessam, S. Bencherif, M. Mechouet, N. Idiri and J. Ghilane, The effect of heteroatom doping on nickel cobalt oxide electrocatalysts for oxygen evolution and reduction reactions, *ChemPlusChem*, 2020, **85**, 1710–1718.
42 X. Fan, D. Zhao, Z. Deng, L. Zhang, J. Li, Z. Li, S. Sun, Y. Luo, D. Zheng and Y. Wang, Constructing Co@ TiO2 Nanoarray Heterostructure with Schottky Contact for Selective Electrocatalytic Nitrate Reduction to Ammonia, *Small*, 2023, 2208036.
43 Y. Wang, A. Xu, Z. Wang, L. Huang, J. Li, F. Li, J. Wicks, M. Luo, D.-H. Nam and C.-S. Tan, Enhanced nitrate-to-ammonia activity on copper–nickel alloys via tuning of intermediate adsorption, *J. Am. Chem. Soc.*, 2020, **142**, 5702–5708.
44 B. Bi, A.-Q. Dong, M.-M. Shi, X.-F. Sun, H.-R. Li, X. Kang, R. Gao, Z. Meng, Z.-Y. Chen and T.-W. Xu, Efficient Ammonia Synthesis from Nitrate Catalyzed by Au/Cu with Enhanced Adsorption Ability, *Small Struct.*, 2022, 2200308.
45 X. Fu, J. B. Pedersen, Y. Zhou, M. Saccoccio, S. Li, R. Sažinas, K. Li, S. Z. Andersen, A. Xu and N. H. Deissler, Continuous-flow electrosynthesis of ammonia by nitrogen reduction and hydrogen oxidation, *Science*, 2023, **379**, 707–712.
46 X.-H. Wang, Z.-M. Wang, Q.-L. Hong, Z.-N. Zhang, F. Shi, D.-S. Li, S.-N. Li and Y. Chen, Oxygen-Vacancy-Rich Cu2O Hollow Nanocubes for Nitrate Electroreduction Reaction to Ammonia in a Neutral Electrolyte, *Inorg. Chem.*, 2022, **61**, 15678–15685.
47 R. Daiyan, T. Tran-Phu, P. Kumar, K. Iputera, Z. Tong, J. Leverett, M. H. A. Khan, A. A. Esmailpour, A. Jalili and M. Lim, Nitrate reduction to ammonium: from CuO defect engineering to waste NO x-to-NH 3 economic feasibility, *Energy Environ. Sci.*, 2021, **14**, 3588–3598.
48 Q. Zeng, G. Yang, J. Chen, Q. Zhang, Z. Liu, B. Qin and F. Peng, Effects of nitrogen and oxygen on electrochemical reduction of CO2 in nitrogen-doped carbon black, *Carbon*, 2023, **202**, 1–11.
49 P. Shen, G. Wang, K. Chen, J. Kang, D. Ma and K. Chu, Selenium-vacancy-rich WSe2 for nitrate electroreduction to ammonia, *J. Colloid Interface Sci.*, 2023, **629**, 563–570.
50 Y. Luo, K. Chen, G. Wang, G. Zhang, N. Zhang and K. Chu, Ce-doped MoS 2− x nanoflower arrays for electrocatalytic nitrate reduction to ammonia, *Inorg. Chem. Front.*, 2023, **10**, 1543–1551.
51 G. Zhang, N. Zhang, K. Chen, X. Zhao and K. Chu, Atomically Mo-Doped SnO2-x for Efficient Nitrate Electroreduction to Ammonia, *J. Colloid Interface Sci.*, 2023, **649**, 724–730.
52 E. Marelli, J. Gazquez, E. Poghosyan, E. Müller, D. J. Gawryluk, E. Pomjakushina, D. Sheptyakov, C. Piamonteze, D. Aegerter and T. J. Schmidt, Correlation between oxygen vacancies and oxygen evolution reaction activity for a model electrode: PrBaCo2O5+ δ, *Angew. Chem., Int. Ed.*, 2021, **60**, 14609–14619.
53 Y. Huang, M. Li, F. Pan, Z. Zhu, H. Sun, Y. Tang and G. Fu, Plasma–induced Mo–doped Co3O4 with enriched oxygen vacancies for electrocatalytic oxygen evolution in water splitting, *Carbon Energy*, 2023, **5**, e279.
54 Q. Ji, L. Bi, J. Zhang, H. Cao and X. S. Zhao, The role of oxygen vacancies of ABO 3 perovskite oxides in the oxygen reduction reaction, *Energy Environ. Sci.*, 2020, **13**, 1408–1428.
55 Q. Zhuang, N. Ma, Z. Yin, X. Yang, Z. Yin, J. Gao, Y. Xu, Z. Gao, H. Wang and J. Kang, Rich surface oxygen vacancies of MnO_2 for enhancing electrocatalytic oxygen reduction and oxygen evolution reactions, *Adv. Energy Sustainability Res.*, 2021, **2**, 2100030.
56 L. Li, Z.-J. Zhao, C. Hu, P. Yang, X. Yuan, Y. Wang, L. Zhang, L. Moskaleva and J. Gong, Tuning oxygen vacancies of oxides to promote electrocatalytic reduction of carbon dioxide, *ACS Energy Lett.*, 2020, **5**, 552–558.
57 Q. He, Y. Zhang, H. Li, Y. Yang, S. Chen, W. Yan, J. Dong, X. M. Zhang and X. Fan, Engineering Steam Induced Surface Oxygen Vacancy onto Ni–Fe Bimetallic Nanocomposite for CO2 Electroreduction, *Small*, 2022, **18**, 2108034.
58 G. Li, H. Jang, S. Liu, Z. Li, M. G. Kim, Q. Qin, X. Liu and J. Cho, The synergistic effect of Hf-O-Ru bonds and

oxygen vacancies in Ru/HfO2 for enhanced hydrogen evolution, *Nat. Commun.*, 2022, **13**, 1270.

59 Z. Wu, P. Yang, Q. Li, W. Xiao, Z. Li, G. Xu, F. Liu, B. Jia, T. Ma and S. Feng, Microwave synthesis of Pt clusters on black TiO2 with abundant oxygen vacancies for efficient acidic electrocatalytic hydrogen evolution, *Angew. Chem.*, 2023, **135**, e202300406.

60 X. Xu, L. Hu, Z. Li, L. Xie, S. Sun, L. Zhang, J. Li, Y. Luo, X. Yan and M. S. Hamdy, Oxygen vacancies in Co 3 O 4 nanoarrays promote nitrate electroreduction for ammonia synthesis, *Sustainable Energy Fuels*, 2022, **6**, 4130–4136.

61 S. Zhao, Y. Yang, F. Bi, Y. Chen, M. Wu, X. Zhang and G. Wang, Oxygen vacancies in the catalyst: Efficient degradation of gaseous pollutants, *Chem. Eng. J.*, 2023, **454**, 140376.

62 J. Kumar, H. J. Jung, R. R. Neiber, R. A. Soomro, Y. J. Kwon, N. U. Hassan, M. Shon, J. H. Lee, K. Y. Baek and K. Y. Cho, Recent advances in oxygen deficient metal oxides: Opportunities as supercapacitor electrodes, *Int. J. Energy Res.*, 2022, **46**, 7055–7081.

63 W. Hou, P. Feng, X. Guo, Z. Wang, Z. Bai, Y. Bai, G. Wang and K. Sun, Catalytic mechanism of oxygen vacancies in perovskite oxides for lithium–sulfur batteries, *Adv. Mater.*, 2022, **34**, 2202222.

64 G. Cui, Y. Zeng, J. Wu, Y. Guo, X. Gu and X. W. Lou, Synthesis of Nitrogen–Doped KMn8O16 with Oxygen Vacancy for Stable Zinc–Ion Batteries, *Adv. Sci.*, 2022, **9**, 2106067.

65 G. Zhang, Q. Ji, K. Zhang, Y. Chen, Z. Li, H. Liu, J. Li and J. Qu, Triggering surface oxygen vacancies on atomic layered molybdenum dioxide for a low energy consumption path toward nitrogen fixation, *Nano Energy*, 2019, **59**, 10–16.

66 L. Zhang, F. Xie, J. Liu, Z. Sun, X. Zhang, Y. Wang, Y. Wang, R. Li and C. Fan, Light-Switchable Oxygen Vacancies Enhanced Nitrogen Fixation Performance on BiOBr: Mechanism of Formation, Reconversion and Function, *Chem. Eng. J.*, 2022, **450**, 138066.

67 H. M. A. Sharif, T. Li, N. Mahmood, M. Ahmad, J. Xu, A. Mahmood, R. Djellabi and B. Yang, Thermally activated epoxy-functionalized carbon as an electrocatalyst for efficient NOx reduction, *Carbon*, 2021, **182**, 516–524.

68 Z. Zhao, Y. Chen, Y. Liu, Y. Zhao, Z. Zhang, K. Zhang, Z. Mo, C. Wang and S. Gao, Atomic catalyst supported on oxygen defective MXenes for synergetic electrocatalytic nitrate reduction to ammonia: A first principles study, *Appl. Surf. Sci.*, 2023, **614**, 156077.

69 W. Jiang, H. Loh, B. Q. L. Low, H. Zhu, J. Low, J. Z. X. Heng, K. Y. Tang, Z. Li, X. J. Loh and E. Ye, Role of oxygen vacancy in metal oxides for photocatalytic CO2 reduction, *Appl. Catal., B*, 2022, 122079.

70 Z. Wang, R. Lin, Y. Huo, H. Li and L. Wang, Formation, detection, and function of oxygen vacancy in metal oxides for solar energy conversion, *Adv. Funct. Mater.*, 2022, **32**, 2109503.

71 J. Sun, C. Ge, D. An, Q. Tong, F. Gao and L. Dong, Characterization of oxygen vacancies in rare earth cerium based catalytic materials, *J. Chem. Eng.*, 2020, **71**, 3403–3415.

72 A. Puigdollers, P. Schlexer, S. Tosoni and G. Pacchioni, Increasing Oxide Reducibility: The Role of Metal/Oxide Interfaces in the Formation of Oxygen Vacancies, *ACS Catal.*, 2017, **7**, 6493–6513.

73 Z. Wang and L. Wang, Role of oxygen vacancy in metal oxide based photoelectrochemical water splitting, *EcoMat*, 2021, **3**, e12075.

74 P. Devi, R. Verma and J. P. Singh, Advancement in electrochemical, photocatalytic, and photoelectrochemical CO2 reduction: Recent progress in the role of oxygen vacancies in catalyst design, *J. CO2 Util.*, 2022, **65**, 102211.

75 R. Schaub, E. Wahlstrom, A. Rønnau, E. Lægsgaard, I. Stensgaard and F. Besenbacher, Oxygen-mediated diffusion of oxygen vacancies on the TiO2 (110) surface, *Science*, 2003, **299**, 377–379.

76 F. Liu and Z. Fan, Defect engineering of two-dimensional materials for advanced energy conversion and storage, *Chem. Soc. Rev.*, 2023, **52**, 1723–1772.

77 G. Pacchioni, Oxygen vacancy: the invisible agent on oxide surfaces, *ChemPhysChem*, 2003, **4**, 1041–1047.

78 K. Chu, F. Liu, J. Zhu, H. Fu, H. Zhu, Y. Zhu, Y. Zhang, F. Lai and T. Liu, A general strategy to boost electrocatalytic nitrogen reduction on perovskite oxides via the oxygen vacancies derived from a–site deficiency, *Adv. Energy Mater.*, 2021, **11**, 2003799.

79 E. Scorza, U. Birkenheuer and C. Pisani, The oxygen vacancy at the surface and in bulk MgO: an embedded-cluster study, *J. Chem. Phys.*, 1997, **107**, 9645–9658.

80 T. S. Bui, E. C. Lovell, R. Daiyan and R. Amal, Defective Metal Oxides: Lessons From CO2RR and Applications in NOxRR, *Adv. Mater.*, 2023, 2205814.

81 S. C. Yang, W. N. Su, J. Rick, S. D. Lin, J. Y. Liu, C. J. Pan, J. F. Lee and B. J. Hwang, Oxygen vacancy engineering of cerium oxides for carbon dioxide capture and reduction, *ChemSusChem*, 2013, **6**, 1326–1329.

82 Y. Liu, P. Deng, R. Wu, X. Zhang, C. Sun and H. Li, Oxygen vacancies for promoting the electrochemical nitrogen reduction reaction, *J. Mater. Chem. A*, 2021, **9**, 6694–6709.

83 M. Castell, P. Wincott, N. Condon, C. Muggelberg, G. Thornton, S. Dudarev, A. Sutton and G. Briggs, Atomic-resolution STM of a system with strongly correlated electrons: NiO (001) surface structure and defect sites, *Phys. Rev. B: Condens. Matter Mater. Phys.*, 1997, **55**, 7859.

84 H. Zheng, Y. Zhang, Y. Wang, Z. Wu, F. Lai, G. Chao, N. Zhang, L. Zhang and T. Liu, Perovskites with Enriched Oxygen Vacancies as a Family of Electrocatalysts for Efficient Nitrate Reduction to Ammonia, *Small*, 2023, **19**, 2205625.

85 E. Shoko, M. Smith and R. H. McKenzie, Charge distribution near bulk oxygen vacancies in cerium oxides, *J. Phys.: Condens. Matter*, 2010, **22**, 223201.

86 J. Nowotny, T. Bak and M. A. Alim, Defect disorder of TiO2. Equilibrium constant for the formation of oxygen vacancies, *ECS Solid State Lett.*, 2014, **3**, Q71.
87 R. Liu, Y. Wang, D. Liu, Y. Zou and S. Wang, Water–plasma–enabled exfoliation of ultrathin layered double hydroxide nanosheets with multivacancies for water oxidation, *Adv. Mater.*, 2017, **29**, 1701546.
88 A. Gloystein, M. Soltanmohammadi and N. Nilius, Light Emission from Single Oxygen Vacancies in Cu2O Films Probed with Scanning Tunneling Microscopy, *J. Phys. Chem. Lett.*, 2023, **14**, 3980–3985.
89 Y. Liu, Y. Peng, M. Naschitzki, S. Gewinner, W. Schöllkopf, H. Kuhlenbeck, R. Pentcheva and B. Cuenya, Surface oxygen vacancies on reduced Co3O4 (100): superoxide formation and ultra–low–temperature CO oxidation, *Angew. Chem., Int. Ed.*, 2021, **60**, 16514–16520.
90 X. Jiang, Y. Zhang, J. Jiang, Y. Rong, Y. Wang, Y. Wu and C. Pan, Characterization of oxygen vacancy associates within hydrogenated TiO2: a positron annihilation study, *J. Phys. Chem. C*, 2012, **116**, 22619–22624.
91 J. Di, C. Chen, C. Zhu, R. Long, H. Chen, X. Cao, J. Xiong, Y. Weng, L. Song and S. Li, Surface local polarization induced by bismuth–oxygen vacancy pairs tuning non–covalent interaction for CO2 photoreduction, *Adv. Energy Mater.*, 2021, **11**, 2102389.
92 D. Roehrens, J. Brendt, D. Samuelis and M. Martin, On the ammonolysis of Ga2O3: An XRD, neutron diffraction and XAS investigation of the oxygen-rich part of the system Ga2O3–GaN, *J. Solid State Chem.*, 2010, **183**, 532–541.
93 P. M. Csernica, S. S. Kalirai, W. E. Gent, K. Lim, Y.-S. Yu, Y. Liu, S.-J. Ahn, E. Kaeli, X. Xu and K. H. Stone, Persistent and partially mobile oxygen vacancies in Li-rich layered oxides, *Nat. Energy*, 2021, **6**, 642–652.
94 J. Yano and V. K. Yachandra, X-ray absorption spectroscopy, *Photosynth. Res.*, 2009, **102**, 241–254.
95 R. U. Chandrasena, W. Yang, Q. Lei, M. U. Delgado-Jaime, K. D. Wijesekara, M. Golalikhani, B. A. Davidson, E. Arenholz, K. Kobayashi and M. Kobata, Strain-engineered oxygen vacancies in CaMnO3 thin films, *Nano Lett.*, 2017, **17**, 794–799.
96 K. Zhu, S. Wei, H. Shou, F. Shen, S. Chen, P. Zhang, C. Wang, Y. Cao, X. Guo and M. Luo, Defect engineering on V2O3 cathode for long-cycling aqueous zinc metal batteries, *Nat. Commun.*, 2021, **12**, 6878.
97 D. Cho, C. Min, J. Kim, J. Park, S. Oh and C. Hwang, X-ray absorption spectroscopy study on oxygen-deficient hafnium oxide film, *J. Phys.: Conf. Ser.*, 2008, DOI: 10.1088/1742-6596/100/4/042044.
98 S. Gao, Z. Sun, W. Liu, X. Jiao, X. Zu, Q. Hu, Y. Sun, T. Yao, W. Zhang and S. Wei, Atomic layer confined vacancies for atomic-level insights into carbon dioxide electroreduction, *Nat. Commun.*, 2017, **8**, 14503.
99 A. Cezar, I. Graff, J. Varalda, W. Schreiner and D. Mosca, Oxygen-vacancy-induced room-temperature magnetization in lamellar V2O5 thin films, *J. Appl. Phys.*, 2014, **116**, 163904.
100 R.-A. Eichel, Structural and dynamic properties of oxygen vacancies in perovskite oxides—analysis of defect chemistry by modern multi-frequency and pulsed EPR techniques, *Phys. Chem. Chem. Phys.*, 2011, **13**, 368–384.
101 K. Ye, K. Li, Y. Lu, Z. Guo, N. Ni, H. Liu, Y. Huang, H. Ji and P. Wang, An overview of advanced methods for the characterization of oxygen vacancies in materials, *TrAC, Trends Anal. Chem.*, 2019, **116**, 102–108.
102 V. Laguta and M. Nikl, Electron spin resonance of paramagnetic defects and related charge carrier traps in complex oxide scintillators, *Phys. Status Solidi B*, 2013, **250**, 254–260.
103 H. Du, H. Guo, K. Wang, X. Du, B. A. Beshiwork, S. Sun, Y. Luo, Q. Liu, T. Li and X. Sun, Durable electrocatalytic reduction of nitrate to ammonia over defective pseudobrookite Fe2TiO5 nanofibers with abundant oxygen vacancies, *Angew. Chem.*, 2023, **135**, e202215782.
104 Y. He, J. Sheng, Q. Ren, Y. Sun, W. Hao and F. Dong, Operando Identification of Dynamic Photoexcited Oxygen Vacancies as True Catalytic Active Sites, *ACS Catal.*, 2022, **13**, 191–203.
105 R. Jia, Y. Wang, C. Wang, Y. Ling, Y. Yu and B. Zhang, Boosting selective nitrate electroreduction to ammonium by constructing oxygen vacancies in TiO2, *ACS Catal.*, 2020, **10**, 3533–3540.
106 X. Zhang, C. Wang, Y. Guo, B. Zhang, Y. Wang and Y. Yu, Cu clusters/TiO 2− x with abundant oxygen vacancies for enhanced electrocatalytic nitrate reduction to ammonia, *J. Mater. Chem. A*, 2022, **10**, 6448–6453.
107 I. T. Awan, G. Lozano, M. Pereira-da-Silva, R. Romano, V. Rivera, S. Ferreira and E. Marega, Understanding the electronic properties of BaTiO 3 and Er 3+ doped BaTiO 3 films through confocal scanning microscopy and XPS: the role of oxygen vacancies, *Phys. Chem. Chem. Phys.*, 2020, **22**, 15022–15034.
108 G. Greczynski, R. T. Haasch, N. Hellgren, E. Lewin and L. Hultman, X-ray photoelectron spectroscopy of thin films, *Nat. Rev. Methods Primers*, 2023, **3**, 40.
109 L. Xu, W. Zhou, S. Chao, Y. Liang, X. Zhao, C. Liu and J. Xu, Advanced Oxygen–Vacancy Ce–Doped MoO3 Ultrathin Nanoflakes Anode Materials Used as Asymmetric Supercapacitors with Ultrahigh Energy Density, *Adv. Energy Mater.*, 2022, **12**, 2200101.
110 J. Zhang, R. Yin, Q. Shao, T. Zhu and X. Huang, Oxygen vacancies in amorphous InOx nanoribbons enhance CO2 adsorption and activation for CO2 electroreduction, *Angew. Chem., Int. Ed.*, 2019, **58**, 5609–5613.
111 Z. Geng, X. Kong, W. Chen, H. Su, Y. Liu, F. Cai, G. Wang and J. Zeng, Oxygen vacancies in ZnO nanosheets enhance CO2 electrochemical reduction to CO, *Angew. Chem.*, 2018, **130**, 6162–6167.
112 F. Lei, Y. Sun, K. Liu, S. Gao, L. Liang, B. Pan and Y. Xie, Oxygen vacancies confined in ultrathin indium oxide porous sheets for promoted visible-light water splitting, *J. Am. Chem. Soc.*, 2014, **136**, 6826–6829.

113 Y. Xiong, Q. Zhong, M. Ou, W. Cai, S. Wan, Y. Yu and S. Zhang, Efficient Inhibition of N2O during NO Absorption Process Using a CuO and (NH4)2SO3 Mixed Solution, *Ind. Eng. Chem. Res.*, 2018, **57**, 13010–13018.

114 L. Xu, Q. Jiang, Z. Xiao, X. Li, J. Huo, S. Wang and L. Dai, Plasma–engraved Co3O4 nanosheets with oxygen vacancies and high surface area for the oxygen evolution reaction, *Angew. Chem.*, 2016, **128**, 5363–5367.

115 J. Bao, X. Zhang, B. Fan, J. Zhang, M. Zhou, W. Yang, X. Hu, H. Wang, B. Pan and Y. Xie, Ultrathin spinel–structured nanosheets rich in oxygen deficiencies for enhanced electrocatalytic water oxidation, *Angew. Chem.*, 2015, **127**, 7507–7512.

116 G. Brauer, W. Anwand, D. Grambole, J. Grenzer, W. Skorupa, J. Čížek, J. Kuriplach, I. Procházka, C. Ling and C. So, Identification of Zn-vacancy–hydrogen complexes in ZnO single crystals: A challenge to positron annihilation spectroscopy, *Phys. Rev. B: Condens. Matter Mater. Phys.*, 2009, **79**, 115212.

117 T. Stassin, R. Verbeke, A. J. Cruz, S. Rodríguez-Hermida, I. Stassen, J. Marreiros, M. Krishtab, M. Dickmann, W. Egger and I. F. Vankelecom, Porosimetry for Thin Films of Metal–Organic Frameworks: A Comparison of Positron Annihilation Lifetime Spectroscopy and Adsorption–Based Methods, *Adv. Mater.*, 2021, **33**, 2006993.

118 F. Tuomisto, Identification of Point Defects in Multielement Compounds and Alloys with Positron Annihilation Spectroscopy: Challenges and Opportunities, *Phys. Status Solidi RRL*, 2021, **15**, 2100177.

119 X. Shen, G. Dong, L. Wang, L. Ye and J. Sun, Enhancing photocatalytic activity of NO removal through an in situ control of oxygen vacancies in growth of TiO2, *Adv. Mater. Interfaces*, 2019, **6**, 1901032.

120 Y. Yang, L. C. Yin, Y. Gong, P. Niu, J. Q. Wang, L. Gu, X. Chen, G. Liu, L. Wang and H. M. Cheng, An unusual strong visible–light absorption band in red anatase TiO2 photocatalyst induced by atomic hydrogen–occupied oxygen vacancies, *Adv. Mater.*, 2018, **30**, 1704479.

121 A. Uedono, S. Ishibashi, S. Keller, C. Moe, P. Cantu, T. Katona, D. Kamber, Y. Wu, E. Letts and S. Newman, Vacancy-oxygen complexes and their optical properties in AlN epitaxial films studied by positron annihilation, *J. Appl. Phys.*, 2009, **105**, 054501.

122 S. Gao, B. Gu, X. Jiao, Y. Sun, X. Zu, F. Yang, W. Zhu, C. Wang, Z. Feng and B. Ye, Highly efficient and exceptionally durable CO2 photoreduction to methanol over freestanding defective single-unit-cell bismuth vanadate layers, *J. Am. Chem. Soc.*, 2017, **139**, 3438–3445.

123 T. Zhai, S. Xie, M. Yu, P. Fang, C. Liang, X. Lu and Y. Tong, Oxygen vacancies enhancing capacitive properties of MnO_2 nanorods for wearable asymmetric supercapacitors, *Nano Energy*, 2014, **8**, 255–263.

124 D. Sun, Y. Li, X. Cheng, H. Shi, S. Jaffer, K. Wang, X. Liu, J. Lu and Y. Zhang, Efficient utilization of oxygen-vacancies-enabled NiCo2O4 electrode for high-performance asymmetric supercapacitor, *Electrochim. Acta*, 2018, **279**, 269–278.

125 Y. C. Wang and J. M. Wu, Effect of controlled oxygen vacancy on H2−production through the piezocatalysis and piezophototronics of ferroelectric R3C ZnSnO3 nanowires, *Adv. Funct. Mater.*, 2020, **30**, 1907619.

126 C. Zhang, G. Liu, X. Geng, K. Wu and M. Debliquy, Metal oxide semiconductors with highly concentrated oxygen vacancies for gas sensing materials: A review, *Sens. Actuators, A*, 2020, **309**, 112026.

127 Y. Li, M. Wen, Y. Wang, G. Tian, C. Wang and J. Zhao, Plasmonic Hot Electrons from Oxygen Vacancies for Infrared Light–Driven Catalytic CO2 Reduction on Bi2O3−x, *Angew. Chem.*, 2021, **133**, 923–929.

128 G. Ou, Y. Xu, B. Wen, R. Lin, B. Ge, Y. Tang, Y. Liang, C. Yang, K. Huang and D. Zu, Tuning defects in oxides at room temperature by lithium reduction, *Nat. Commun.*, 2018, **9**, 1302.

129 Y. Liu, C. Ma, Q. Zhang, W. Wang, P. Pan, L. Gu, D. Xu, J. Bao and Z. Dai, 2D electron gas and oxygen vacancy induced high oxygen evolution performances for advanced Co3O4/CeO_2 nanohybrids, *Adv. Mater.*, 2019, **31**, 1900062.

130 J. Qian, S. Zhao, W. Dang, Y. Liao, W. Zhang, H. Wang, L. Lv, L. Luo, H. Y. Jiang and J. Tang, Photocatalytic nitrogen reduction by Ti3C2 MXene derived oxygen vacancy–rich C/TiO2, *Adv. Sustainable Syst.*, 2021, **5**, 2000282.

131 J. Wan, W. Chen, C. Jia, L. Zheng, J. Dong, X. Zheng, Y. Wang, W. Yan, C. Chen and Q. Peng, Defect effects on TiO2 nanosheets: stabilizing single atomic site Au and promoting catalytic properties, *Adv. Mater.*, 2018, **30**, 1705369.

132 S. Liu, Y. Yin, D. Ni, K. Hui, M. Ma, S. Park, K. N. Hui, C.-Y. Ouyang and S. C. Jun, New insight into the effect of fluorine doping and oxygen vacancies on electrochemical performance of Co2MnO4 for flexible quasi-solid-state asymmetric supercapacitors, *Energy Storage Mater.*, 2019, **22**, 384–396.

133 S. Wang, T. He, P. Chen, A. Du, K. Ostrikov, W. Huang and L. Wang, In situ formation of oxygen vacancies achieving near–complete charge separation in planar BiVO4 photoanodes, *Adv. Mater.*, 2020, **32**, 2001385.

134 Z. Wang, X. Mao, P. Chen, M. Xiao, S. A. Monny, S. Wang, M. Konarova, A. Du and L. Wang, Understanding the roles of oxygen vacancies in hematite–based photoelectrochemical processes, *Angew. Chem.*, 2019, **131**, 1042–1046.

135 K. Zhu, F. Shi, X. Zhu and W. Yang, The roles of oxygen vacancies in electrocatalytic oxygen evolution reaction, *Nano Energy*, 2020, **73**, 104761.

136 A. Lepcha, C. Maccato, A. Mettenbörger, T. Andreu, L. Mayrhofer, M. Walter, S. Olthof, T.-P. Ruoko, A. Klein and M. Moseler, Electrospun black titania nanofibers: Influence of hydrogen plasma-induced disorder on the electronic structure and photoelectrochemical performance, *J. Phys. Chem. C*, 2015, **119**, 18835–18842.

137 X. Shan, Z. Wang, Y. Lin, T. Zeng, X. Zhao, H. Xu and Y. Liu, Silent Synapse Activation by Plasma–Induced Oxygen Vacancies in TiO2 Nanowire–Based Memristor, *Adv. Electron. Mater.*, 2020, **6**, 2000536.

138 Z. Wang, S. Tian, J. Guo and Z. Wang, Introducing Oxygen Vacancies and Ti3+ on Rh/TiO2 via Plasma Treatment for CO Hydrogenation to Ethanol, *Energy Fuels*, 2022, **37**(1), 214–221.

139 Z. Wang, C. Yang, T. Lin, H. Yin, P. Chen, D. Wan, F. Xu, F. Huang, J. Lin and X. Xie, H–doped black titania with very high solar absorption and excellent photocatalysis enhanced by localized surface plasmon resonance, *Adv. Funct. Mater.*, 2013, **23**, 5444–5450.

140 M. Ahmad, S. Liu, N. Mahmood, A. Mahmood, M. Ali, M. Zheng and J. Ni, Synergic Adsorption–Biodegradation by an Advanced Carrier for Enhanced Removal of High-Strength Nitrogen and Refractory Organics, *ACS Appl. Mater. Interfaces*, 2017, **9**, 13188–13200.

141 J. Lei, W. Liu, Y. Jin and B. Li, Oxygen vacancy-dependent chemiluminescence: A facile approach for quantifying oxygen defects in ZnO, *Anal. Chem.*, 2022, **94**, 8642–8650.

142 F. Chen, Z. Ma, L. Ye, T. Ma, T. Zhang, Y. Zhang and H. Huang, Macroscopic spontaneous polarization and surface oxygen vacancies collaboratively boosting CO2 photoreduction on BiOIO3 single crystals, *Adv. Mater.*, 2020, **32**, 1908350.

143 Q. Wu, J. Liang, J.-D. Yi, P.-C. Shi, Y.-B. Huang and R. Cao, Porous nitrogen/halogen dual-doped nanocarbons derived from imidazolium functionalized cationic metal-organic frameworks for highly efficient oxygen reduction reaction, *Sci. China Mater.*, 2019, **62**, 671–680.

144 Y. Sun, T. Xiong, F. Dong, H. Huang and W. Cen, Interlayer-I-doped BiOIO 3 nanoplates with an optimized electronic structure for efficient visible light photocatalysis, *Chem. Commun.*, 2016, **52**, 8243–8246.

145 M. Li, S. Yu, H. Huang, X. Li, Y. Feng, C. Wang, Y. Wang, T. Ma, L. Guo and Y. Zhang, Unprecedented eighteen–faceted BiOCl with a ternary facet junction boosting cascade charge flow and photo–redox, *Angew. Chem., Int. Ed.*, 2019, **58**, 9517–9521.

146 R. Li, F. Zhang, D. Wang, J. Yang, M. Li, J. Zhu, X. Zhou, H. Han and C. Li, Spatial separation of photogenerated electrons and holes among {010} and {110} crystal facets of BiVO4, *Nat. Commun.*, 2013, **4**, 1432.

147 A. Sinhamahapatra, J.-P. Jeon, J. Kang, B. Han and J.-S. Yu, Oxygen-deficient zirconia (ZrO2− x): a new material for solar light absorption, *Sci. Rep.*, 2016, **6**, 1–8.

148 A. Puigdollers, P. Schlexer, S. Tosoni and G. Pacchioni, Increasing oxide reducibility: the role of metal/oxide interfaces in the formation of oxygen vacancies, *ACS Catal.*, 2017, **7**, 6493–6513.

149 X. Chen, L. Liu, P. Y. Yu and S. S. Mao, Increasing solar absorption for photocatalysis with black hydrogenated titanium dioxide nanocrystals, *Science*, 2011, **331**, 746–750.

150 Y. Chen, Y. Zhang, Q. Kou, Y. Liu, D. Han, D. Wang, Y. Sun, Y. Zhang, Y. Wang, Z. Lu, L. Chen, J. Yang and S. G. Xing, Enhanced Catalytic Reduction of 4-Nitrophenol Driven by Fe3O4-Au Magnetic Nanocomposite Interface Engineering: From Facile Preparation to Recyclable Application, *Nanomaterials*, 2018, **8**, 353.

151 Y. Hu, Y. Pan, Z. Wang, T. Lin, Y. Gao, B. Luo, H. Hu, F. Fan, G. Liu and L. Wang, Lattice distortion induced internal electric field in TiO2 photoelectrode for efficient charge separation and transfer, *Nat. Commun.*, 2020, **11**, 2129.

152 S. Zhang, Z. Zhang and W. Leng, Understanding the enhanced photoelectrochemical water oxidation over Ti-doped α-Fe 2 O 3 electrodes by electrochemical reduction pretreatment, *Phys. Chem. Chem. Phys.*, 2020, **22**, 7835–7843.

153 S. Wang, P. Chen, J. H. Yun, Y. Hu and L. Wang, An electrochemically treated BiVO4 photoanode for efficient photoelectrochemical water splitting, *Angew. Chem.*, 2017, **129**, 8620–8624.

154 W. Guo, C. Yu, S. Li, X. Song, H. Huang, X. Han, Z. Wang, Z. Liu, J. Yu and X. Tan, A universal converse voltage process for triggering transition metal hybrids in situ phase restruction toward ultrahigh–rate supercapacitors, *Adv. Mater.*, 2019, **31**, 1901241.

155 G. Wang, Y. Yang, Y. Ling, H. Wang, X. Lu, Y.-C. Pu, J. Z. Zhang, Y. Tong and Y. Li, An electrochemical method to enhance the performance of metal oxides for photoelectrochemical water oxidation, *J. Mater. Chem. A*, 2016, **4**, 2849–2855.

156 Q. Ye, R. Dong, Z. Xia, G. Chen, H. Wang, G. Tan, L. Jiang and F. Wang, Enhancement effect of Na ions on capacitive behavior of amorphous MnO_2, *Electrochim. Acta*, 2014, **141**, 286–293.

157 A. K. Tomar, R. B. Marichi, G. Singh and R. K. Sharma, Enhanced electrochemical performance of anion-intercalated lanthanum molybdenum oxide pseudocapacitor electrode, *Electrochim. Acta*, 2019, **296**, 120–129.

158 T. Meng, Z. Kou, I. S. Amiinu, X. Hong, Q. Li, Y. Tang, Y. Zhao, S. Liu, L. Mai and S. Mu, Electronic Structure Control of Tungsten Oxide Activated by Ni for Ultrahigh–Performance Supercapacitors, *Small*, 2018, **14**, 1800381.

159 J. Kang, A. Hirata, L. Kang, X. Zhang, Y. Hou, L. Chen, C. Li, T. Fujita, K. Akagi and M. Chen, Enhanced supercapacitor performance of MnO_2 by atomic doping, *Angew. Chem., Int. Ed.*, 2013, **52**, 1664–1667.

160 A. K. Tomar, G. Singh and R. K. Sharma, Fabrication of a Mo–doped strontium cobaltite perovskite hybrid supercapacitor cell with high energy density and excellent cycling life, *ChemSusChem*, 2018, **11**, 4123–4130.

161 Y. Jiang, C. Choi, S. Hong, S. Chu, T.-S. Wu, Y.-L. Soo, L. Hao, Y. Jung and Z. Sun, Enhanced electrochemical CO2 reduction to ethylene over CuO by synergistically tuning oxygen vacancies and metal doping, *Cell Rep. Phys. Sci.*, 2021, **2**, 100356.

162 K. Zhang, G. Zhang, J. Qu and H. Liu, Disordering the atomic structure of Co(II) oxide via b–doping: an efficient

oxygen vacancy introduction approach for high oxygen evolution reaction electrocatalysts, *Small*, 2018, **14**, 1802760.

163 Y. Wang, H. Li, W. Zhou, X. Zhang, B. Zhang and Y. Yu, Structurally disordered RuO2 nanosheets with rich oxygen vacancies for enhanced nitrate electroreduction to ammonia, *Angew. Chem.*, 2022, **134**, e202202604.

164 S. Kunze, L. C. Tănase, M. J. Prieto, P. Grosse, F. Scholten, L. de Souza Caldas, D. van Vörden, T. Schmidt and B. R. Cuenya, Plasma-assisted oxidation of Cu(100) and Cu(111), *Chem. Sci.*, 2021, **12**, 14241–14253.

165 Z. Wang, S. Liu, X. Zhao, M. Wang, L. Zhang, T. Qian, J. Xiong, C. Yang and C. Yan, Interfacial Defect Engineering Triggered by Single Atom Doping for Highly Efficient Electrocatalytic Nitrate Reduction to Ammonia, *ACS Mater. Lett.*, 2023, **5**, 1018–1026.

166 X. Wang, D. Zhang, Q. Xiang, Z. Zhong and Y. Liao, Review of Water-Assisted Crystallization for TiO2 Nanotubes, *Nano-Micro Lett.*, 2018, **10**, 77.

167 S. Chen, H. Wang, Z. Kang, S. Jin, X. Zhang, X. Zheng, Z. Qi, J. Zhu, B. Pan and Y. Xie, Oxygen vacancy associated single-electron transfer for photofixation of CO2 to long-chain chemicals, *Nat. Commun.*, 2019, **10**, 788.

168 Y. Bo, H. Wang, Y. Lin, T. Yang, R. Ye, Y. Li, C. Hu, P. Du, Y. Hu and Z. Liu, Altering hydrogenation pathways in photocatalytic nitrogen fixation by tuning local electronic structure of oxygen vacancy with dopant, *Angew. Chem., Int. Ed.*, 2021, **60**, 16085–16092.

169 Z. Gong, W. Zhong, Z. He, Q. Liu, H. Chen, D. Zhou, N. Zhang, X. Kang and Y. Chen, Regulating surface oxygen species on copper(I) oxides via plasma treatment for effective reduction of nitrate to ammonia, *Appl. Catal., B*, 2022, **305**, 121021.

170 Z. Wu, Y. Zhao, W. Jin, B. Jia, J. Wang and T. Ma, Recent progress of vacancy engineering for electrochemical energy conversion related applications, *Adv. Funct. Mater.*, 2021, **31**, 2009070.

171 H. B. Tao, L. Fang, J. Chen, H. B. Yang, J. Gao, J. Miao, S. Chen and B. Liu, Identification of surface reactivity descriptor for transition metal oxides in oxygen evolution reaction, *J. Am. Chem. Soc.*, 2016, **138**, 9978–9985.

172 Q. Song, S. Zhang, X. Hou, J. Li, L. Yang, X. Liu and M. Li, Efficient electrocatalytic nitrate reduction via boosting oxygen vacancies of TiO2 nanotube array by highly dispersed trace Cu doping, *J. Hazard. Mater.*, 2022, **438**, 129455.

173 N. Zhang, G. Zhang, P. Shen, H. Zhang, D. Ma and K. Chu, Lewis Acid Fe–V Pairs Promote Nitrate Electroreduction to Ammonia, *Adv. Funct. Mater.*, 2023, **33**, 2211537.

174 G. Zhang, X. Li, K. Chen, Y. Guo, D. Ma and K. Chu, Tandem electrocatalytic nitrate reduction to ammonia on MBenes, *Angew. Chem., Int. Ed.*, 2023, **62**, e202300054.

175 H. M. A. Sharif, M. Ali, A. Mahmood, M. B. Asif, M. A. U. Din, M. Sillanpää, A. Mahmood and B. Yang, Separation of Fe from wastewater and its use for NOx reduction; a sustainable approach for environmental remediation, *Chemosphere*, 2022, **303**, 135103.

176 C. T. Campbell and C. H. Peden, Oxygen vacancies and catalysis on ceria surfaces, *Science*, 2005, **309**, 713–714.

177 Z. Li, Z. Deng, L. Ouyang, X. Fan, L. Zhang, S. Sun, Q. Liu, A. A. Alshehri, Y. Luo and Q. Kong, CeO_2 nanoparticles with oxygen vacancies decorated N-doped carbon nanorods: A highly efficient catalyst for nitrate electroreduction to ammonia, *Nano Res.*, 2022, **15**, 8914–8921.

178 Z. X. Ge, T. J. Wang, Y. Ding, S. B. Yin, F. M. Li, P. Chen and Y. Chen, Interfacial engineering enhances the electroactivity of frame–like concave RhCu bimetallic nanocubes for nitrate reduction, *Adv. Energy Mater.*, 2022, **12**, 2103916.

179 T. J. Wang, Y. C. Jiang, J. W. He, F. M. Li, Y. Ding, P. Chen and Y. Chen, Porous palladium phosphide nanotubes for formic acid electrooxidation, *Carbon Energy*, 2022, **4**, 283–293.

180 Y. Xu, M. Wang, K. Ren, T. Ren, M. Liu, Z. Wang, X. Li, L. Wang and H. Wang, Atomic defects in pothole-rich two-dimensional copper nanoplates triggering enhanced electrocatalytic selective nitrate-to-ammonia transformation, *J. Mater. Chem. A*, 2021, **9**, 16411–16417.

181 X. Li, G. Hai, J. Liu, F. Zhao, Z. Peng, H. Liu, M. K. Leung and H. Wang, Bio-inspired NiCoP/CoMoP/Co (Mo3Se4) 4@ C/NF multi-heterojunction nanoflowers: Effective catalytic nitrogen reduction by driving electron transfer, *Appl. Catal., B*, 2022, **314**, 121531.

182 Z. Fang, Z. Jin, S. Tang, P. Li, P. Wu and G. Yu, Porous two-dimensional iron-cyano nanosheets for high-rate electrochemical nitrate reduction, *ACS Nano*, 2021, **16**, 1072–1081.

183 F. Zhao, G. Hai, X. Li, Z. Jiang and H. Wang, Enhanced electrocatalytic nitrate reduction to ammonia on cobalt oxide nanosheets via multiscale defect modulation, *Chem. Eng. J.*, 2023, **461**, 141960.

184 S. Cheng, Y.-J. Gao, Y.-L. Yan, X. Gao, S.-H. Zhang, G.-L. Zhuang, S.-W. Deng, Z.-Z. Wei, X. Zhong and J.-G. Wang, Oxygen vacancy enhancing mechanism of nitrogen reduction reaction property in Ru/TiO2, *J. Energy Chem.*, 2019, **39**, 144–151.

185 R. Huang, Y. Zhu, M. T. Curnan, Y. Zhang, J. W. Han, Y. Chen, S. Huang and Z. Lin, Tuning reaction pathways of peroxymonosulfate-based advanced oxidation process via defect engineering, *Cell Rep. Phys. Sci.*, 2021, **2**, 100550.

186 S. Tang, Q. Dang, T. Liu, S. Zhang, Z. Zhou, X. Li, X. Wang, E. Sharman, Y. Luo and J. Jiang, Realizing a not-strong-not-weak polarization electric field in single-atom catalysts sandwiched by boron nitride and graphene sheets for efficient nitrogen fixation, *J. Am. Chem. Soc.*, 2020, **142**, 19308–19315.

187 X. Li, Y. Luo, Q. Li, Y. Guo and K. Chu, Constructing an electron-rich interface over an Sb/Nb 2 CT x–MXene heterojunction for enhanced electrocatalytic nitrogen reduction, *J. Mater. Chem. A*, 2021, **9**, 15955–15962.

188 S. Dong, A. Niu, K. Wang, P. Hu, H. Guo, S. Sun, Y. Luo, Q. Liu, X. Sun and T. Li, Modulation of oxygen vacancy and zero-valent zinc in ZnCr2O4 nanofibers by enriching zinc for efficient nitrate reduction, *Appl. Catal., B*, 2023, 122772.

189 V. L. Deringer, A. L. Tchougréeff and R. Dronskowski, Crystal orbital Hamilton population (COHP) analysis as projected from plane-wave basis sets, *J. Phys. Chem. A*, 2011, **115**, 5461–5466.

190 B. Sambandam, V. Mathew, S. Kim, S. Lee, S. Kim, J. Y. Hwang, H. J. Fan and J. Kim, An analysis of the electrochemical mechanism of manganese oxides in aqueous zinc batteries, *Chem*, 2022, **8**, 924–946.

191 W. Gao, J. V. Perales-Rondon, J. Michalička and M. Pumera, Ultrathin manganese oxides enhance the electrocatalytic properties of 3D printed carbon catalysts for electrochemical nitrate reduction to ammonia, *Appl. Catal., B*, 2023, **330**, 122632.

192 W. Wen, P. Yan, W. Sun, Y. Zhou and X. Y. Yu, Metastable phase Cu with optimized local electronic state for efficient electrocatalytic production of ammonia from nitrate, *Adv. Funct. Mater.*, 2023, **33**, 2212236.

193 Y. Wang, W. Zhou, R. Jia, Y. Yu and B. Zhang, Unveiling the activity origin of a copper–based electrocatalyst for selective nitrate reduction to ammonia, *Angew. Chem., Int. Ed.*, 2020, **59**, 5350–5354.

194 D. Jang, J. Maeng, J. Kim, H. Han, G. H. Park, J. Ha, D. Shin, Y. J. Hwang and W. B. Kim, Boosting electrocatalytic nitrate reduction reaction for ammonia synthesis by plasma-induced oxygen vacancies over MnCuOx, *Appl. Surf. Sci.*, 2023, **610**, 155521.

195 Y. Wang, S. Shu, M. Peng, L. Hu, X. Lv, Y. Shen, H. Gong and G. Jiang, Dual-site electrocatalytic nitrate reduction to ammonia on oxygen vacancy-enriched and Pd-decorated MnO 2 nanosheets, *Nanoscale*, 2021, **13**, 17504–17511.

196 K. Chen, Z. Ma, X. Li, J. Kang, D. Ma and K. Chu, Single–Atom Bi Alloyed Pd Metallene for Nitrate Electroreduction to Ammonia, *Adv. Funct. Mater.*, 2023, **33**, 2209890.

197 H. Wang, Q. Mao, T. Ren, T. Zhou, K. Deng, Z. Wang, X. Li, Y. Xu and L. Wang, Synergism of interfaces and defects: Cu/oxygen vacancy-rich Cu-Mn3O4 heterostructured ultrathin nanosheet arrays for selective nitrate electroreduction to ammonia, *ACS Appl. Mater. Interfaces*, 2021, **13**, 44733–44741.

198 Z. Meng, J. X. Yao, C. N. Sun, X. Kang, R. Gao, H. R. Li, B. Bi, Y. F. Zhu, J. M. Yan and Q. Jiang, Efficient Ammonia Production Beginning from Enhanced Air Activation, *Adv. Energy Mater.*, 2022, **12**, 2202105.

199 B. Li, P. Xue, Y. Bai, Q. Tang, M. Qiao and D. Zhu, Coupling Cu doping and oxygen vacancies in Co3O4 for efficient electrochemical nitrate conversion to ammonia, *Chem. Commun.*, 2023, **59**, 5086–5089.

200 M. Khan, A. Hameed, A. Samad, T. Mushiana, M. I. Abdullah, A. Akhtar, R. S. Ashraf, N. Zhang, B. G. Pollet and U. Schwingenschlögl, In situ grown oxygen-vacancy-rich copper oxide nanosheets on a copper foam electrode afford the selective oxidation of alcohols to value-added chemicals, *Commun. Chem.*, 2022, **5**, 109.

201 T. X. Nguyen, Y. C. Liao, C. C. Lin, Y. H. Su and J. M. Ting, Advanced high entropy perovskite oxide electrocatalyst for oxygen evolution reaction, *Adv. Funct. Mater.*, 2021, **31**, 2101632.

202 Y. Wang, R. Yang, Y. Ding, B. Zhang, H. Li, B. Bai, M. Li, Y. Cui, J. Xiao and Z.-S. Wu, Unraveling oxygen vacancy site mechanism of Rh-doped RuO2 catalyst for long-lasting acidic water oxidation, *Nat. Commun.*, 2023, **14**, 1412.

203 R. Hu, M. Zhao, H. Miao, F. Liu, J. Zou, C. Zhang, Q. Wang, Z. Tian, Q. Zhang and J. Yuan, Rapidly reconstructing the active surface of cobalt-based perovskites for alkaline seawater splitting, *Nanoscale*, 2022, **14**, 10118–10124.

204 X. Li, X. Wang, J. Ding, M. Ma, S. Yuan, Q. Yang, Z. Wang, Y. Peng, C. Sun and H. Zhou, Engineering Active Surface Oxygen Sites of Cubic Perovskite Cobalt Oxides toward Catalytic Oxidation Reactions, *ACS Catal.*, 2023, **13**, 6338–6350.

205 F. Liu, Z. Zhang, L. Shi, Y. Zhang, X. Qiu, Y. Dong, H. Jiang, Y. Zhu and J. Zhu, Promoting nitrate electroreduction to ammonia over A-site deficient cobalt-based perovskite oxides, *J. Mater. Chem. A*, 2023, **11**, 1056–10604.

206 D. A. Kuznetsov, M. A. Naeem, P. V. Kumar, P. M. Abdala, A. Fedorov and C. R. Müller, Tailoring lattice oxygen binding in ruthenium pyrochlores to enhance oxygen evolution activity, *J. Am. Chem. Soc.*, 2020, **142**, 7883–7888.

207 C. Cao, D. D. Ma, J. F. Gu, X. Xie, G. Zeng, X. Li, S. G. Han, Q. L. Zhu, X. T. Wu and Q. Xu, Metal–organic layers leading to atomically thin bismuthene for efficient carbon dioxide electroreduction to liquid fuel, *Angew. Chem., Int. Ed.*, 2020, **59**, 15014–15020.

208 K. Deng, T. Zhou, Q. Mao, S. Wang, Z. Wang, Y. Xu, X. Li, H. Wang and L. Wang, Surface engineering of defective and porous Ir metallene with polyallylamine for hydrogen evolution electrocatalysis, *Adv. Mater.*, 2022, **34**, 2110680.

209 H. Yu, T. Zhou, Z. Wang, Y. Xu, X. Li, L. Wang and H. Wang, Defect–rich porous palladium metallene for enhanced alkaline oxygen reduction electrocatalysis, *Angew. Chem.*, 2021, **133**, 12134–12138.

210 X. Lu, M. Cai, X. Wu, Y. Zhang, S. Li, S. Liao and X. Lu, Controllable Synthesis of 2D Materials by Electrochemical Exfoliation for Energy Storage and Conversion Application, *Small*, 2023, **19**, 2206702.

211 Y. Cui, A. Dong, Y. Zhou, Y. Qu, M. Zhao, Z. Wang and Q. Jiang, Interfacially Engineered Nanoporous Cu/MnOx Hybrids for Highly Efficient Electrochemical Ammonia Synthesis via Nitrate Reduction, *Small*, 2023, 2207661.

212 H. Wang, Y. Guo, C. Li, H. Yu, K. Deng, Z. Wang, X. Li, Y. Xu and L. Wang, Cu/CuO x In-Plane Heterostructured Nanosheet Arrays with Rich Oxygen Vacancies Enhance Nitrate Electroreduction to Ammonia, *ACS Appl. Mater. Interfaces*, 2022, **14**, 34761–34769.

213 Z. Sun, R. Huo, C. Choi, S. Hong, T.-S. Wu, J. Qiu, C. Yan, Z. Han, Y. Liu and Y.-L. Soo, Oxygen vacancy enables electrochemical N2 fixation over WO3 with tailored structure, *Nano Energy*, 2019, **62**, 869–875.

214 T. Feng, F. Li, X. Hu and Y. Wang, Selective electroreduction of nitrate to ammonia via NbWO6 perovskite nanosheets with oxygen vacancy, *Chin. Chem. Lett.*, 2023, **34**, 107862.

215 L. Huang, J. Wu, P. Han, A. M. Al-Enizi, T. M. Almutairi, L. Zhang and G. Zheng, NbO2 electrocatalyst toward 32% faradaic efficiency for N2 fixation, *Small Methods*, 2019, **3**, 1800386.

216 W. Kong, Z. Liu, J. Han, L. Xia, Y. Wang, Q. Liu, X. Shi, Y. Wu, Y. Xu and X. Sun, Ambient electrochemical N 2-to-NH 3 fixation enabled by Nb 2 O 5 nanowire array, *Inorg. Chem. Front.*, 2019, **6**, 423–427.

217 X. Wan, W. Guo, X. Dong, H. Wu, X. Sun, M. Chu, S. Han, J. Zhai, W. Xia and S. Jia, Boosting nitrate electroreduction to ammonia on NbO x via constructing oxygen vacancies, *Green Chem.*, 2022, **24**, 1090–1095.

218 J. Lim, C.-Y. Liu, J. Park, Y.-H. Liu, T. P. Senftle, S. W. Lee and M. C. Hatzell, Structure sensitivity of Pd facets for enhanced electrochemical nitrate reduction to ammonia, *ACS Catal.*, 2021, **11**, 7568–7577.

219 Y. Fu, S. Wang, Y. Wang, P. Wei, J. Shao, T. Liu, G. Wang and X. Bao, Enhancing Electrochemical Nitrate Reduction to Ammonia over Cu Nanosheets via Facet Tandem Catalysis, *Angew. Chem., Int. Ed.*, 2023, e202303327.

220 W. Zhong, Z. Gong, Z. He, N. Zhang, X. Kang, X. Mao and Y. Chen, Modulating surface oxygen species via facet engineering for efficient conversion of nitrate to ammonia, *J. Energy Chem.*, 2023, **78**, 211–221.

221 D. Chen, S. Zhang, X. Bu, R. Zhang, Q. Quan, Z. Lai, W. Wang, Y. Meng, D. Yin and S. Yip, Synergistic modulation of local environment for electrochemical nitrate reduction via asymmetric vacancies and adjacent ion clusters, *Nano Energy*, 2022, **98**, 107338.

222 A. J. Bard, R. Parsons and J. Jordan, in *Standard Potentials in Aqueous Solution*, Routledge, 2017, pp. 507–538.

223 Y. Yu, C. Wang, Y. Yu, Y. Wang and B. Zhang, Promoting selective electroreduction of nitrates to ammonia over electron-deficient Co modulated by rectifying Schottky contacts, *Sci. China: Chem.*, 2020, **63**, 1469–1476.

224 T. F. Beltrame, M. C. Gomes, L. Marder, F. A. Marchesini, M. A. Ulla and A. M. Bernardes, Use of copper plate electrode and Pd catalyst to the nitrate reduction in an electrochemical dual-chamber cell, *J. Water Process Eng.*, 2020, **35**, 101189.

225 H. Liu, J. Park, Y. Chen, Y. Qiu, Y. Cheng, K. Srivastava, S. Gu, B. H. Shanks, L. T. Roling and W. Li, Electrocatalytic nitrate reduction on oxide-derived silver with tunable selectivity to nitrite and ammonia, *ACS Catal.*, 2021, **11**, 8431–8442.

226 M. De Groot and M. Koper, The influence of nitrate concentration and acidity on the electrocatalytic reduction of nitrate on platinum, *J. Electroanal. Chem.*, 2004, **562**, 81–94.

227 J. Yang, F. Calle-Vallejo, M. Duca and M. T. Koper, Electrocatalytic Reduction of Nitrate on a Pt Electrode Modified by p–Block Metal Adatoms in Acid Solution, *ChemCatChem*, 2013, **5**, 1773–1783.

228 G. Dima, A. De Vooys and M. Koper, Electrocatalytic reduction of nitrate at low concentration on coinage and transition-metal electrodes in acid solutions, *J. Electroanal. Chem.*, 2003, **554**, 15–23.

229 A. deVooys, G. Beltramo, B. vanRiet, J. A. R. van Veen and M. T. M. Koper, *Electrochim. Acta*, 2004, **49**, 1307–1314.

230 I. Katsounaros and G. Kyriacou, Influence of nitrate concentration on its electrochemical reduction on tin cathode: Identification of reaction intermediates, *Electrochim. Acta*, 2008, **53**, 5477–5484.

231 E. Pérez-Gallent, M. C. Figueiredo, I. Katsounaros and M. T. Koper, Electrocatalytic reduction of Nitrate on Copper single crystals in acidic and alkaline solutions, *Electrochim. Acta*, 2017, **227**, 77–84.

232 D. Reyter, D. Bélanger and L. Roué, Study of the electroreduction of nitrate on copper in alkaline solution, *Electrochim. Acta*, 2008, **53**, 5977–5984.

233 C. A. Casey-Stevens, H. Ásmundsson, E. Skúlason and A. L. Garden, A density functional theory study of the mechanism and onset potentials for the major products of NO electroreduction on transition metal catalysts, *Appl. Surf. Sci.*, 2021, **552**, 149063.

234 G.-F. Chen, Y. Yuan, H. Jiang, S.-Y. Ren, L.-X. Ding, L. Ma, T. Wu, J. Lu and H. Wang, Electrochemical reduction of nitrate to ammonia via direct eight-electron transfer using a copper–molecular solid catalyst, *Nat. Energy*, 2020, **5**, 605–613.

235 Y. Yao, S. Zhu, H. Wang, H. Li and M. Shao, A spectroscopic study of electrochemical nitrogen and nitrate reduction on rhodium surfaces, *Angew. Chem.*, 2020, **132**, 10565–10569.

236 M. Duca and M. T. Koper, Powering denitrification: the perspectives of electrocatalytic nitrate reduction, *Energy Environ. Sci.*, 2012, **5**, 9726–9742.

237 Z. Wang, D. Richards and N. Singh, Recent discoveries in the reaction mechanism of heterogeneous electrocatalytic nitrate reduction, *Catal. Sci. Technol.*, 2021, **11**, 705–725.

238 H. M. A. Sharif, M. B. Asif, Y. Wang, K. Khan, Y. Cai, X. Xiao and C. Li, Construction and elucidation of zerovalent iron@terephthalic acid/iron oxide catalyst to activate peroxymonosulfate for accelerating and long-lasting NOx removal, *Chem. Eng. J.*, 2023, **465**, 142782.

239 H.-J. Chun, Z. Zeng and J. Greeley, DFT insights into NO electrochemical reduction: a case study of Pt (211) and Cu (211) surfaces, *ACS Catal.*, 2022, **12**, 1394–1402.

240 H. Wan, A. Bagger and J. Rossmeisl, Electrochemical nitric oxide reduction on metal surfaces, *Angew. Chem.*, 2021, **133**, 22137–22143.

241 D. Anastasiadou, Y. van Beek, E. J. Hensen and M. Figueiredo, Ammonia electrocatalytic synthesis from nitrate, *Electrochem. Sci. Adv.*, 2022, e2100220.

242 H. M. A. Sharif, N. Mahmood, S. Wang, I. Hussain, Y.-N. Hou, L.-H. Yang, X. Zhao and B. Yang, Recent advances in hybrid wet scrubbing techniques for NOx and SO2 removal: State of the art and future research, *Chemosphere*, 2021, **273**, 129695.

243 H. Han, S. Jin, S. Park, Y. Kim, D. Jang, M. H. Seo and W. B. Kim, Plasma-induced oxygen vacancies in amorphous MnOx boost catalytic performance for electrochemical CO2 reduction, *Nano Energy*, 2021, **79**, 105492.

244 Y. Du, X. Wang and J. Sun, Tunable oxygen vacancy concentration in vanadium oxide as mass-produced cathode for aqueous zinc-ion batteries, *Nano Res.*, 2021, **14**, 754–761.

245 Z.-F. Huang, S. Xi, J. Song, S. Dou, X. Li, Y. Du, C. Diao, Z. J. Xu and X. Wang, Tuning of lattice oxygen reactivity and scaling relation to construct better oxygen evolution electrocatalyst, *Nat. Commun.*, 2021, **12**, 3992.

246 H. Yi, T. Choi, S. Choi, Y. S. Oh and S. W. Cheong, Mechanism of the switchable photovoltaic effect in ferroelectric BiFeO3, *Adv. Mater.*, 2011, **23**, 3403–3407.

247 P. Scheiber, M. Fidler, O. Dulub, M. Schmid, U. Diebold, W. Hou, U. Aschauer and A. Selloni, (Sub) Surface mobility of oxygen vacancies at the TiO 2 anatase (101) surface, *Phys. Rev. Lett.*, 2012, **109**, 136103.

248 S. Lee, W. Jin, S. H. Kim, S. H. Joo, G. Nam, P. Oh, Y. K. Kim, S. K. Kwak and J. Cho, Oxygen Vacancy Diffusion and Condensation in Lithium–Ion Battery Cathode Materials, *Angew. Chem., Int. Ed.*, 2019, **58**, 10478–10485.

249 G. Wang, Y. Ling, X. Lu, F. Qian, Y. Tong, J. Z. Zhang, V. Lordi, C. Leao and Y. Li, Computational and photoelectrochemical study of hydrogenated bismuth vanadate, *J. Phys. Chem. C*, 2013, **117**, 10957–10964.

250 B. Klahr, S. Gimenez, F. Fabregat-Santiago, T. Hamann and J. Bisquert, Water oxidation at hematite photoelectrodes: the role of surface states, *J. Am. Chem. Soc.*, 2012, **134**, 4294–4302.

251 Z. Li, W. Yang, L. Xie, Y. Li, Y. Liu, Y. Sun, Y. Bu, X. Mi, S. Zhan and W. Hu, Prominent role of oxygen vacancy for superoxide radical and hydroxyl radical formation to promote electro-Fenton like reaction by W-doped CeO_2 composites, *Appl. Surf. Sci.*, 2021, **549**, 149262.

252 H. Xu, Y. Ma, J. Chen, W.-X. Zhang and J. Yang, Electrocatalytic reduction of nitrate–a step towards a sustainable nitrogen cycle, *Chem. Soc. Rev.*, 2022, **51**, 2710–2758.